VALIDATION OF CFD FOR FLOW DISTRIBUTION IN CANDU HEADERS

VALIDATION OF COMPUTATIONAL FLUID DYNAMIC TOOLS FOR SINGLE-PHASE FLOW DISTRIBUTION IN CANDU HEADERS

By

ALA MUHANA. B. Sc.

A Thesis

Submitted to the School of Graduate Studies

in Partial Fulfillment of the Requirements for the Degree of

M. A. Sc. In Engineering Physics

McMaster University

MASTER OF APPLIED SCIENCES (2009) McMaster University
(Engineering Physics) Hamilton, Ontario

TITLE: Validation of Computational Fluid Dynamic Tools for Single-Phase Flow Distribution in CANDU Headers

AUTHER: Ala Muhana, B. Sc. (Jordan University of Science and Technology)

SUPERVISOR: Dr. David Novog

NUMBER OF PAGES: xii, 112

Abstract

Canada Deuterium Uranium, CANDU, nuclear reactors use forced convection cooling to remove heat from the nuclear fuel and transport it to the power production systems. Flow is supplied by large capacity heat transport pumps and is distributed to each separate fuel assembly through headers. The determination of thermalhydraulic parameters of the CANDU headers is important because hydraulic behavior in the headers governs the void fractions of fuel channels connected to them and influences the fuel bundles cooling efficiency during postulated accidents.

This work presents the validation of FLUENT 6.3.26, a three dimensional Computational Fluid Dynamics (CFD) code, for header flow distribution simulations by comparing predictions to experimental data. The experimental data were obtained for three different header geometries: horizontal header with four vertical outlets (case study-data obtained from literature), horizontal header with two vertical inlets and header with two horizontal inlets (experiments done in this study). The experiments were carried out using 1.0 m long, 3.67 cm ID horizontal cylindrical header with two symmetrical distributed vertical inlets or two horizontal inlets at the two header ends. The flow is distributed to five horizontal and five vertical outlets along the header with 0.92 cm ID.

In the first validation, FLUENT provided good predictions of flow distribution and pressure gradients along the header for different inlet flow rates (Re number between 800 and 4,800). In the second and third validations, simulations for both vertical and horizontal inlet configurations were examined and with varying levels of inlet flow imbalance. The experimental data consists of a set of outlet flow rates as a function of inlet flow rates. The effects of flow inlet velocities, flow modeling and grid density on the computational accuracy are also presented. The CFD technique was found to be an efficient tool to predict the flow distribution in the headers studied.

Acknowledgments

This report could not be appeared to the light without the efforts of some kind people, which whatever I say I can't thank them as they deserve. First of all, I would like to sincerely thank Dr. David Novog for supervising this work and for his continuous invaluable guidance and support.

I thank my parents for their support, my husband Kifah for his continuous encouragement, my daughter Ayshah and my son Yahya for their patience while doing this work.

And thanks for everyone helped in the succession of this report.

Nomenclature

C_1	Turbulence intensity constant
C_2	Turbulence dissipation constant
$C_{1\varepsilon}$	Empirical constant in ε transport equation
$C_{2\varepsilon}$	Empirical constant in ε transport equation
C_μ	Constant in turbulent viscosity formulation
F_i	External body force (N/m^3)
g_i	Gravitational acceleration (m/sec^2)
h	Outlet branch length (m)
k	Turbulence intensity
P	Pressure (Pa)
Q	Inlet flow rate (m^3/s)
q_i	Outlet flow rate in branch i (m^3/s)
R_{ij}	Reynolds shear stress at *ij* surface (N/m^2)
T	Large time scale (s)
t	Time (s)
U_i	Flow mean velocity (m/s)
$U_i(t)$	Flow velocity (m/s)
$u_i(t)$	Flow turbulent fluctuating velocity (m/s)
u_i	Fluid velocity components (m/s) where i denotes the coordinate
V	Header inlet velocity (m/s)
v_m	Fluid velocity in the header just before branch m (m/s)
x_i	Spatial coordinates (m)
Y	The physical wall distance (m)
Y^+	Non-dimensional wall distance
Δp_{ik}	Pressure difference between two planes i^{th} and k^{th} (Pa)
δ_{ij}	Delta function
ε	Turbulence dissipation
μ	Molecular viscosity (Pa. s)
μ_t	Turbulent viscosity (Pa. s)
ρ	Fluid density (kg/m^3)
σ_k	Turbulent Prandtl number for k
σ_ε	Turbulent Prandtl number for ε
τ_{ij}	Shear stress at *ij* surface (N/m^2)
τ_w	Shear stress at the wall (N/m^2)

Abbreviations

AECL	Atomic Energy of Canada Limited
BWR	Boiling Water Reactor
CANDU	Canada Deuterium / Uranium
CATHENA	Canadian Algorithm for THErmalhydraulic Network Analysis
CFD	Computational Fluid Dynamics
DAS	Data Acquisition System
DNS	Direct Numerical Solution
ENH	Enhanced
GUI	Graphical User Interface
ID	Inner Diameter
LDA	Laser Doppler Anemometry
NEQ	Non-Equilibrium
NSA	Nuclear Safety Analysis
NUCIRC	NUclear CIRCuits
PHTS	Primary Heat Transport System
PWR	Pressurized Water Reactor
RANS	Reynolds-Averaged Navier Stokes
REAL	Realizable
RIH	Reactor Inlet Header
RNG	Re-Normalization Grouping
RSM	Reynolds Stress Model
SG	Steam Generator
SIMPLE	Semi-Implicit Method for Pressure Linked Equations
SST	Shear Stress Transport
STD	Standard
TDMA	Tri-Diagonal Matrix Algorithm
TUF	Two Unequal Fluids

Table of Contents

Subject **Page**

List of Figures

List of Tables

Chapter 1

Introduction

With the increase of the energy consumption, effects on the environment and the depletion of the limited energy resources, new and clean sources are required. To meet these needs new nuclear reactor stations are being designed and built where the thermal energy of the fission process is used to generate electrical power. The safety of the nuclear reactor is of great importance and Nuclear Safety Analysis (NSA) is an essential element of the safety assessment. NSA is an analytical study to demonstrate how safety requirements are met for a broad range of operating conditions and various initiating events (like accidents). NSA demonstrates that the reactor is kept within the safe operating margins and also provides an understanding of how the reactor will behave under postulated accident scenarios.

The safety analysis in the past was performed using prescribed conservative assumptions to account for uncertainties in the models, correlations, codes, and initial and boundary conditions of nuclear reactors. These assumptions include weakening the effectiveness of safety system trips or maximizing the cooling system hypothetical break sizes in order to analyze the worst case scenarios to account for those uncertainties [1].

With the huge improvement in the computational capabilities, there has been a move towards the CFD techniques. CFD techniques provide detailed modeling of the geometries and are more flexible and less reliant on empirical correlations [2]. In CFD, the details of the geometry are important to the flow field, and can be represented accurately.

This thesis investigates the suitability of Computational Fluid Dynamics (CFD) tools in predicting the behaviour of the reactor coolant in complex geometries representative of nuclear plant components. The work compares code prediction to previous and new experiments in representative geometries which has not previously been performed. Specifically, CFD tools will be validated for single phase flow distribution in scaled multi-branch headers representing the Canada Deuterium Uranium, CANDU, headers. The effects of header geometry and inlet flow imbalance on the CFD predictions are investigated. This study presents a review of previous work which has been conducted in the field as well as an overview of the reactor components where CFD was found to be efficient for the flow analysis. Detailed description of the CFD model is provided as well as a detailed description of the experimental facilities used to obtain the experimental data. Finally, results, conclusions and recommendations are provided.

The following sections introduce the main nuclear reactor components including the Primary Heat Transport System (PHTS), the reactor headers and reactor core (Section 1.1), the flow distribution in manifolds (Section 1.2), the CFD code validation (Section 1.3) and finally the objectives of this study (Section 1.4).

1.1 CANDU Reactor Main Components

1.1.1 Primary Heat Transport System (PHTS)

This system consists of fuel channels, headers, pumps and steam generators. A unique feature of the CANDU reactor design is that the fuel is located in separate pressure tubes rather than in a single vessel used like in Pressurized Water Reactors (PWR). The PHTS circulates pressurized heavy water coolant through fuel channels to carry heat produced from fission process and transfers it to light water in the steam generators to derive the turbines. In doing so, it accomplishes the safety goal of cooling the fuel and keeping it wet to protect it from overheating.

A main circulating pump takes cooled heavy water from the steam generator (SG) and pumps it to a RIH, which distributes the coolant to the next pass of feeders which are connected to individual fuel channels. The hot coolant leaves the channels into outlet feeders which lead to the reactor outlet header from where it is directed to a second SG in another circulation loop. Each PHTS loop is arranged in a "Figure of 8", with the coolant making two passes in opposite directions through the core, and the pumps in each loop operating in series. The coolant flow in adjacent channels is in opposite directions. The pressure in the PHTS is controlled by a pressurizer connected to the outlet headers at one end of the reactor [3].

Figure (1) shows a simplified PHTS layout of a typical CANDU reactor where two reactor inlet headers (RIH) distribute the flow into one half of the fuel channels each.

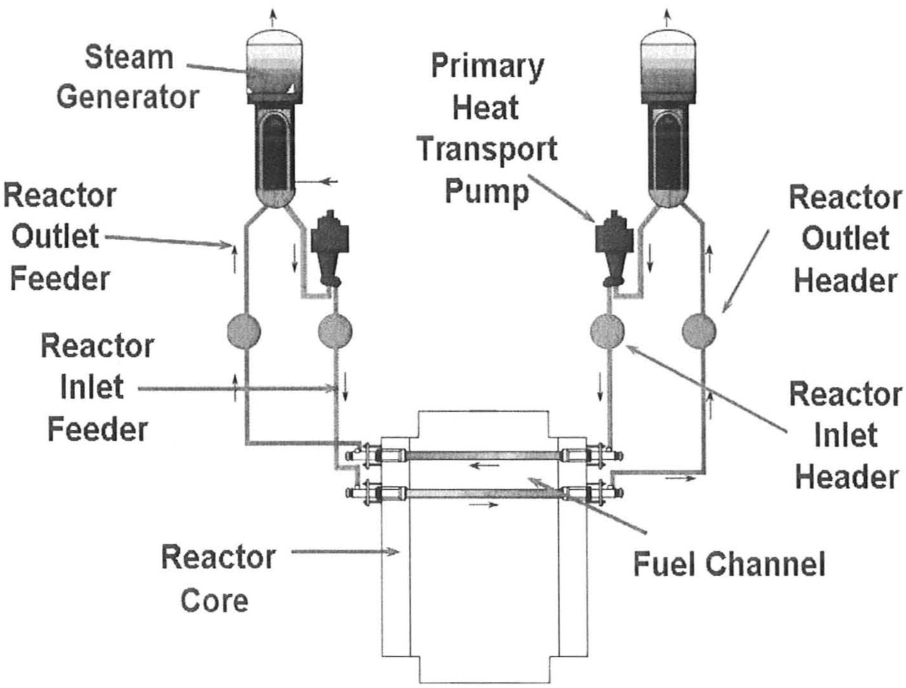

Figure (1): Simplified PHTS Circulating System [4].

1.1.1.1 CANDU Headers

The CANDU headers are long (approximately 6 m) with large diameters (approximately 0.35 m) vessels which connect the coolant pumps to the fuel channels (inlet headers) and the fuel channels to the steam generators (outlet headers). The headers are generally composed of two vertical turrets and the feeders are attached to the header's body in banks. In earlier CANDU reactors (i.e., Pickering), the flow to each inlet header is pumped by any 3 of 4 pumps equally distributed along the header's axis (where one pump is usually on standby at any given time, 16 pumps are in each reactor design). This connection of the flow channels in any reactor design coupled with the inlet pipe positions coming from the pumps may create temperature and pressure gradients along the length of the header which in turn may affect the flow characteristics in the fuel channels [4]. Figure (2) shows a typical RIH [5] like the ones used in Darlington CANDU reactor. In a different design (the Bruce Reactor) the two inlets of the RIH are horizontally aligned and connected to the header body at the far two edges as will be shown later (Figure (56)).

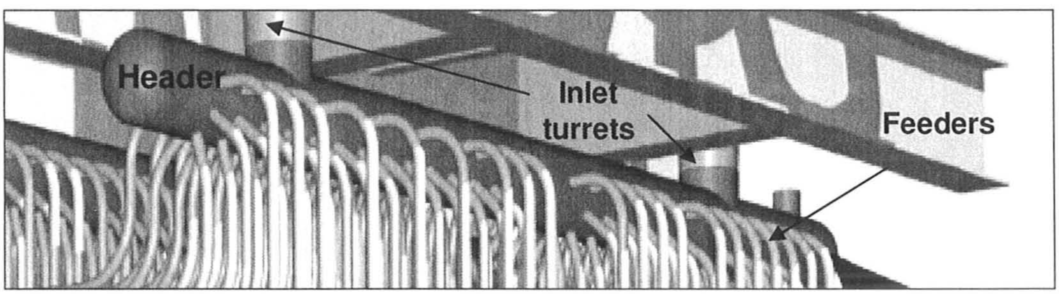

Figure (2): Typical Reactor Inlet Header RIH [5].

Thermalhydraulic analysis of the PHTS has historically been performed using one-dimensional averaged computer codes where phenomena are modeled using volume average approximations for each of the main components as it is impractical to simulate all of the three-dimensional fluid behavior in such large systems. Within this safety analysis, it is generally assumed that the pressure distribution along the inlet and outlet headers is uniform and the headers are constant pressure reservoirs [6, 7]. However, code predictions within some of the header components have shown that the steady-state pressure along the inlet header could vary by approximately 83 kPa [6]. The complex flow behavior in the headers has been modeled using one-dimensional models (discussed in Section 2.1) and empirically derived distribution coefficients, or by applying high safety factors to the analysis. Recently there has been a move toward the application of CFD to some components; however the CFD codes need to be validated before being accepted in the analysis (Section 1.4).

1.1.2 Reactor Core

The reactor core is composed of bundles, pressure tubes and a calandria vessel, which is 6 m long and 7.6 m in diameter (for the CANDU-6 reactor). It contains 380-480 horizontal fuel channels (dependant on the reactor design) which accounts for about 12% of the calandria vessel total volume. The remaining volume is largely composed of heavy water moderator. The main components of the CANDU reactor and the calandria vessel are shown in Figure (3). Each fuel channel consists of a pressure tube, which contains fuel bundles, and outer calandria tube. The fuel channel components are shown in Figure (4). Heavy water moderator flows around the channels. The calandria is considered a large volume component of the reactor where CFD has recently been investigated to predict flow and temperature distributions (Section 2.2.2).

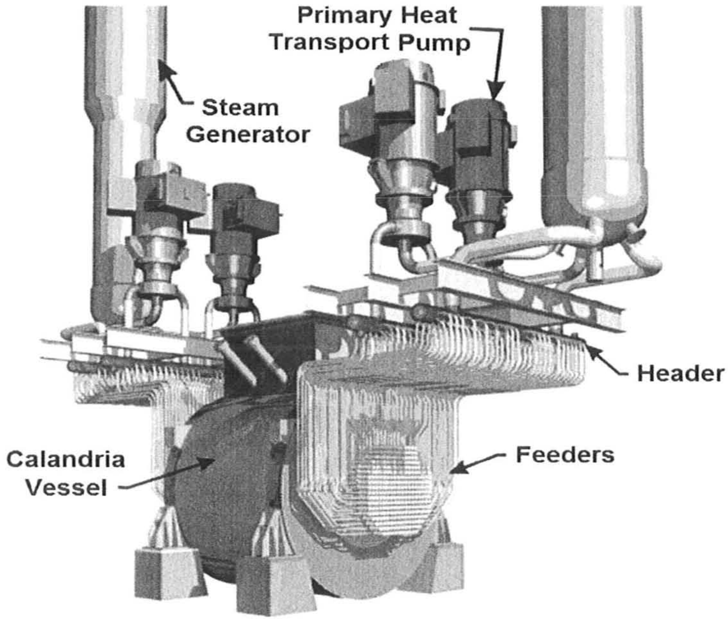

Figure (3): CANDU reactor main components [5].

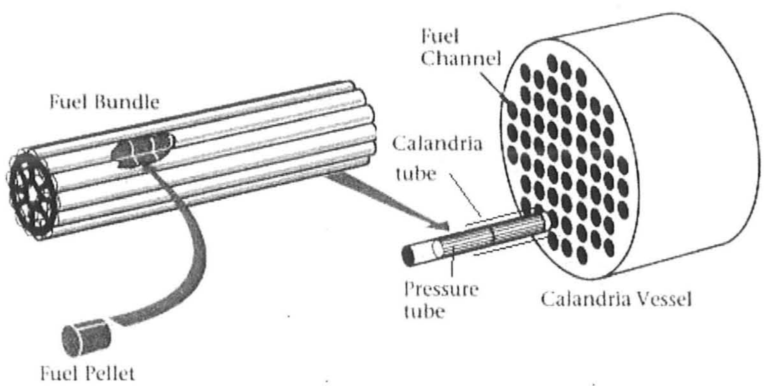

Figure (4): CANDU reactor fuel channel [8].

1.2 Flow Distributions in Manifolds

Equipment composed of headers and branch pipes for distributing a fluid stream or combining small streams are widely used in engineering applications. The manifold is defined as a volume with axial flow having many openings in the wall where the fluid leaves or enters under a pressure difference driving force. Two common manifold types used in flow distribution systems are the dividing and the combining manifolds [9]. The two types are illustrated in Figure (5).

Figure (5): Dividing (left) and combining (right) manifolds.

The division or combining of fluid by means of a manifold is accompanied by pressure gradients and changes in fluid momentum between the main stream and the branches. As the flow passes through a branch, two recirculation zones are formatted: one in the manifold and one downstream in the branch. This leads to a complex, swirling, three-dimensional flow field [10]. This is illustrated in Figure (6) where the magnitude and shape of the vortices depend on Re number.

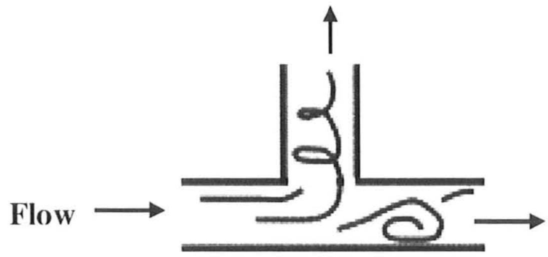

Figure (6): Vortex and swirling flow in a dividing manifold [11].

1.3 CFD Code Validation

Code Validation is defined as the process of checking that a code meets specifications and fulfils its intended purpose of giving the desired results with a defined accuracy.

In the past 20 years, significant developments in CFD capabilities have allowed these methods to be applied to a wide range of engineering problems. However, there is still limited confidence in CFD techniques unless they are validated against experimental data before being adopted in problems with similar range of conditions [12]. The flow pattern in headers and manifolds is highly complex. In the CANDU inlet header, for example, the flow encounters a sequence of branch points and its axial momentum along the header decreases as the flow is depleted. In practice, the flow in the headers is highly turbulent and complex 3-dimensional flows occur inside the header [9]. Furthermore during a hypothetical accident transient the Reynolds number can decrease significantly.

An important step before code validation is the selection of a turbulence model. To simulate the high complex flow in the manifolds and headers, a proper selection of the turbulence model is required. There is a large number of turbulence models in the open literature to select from but none of these models can simulate all types of turbulent flows. The proper turbulence model selection is usually followed by comparison with experimental data. The need of turbulence modeling is explained in Sections 3.1.2 and 3.1.3 of Chapter 3.

1.4 Objectives of this Study

The objectives of this study are to:

1) Validate FLUENT, a three dimensional computational fluid dynamics CFD code, against experimental data for single phase flow distribution in multi-branch headers.

2) Study the effects of header geometry and inlet flow imbalance on the CFD predictions.

This work represents a preliminary validation of CFD for simulation of large-scale CANDU headers by investigating the code accuracy on representative and scaled geometries. The importance of this study to the nuclear safety analysis is that it validates the CFD techniques for future application in predicting header pressure and temperature gradients.

Chapter 2

Literature Review

In this chapter, a literature review is presented on the methods have been used for modeling and simulating CANDU reactor different components mainly the headers. The first section discusses the one-dimensional thermalhydraulic predictions for the CANDU reactor and shows how the headers have been modeled and treated. The second section reviews the CFD tools investigated for flow in large volumes and complex geometries in nuclear applications including the reactor headers. The third section reviews the CFD applications for headers and manifolds in other engineering applications.

2.1 One-Dimensional System Level Codes

The one-dimensional approximation of the nuclear reactor components has been adopted by several computer codes like CATHENA (Canadian Algorithm for THErmalhydraulic Network Analysis), NUCIRC (NUclear CIRCuits) and TUF (Two Unequal Fluids), where coarse nodalisation or control volumes are usually used.

To describe the fluid flow in CATHENA, for example, non-equilibrium, two-fluid model is used. Mass, momentum and energy balance equations are solved for each phase (in a two phase flow), resulting in a 6-equation model. Correlations obtained from literature or derived from single effect experiments are also used. To simulate the PHTS (for example), physical information on the components like the pump, steam generator and channel power need to be defined. The balance equations are numerically solved using a one-step, staggered domain, semi-implicit, finite-difference method [13]. The dependent variables calculated at each node include pressure, void fraction and phase enthalpies.

2.1.1 One-Dimensional Analysis of CANDU Headers

An accurate determination of the header to header pressure drop for each channel is very important as it is related to the flow rate in the channel to determine the channel critical power which is necessary to assess the safety margins.

The header manifold treatment has been introduced by Kwan [7] using NUCIRC code, which is a one-dimension cross-sectional averaged steady-state code where the full PHTS circuit was modeled (including inlet and outlet feeders, channels, headers, pumps, steam generators ...etc). The headers are subdivided into sections and each section is also divided into vertical planes as shown in Figure (7). Some sections contain 12 or 13 planes and each plane may contain up to 6 feeders. Each feeder location on the header is then identified by three numbers: the section, the plane and the feeder-in-plane numbers. In the analysis, the sections are treated as individual manifolds. However, to correctly simulate the whole header, the pressure of different sections is matched at a common plane between sections where the pressure must be the same.

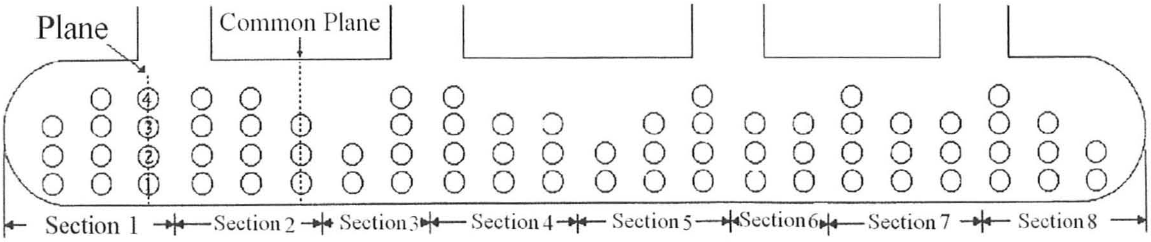

Figure (7): Simplified version of CANDU outlet header for one-dimensional analysis [7].

The manifold model for a large scale CANDU version header was found to predict a significant axial pressure gradient in the inlet header (up to 150 kPa) and in the outlet header (up to 60 kPa) [7]. Therefore, better determination of the header-to-header pressure drop in each fuel channel was obtained.

Holliday *et. al.* [4] used an empirical-based methodology to improve the one-dimensional CANDU inlet header pressure gradients. The loss factor in the links between the header regions was optimized based on station data available and attempted to determine the theoretical range of values this factor could attain.

Analytical models to obtain better predictions were developed. The flow rates in the channels and the pressure difference across the headers could be predicted by the solution of two pressure-flow ordinary differential equations. Chandraker *et. al.* [14] divided the outlet header of a Pressurized Heavy Water Reactor PHWR into several basic flow manifolds, and the pressure-flow equation set was solved using an iterative procedure to satisfy the flow and pressure conditions at each junction point between the manifolds. They validated their analytical model against experimental data of flow and pressure with (i) both header turrets were open and (ii) one of the turrets was closed. Good agreement between the analytical and the experimental results was noticed.

The above mentioned models do not consider the three-dimensional flow effects in the headers, but rather empirically account for these phenomena. Recently, there has been a move towards the use of CFD tools for the flow in large volumes and complex geometries in the nuclear industry. The following sections review some of the recent studies investigated the CFD tools for some components in PWR and CANDU reactors including the headers.

2.2 CFD for Nuclear Reactor Components

The flow in many nuclear reactor large components is essentially three-dimensional in nature, as in mixing, natural circulation and stratification. The three-dimensional aspects of flow in these components may have a significant impact on the safety analysis. The following subsections illustrate some applications where CFD tools were found to provide a better insight of some phenomena in nuclear industry.

2.2.1 Fluid Mixing in PWR

Mixing in a small scale test vessel of PWR was modeled using CFD tools [16]. The water in the test vessel was kept at constant temperature (74^{o}C) and cold water was injected into the vessel from one inlet. The temperature distribution inside the vessel was predicted using a mesh of 640,000 cells with the RNG k-ε turbulence model in FLUENT. The average temperature at the exit of the vessel was compared to experimentally measured temperature. Two approaches were followed for the transient analysis, one assuming constant fluid properties inside the vessel with no buoyancy and another with temperature dependent density and viscosity. The second approach was found to provide predictions within the uncertainty of the test results.

2.2.2 Flow in BWR Lower Plenum

The coolant in a Boiling Water Reactor (BWR) is pumped to the reactor core by several pumps through a lower plenum which consists of many pipes. One phenomena related to the reactor safety is the lack of flow uniformity between these pipes due to partial operation of the pumps. This operation may lead to a non uniform temperature distribution and thus it is important to check the three-dimensional flow behavior under such a condition. A CFD code has been used to model this case [17] and was found to successfully evaluate the flow field using the standard k-ε turbulence model.

2.2.3 Flow and Temperature Distribution inside CANDU Calandria Vessel

The interest of this subsection is in the moderator flow surrounding the fuel channels in the CANDU calandria vessel. Two major flows usually occur; forced flow from inlet nozzles and buoyant flow due to internal heating. The determination of the local subcooling of the moderator inside the calandria vessel is one of the major concerns in the CANDU safety analysis [18]. After a LOCA, the pressure tube may get into contact with the calandria tube and a subsequent dryout of the outer surface of the calandria tube may occur. The prevention of the tube contact depends on the local subcooling of the moderator. Secondary flows can exist among the fuel channels, which have an important role in fluid flow and heat transfer characteristics [18].

Kim *et. al.* [19] reported that it is necessary to analyze the three dimensional flow behavior inside the calandria vessel using the real geometry of the fuel channels. They investigated FLUENT for the prediction of experimental data of single phase (water) flow and temperature distributions inside a calandria-like vessel. The experimental data was obtained using 0.254 m long vessel with 0.737 m inside diameter. 52 copper tubes (0.254 m long and 0.038 m OD) were arranged inside the vessel. Two inlet nozzles from the top were used to inject water inside the vessel and electric heaters were used to heat the tubes. The temperature profiles inside the vessel were experimentally measured. To simulate this test, a CFD model was built using mesh of 5.3×10^4 cells adopted after a mesh sensitivity analyses they conducted. The turbulence behavior was modeled using the standard k–ε model combined with the standard wall treatment. Comparison with the experimental data showed that the CFD model can reasonably predict the temperature distribution of the moderator. Moreover, the secondary flows in the vicinity of calandria vessel wall and the fuel channels were found to play an important role in the heat transfer process.

2.2.4 Flow in a CANDU Fuel Bundle

Tavoularis *et. al.* [20] investigated the CFD tools for fully developed turbulent flow in a 60^{o} sector of a 37-fuel bundle. The sector geometry is a scaled-up model (1:12.8) of the real fuel bundle. FLUENT was used to solve the single phase (air) isothermal flow equations using the Reynolds Stress Model (RSM). The computations were conducted using 800,000 nodes mesh, which provided solutions that differ by less than 5% (in the local maximum velocity) compared to those obtained using a much finer mesh. It was found that the bundle geometry strongly affects the local velocity fluctuations, especially in the gaps between the bundle rods themselves and between the rods and the surrounding wall. The time-averaged mean velocity and the time-averaged Reynolds stresses were found to be in good agreement with experimental data.

Rock and Lighstone [2] studied the friction factor and turbulence structure of fluid thermal mixing in an array of rods using the standard k-ε turbulence model with standard wall treatment. The predictions were compared to published experimental data for a number of rod geometries (single row of unheated rods with different pith-to-diameter ratios). Single phase flow (air) was used with Re number ranging between 3×10^4 and 3×10^5.Different grid densities and placement of wall nodes were studied to determine a grid independent mesh. Mesh of 150,000 nodes was adopted and adequate prediction of the friction factor was obtained but the degree of mixing was underpredicted. That was explained to be due to the use of an isotropic turbulent viscosity model applied for a strongly anisotropic flow.

2.2.5 CFD for CANDU Headers

Several studies have been carried out to investigate the validity of CFD simulations in predicting flow distributions and pressure gradients in multi-branch geometries. This section reviews the studies done for some components of CANDU headers. The following section reviews CFD tools investigated for headers in other engineering applications.

Moffet *et. al.* [6] calculated the pressure and flow distributions inside a CANDU-6 reactor inlet header using one- and three-dimensional models (using NUCIRC and CFDS-FLOW3D codes; respectively). For the three-dimensional model, coarse and fine meshes were used consisting of 14,868 and 62,139 cells; respectively, and the k-ε turbulence model was selected. The sensitivity to grid density showed a difference in pressure of less than 3 kPa along the axial centerline of the header. They also found that the three-dimensional effects were able to capture some variations between feeder pressures in a given header cross-section, especially near the inlet of the header. The one-dimensional calculations for the CANDU-6 reactor header were recommended to be further refined.

The validity of using CFD results in a header-to-branch flow as a series of experimental results to develop a correlation that can be implemented to one-dimensional accident analysis codes instead of doing experiments was also examined by Cho *et. al.* [21]. The physical modeling of experiments (air-water flow in 58 mm ID horizontal pipe with one outlet branch of 0.635 mm ID) at system pressures of 316 and

517 kPa was implemented into the three-dimensional CFX10 code using a mesh of 1,075,228 cells. The standard k-ε turbulence model was selected. It was found that the CFD results could be successfully used to develop the correlation.

In a recent study, FLUENT was used to simulate two-phase flow behaviour in the RD-14M header (a reduced scale CANDU facility, involving only five header feeders and five heated channels) [22]. By comparing vapour phase distribution obtained by FLUENT with experimental data; FLUENT provided good predictions when the discrete-phase model was used to simulate the vapour entrainment since it tracks every vapour bubble. The discrete-phase model was also used to simulate feeder vapour entrainment and two-phase injection into the header turret. It was reported that the vapour-phase behaviour analysis could be useful in accident analyses.

M. An *et. al.* [23] analyzed the role of the header flow conditions in flow reversal in two heated channels of the RD-14M facility. The purpose was to determine the PHOENICS (a CFD code) calculated header outflows when using CATHENA predictions of void and phase velocities as boundary conditions and compared these with measurements. It was found that the flow conditions within the header may not be responsible for initiating the flow reversals in the two heated sections. However, they concluded that the procedure of header partition into pressure/void segments in the RD-14M is not applicable in the full scale CANDU header.

2.3 CFD for Headers in General Engineering Applications

CFD tools have also been used to model manifolds in other engineering applications. The design of these manifolds is different than the reactor headers design but these studies are important as they provide investigation of CFD tools for flow in multi-branch geometries.

In a separate effects experiment, Y. Li *et. al.* used FLUENT to predict single phase (air) flow distributions in plate-fin manifold (one inlet and eleven downward outlets) [24]. The inlet of the manifold is 40 mm in diameter and the manifold is 250 mm in length. A mesh with 150,000 cells was built and the standard k-ε turbulence model was selected. The results were validated against experimental data at Re=2100 and it was found that the CFD predictions are in good agreement with the experiment. The effects of different header configurations were investigated in order to optimize the header design to have the minimal effect on flow maldistribution. Three header shapes were compared, one with a single-stage (cylindrical header with one inlet and eleven downward outlets), and the others with a two-stage distributing structure through which the flow can be distributed two times (composed of the single-stage header attached to a second header with 5 or 7 holes in between and eleven downward outlets at the second header). The optimum header configuration found was the third type, which is a two-stage distributing header with a ratio of equivalent diameters.

CFD was also used to simulate single phase (water) flow in a manifold (consisting of tapered rectangular duct with 30 upward vertical outlets) [25]. The inlet of the duct is 0.6 m in diameter and each outlet is 0.5 m long and 0.01 m ID. Coarse and fine meshes were used consisting of 48,050 and 91,605 nodes; respectively. The standard k-ε turbulence model with standard wall treatment was selected. The inlet velocity was 1 m/s. They found that the computational method developed had the ability to model the complex geometry of the manifold. However, the results were not compared to experimental data.

An investigation of the candidate turbulence model for the flow in a distribution header has been performed by Sparrow *et. al.* [26]. They considered three turbulence models and compared the CFD prediction to experimental data. The investigated models were the standard, RNG and the realizable k-ε models. The experiments were carried out for a single phase (air) flow in a cylindrical pipe (304.8 cm long and 4.7 cm ID) fitted with an array of rectangular discharge slots distributed axially and uniformly along the length of the chamber. The slot axial dimension is 0.159 cm and 0.0159 in width. Each slot is axially spaced 0.318 cm from its neighbor slots. The computations were performed for Re of 40,000 and 200,000. Two mesh densities were investigated, coarse one with 236,600 control volumes and finer one with 1,695,700 control volumes. No difference in solution was noticed using both meshes and thus the coarse mesh was adopted. The realizable model provided best fit of the outlet flow rates for the entire range of Re number and it gave excellent agreement with the data (within ±4.7%).

From the literature review presented above, no full study was found that investigates the flow modeling effects (i.e turbulence modeling), the solution parameters effects (i.e grid density and convergence criteria), header geometrical effects and the effects of flow imbalance levels for cylindrical headers similar to the CANDU geometry.

In this study, a CFD analysis is conducted for multi-branch headers in order to predict flow and pressure distributions along the headers taking into consideration the previous mentioned effects. The computational results were compared with experimental data for single phase flow in a scaled facility with reduced Reynolds number. In some of the experimental runs, Reynolds number was set to low values with high level of flow imbalance to represent loss of flow scenarios. This work represents a detailed validation of CFD for simulation of CANDU header gradients using scaled experimental facilities.

Chapter 3

CFD Mathematical Model, Codes Description and Method of Solution

In this chapter, the following is presented: the three-dimensional header mathematical model, a brief description of the codes used for the simulation (GAMBIT and FLUENT), and the adopted method of solution (the SIMPLE method).

3. 1 CFD Mathematical Model

The model equations were derived by considering a finite control volume element within the header and applying the following conservation equations:

3. 1. 1 Mass Conservation Equation

The unsteady, three-dimensional mass conservation equation (the continuity equation) for a compressible fluid is:

$$\frac{\partial \rho}{\partial t} + \frac{\partial (\rho u_i)}{\partial x_i} = 0 \tag{1}$$

where, ρ: is the fluid density (kg/m^3).

t: time (s).

u_i: fluid velocity components (m/s) where i denotes the coordinates.

x_i: spatial coordinates (m).

The first term represents the rate of change of the density in time. The second term represents the gradient of mass change. Steady state conditions and incompressible fluid are assumed in this study.

3. 1. 2 Momentum Conservation Equations

The three-dimensional momentum conservation equations in the spatial directions are:

$$\frac{\partial(\rho u_i)}{\partial t}+\frac{\partial(\rho u_i u_j)}{\partial xj}=-\frac{\partial p}{\partial x_i}+\frac{\partial \tau_{ij}}{\partial x_j}+\rho g_i+F_i \qquad (2)$$

where,

p: pressure (Pa)

τ_{ij}: shear stress at *ij* surface (N/m^2)

g_i: the gravitational acceleration (m/sec^2).

F_i: external body force (N/m^3).

Each momentum equation was derived by setting the rate of change of the momentum in that component direction equal to the net force acting on the element in that direction (due to the surface stress) plus the gravitational and external forces.

The shear stress term is defined as:

$$\tau_{ij}=-\rho u_i u_j=-\frac{2}{3}\mu\frac{\partial u_l}{\partial x_l}\delta_{ij}+\mu\left(\frac{\partial u_i}{\partial x_j}+\frac{\partial u_j}{\partial x_i}\right) \qquad (3)$$

where, μ: is the molecular viscosity (Pa. s).

δ_{ij}: is the delta function.

The first term at the right hand side represents the effect of volume dilation.

The most accurate numerical method to solve for turbulent flows is by directly solving the Navier-Stokes equations in the so-called Direct Numerical Solution (DNS) approach [26]. However, this approach is too complex and time consuming to solve and applicable only to flows at low Re number with simple flow geometries.

Instead, the Navier-Stokes equations are usually averaged to give Reynolds-Averaged Navier-Stokes equations (RANS). The flow variables (such as velocity and pressure) are decomposed into a mean and turbulent fluctuating part as shown in Figure (8).

$$U_i(t) \equiv U_i + u_i(t) \tag{4}$$

where, $U_i(t)$: is the flow velocity (m/s).

U_i: is the flow mean velocity (m/s).

$u_i(t)$: is the flow turbulent fluctuating velocity (m/s).

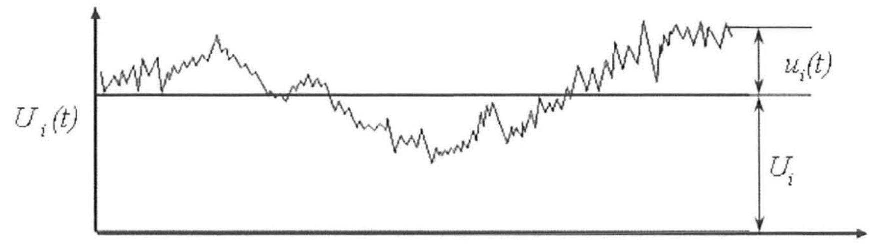

Figure (8): Velocity decomposition into mean and fluctuating parts [28].

The mean velocity is obtained by integrating the flow velocity over a time scale that is large enough in comparison with the time scale of the turbulent fluctuations. Reynolds averaging is defined as follows:

$$U_i = \lim_{T\to\infty}\frac{1}{T}\int^{t+dt} u_i(t)dt \tag{5}$$

where, T: is the large time scale (s).

In FLUENT, the RANS equations for a steady, incompressible flow are [28]:

$$\rho U_k \frac{\partial U_i}{\partial x_k} = -\frac{\partial p}{\partial x_i} + \mu\frac{\partial^2 U_i}{\partial x_j \partial x_j} + \frac{\partial R_{ij}}{\partial x_j} \tag{6}$$

and

$$R_{ij} = -\rho U_i U_j = -\rho\frac{2}{3}k\delta_{ij} + \mu_t\left(\frac{\partial U_i}{\partial x_j} + \frac{\partial U_j}{\partial x_i}\right) \tag{7}$$

where, μ_t: is the turbulent viscosity (Pa. s).

R_{ij}: Reynolds shear stress.

As a result of averaging, the turbulent viscosity arises which needs to be modeled. Several modeling methods are available: one-equation (Spalart-Allmaras) model, two-equation models (k-ε models), Reynolds Stress Model and Large Eddy Simulation. The following section discusses a two-equation model (k-ε model).

3. 1. 3 Turbulence Model

As a result of the averaging, the universality of the model is lost and thus some information about the dynamics of the turbulence is eliminated. A large number of turbulence models have been developed to approximately account for the effects of turbulence. Therefore, the selection of a turbulence model must be validated by comparison with experimental data. For Two-Equation models, the turbulent viscosity is correlated with turbulent kinetic energy, k, and dissipation rate of turbulent kinetic energy, ε, as follows:

$$\mu_t = \rho C_\mu \frac{k^2}{\varepsilon} \tag{8}$$

where:

$$k = U_i U_i / 2 \qquad \varepsilon = \mu_t \frac{\partial U_i}{\partial x_j}\left(\frac{\partial U_i}{\partial x_j} + \frac{\partial U_j}{\partial x_i}\right) \tag{9}$$

and C_μ is a constant.

Transport equations for k and ε are solved so that the turbulent viscosity can be computed for RANS equations.

In FLUENT there is a list of turbulence models to select from; namely they are: Sparlart-Allmaras model, k-ε models (standard, RNG and Realizable) and k-ω models [28]. In this study, these models were initially investigated (as well as the laminar model). Table (1) describes and summarizes the applications of the k-ε models which found to provide the most reasonable predictions. The adopted model should provide good agreement with experimental data and should not be computationally expensive

Table (1): Summary and description of k-ε turbulence models [28].

Turbulence Model	**Description**	**Application**
Standard k-ε	Two-equation model. Assumes isotropic eddy viscosity. Robust, stable and economical, poor for very complex flows.	Poor for severe pressure gradients.
RNG k-ε	Has an additional term in ε equation. Assumes isotropic eddy viscosity. Accounts for the different scales of motion.	Suitable for moderately complex separation, recirculation and swirl flows for wide range of Re.
Realizable k-ε	New formulation of turbulent viscosity and new equation for ε.	Suitable for flows with boundary layers under strong adverse pressure gradient.

Taking the standard k-ε model as an example, the two transport equations are:

$$\underbrace{\rho U_i \frac{\partial k}{\partial x_i}}_{convection} = \underbrace{\mu_t \left(\frac{\partial U_j}{\partial x_i} + \frac{\partial U_i}{\partial x_j} \right) \frac{\partial U_j}{\partial x_i}}_{generation} + \underbrace{\frac{\partial}{\partial x_i} \left\{ (\mu_t / \sigma_k) \frac{\partial k}{\partial x_i} \right\}}_{diffusion} - \underbrace{\rho \varepsilon}_{destruction} \tag{10}$$

$$\underbrace{\rho U_i \frac{\partial \varepsilon}{\partial x_i}}_{convection} = \underbrace{C_{1\varepsilon}\left(\frac{\varepsilon}{k}\right)\mu_t\left(\frac{\partial U_j}{\partial x_i}+\frac{\partial U_i}{\partial x_j}\right)\frac{\partial U_j}{\partial x_i}}_{generation} + \underbrace{\frac{\partial}{\partial x_i}\left\{(\mu_t/\sigma_\varepsilon)\frac{\partial \varepsilon}{\partial x_i}\right\}}_{diffusion} - \underbrace{C_{2\varepsilon}\rho\left(\frac{\varepsilon^2}{k}\right)}_{destruction} \quad (11)$$

Where, σ_k, σ_ε, $C_{1\varepsilon}$, $C_{2\varepsilon}$ are empirical constants.

The selection of the proper turbulence modeling is discussed in Chapter Five: Results and Discussion for each validation case separately.

3. 1. 4 Near Wall Treatment

The near-wall region is important in turbulence flow modeling as it is the main source of turbulence and large gradients exist in this region. Thus, accurate turbulence modeling requires successful treatment of the near wall effects.

FLUENT provides three methods of near-wall treatment for turbulent flows. These methods are: standard, non-equilibrium and enhanced wall treatment. The first two methods use empirical-based functions (wall function approach) whereas the third method resolves turbulence all the way to the wall and thus finer mesh resolution is required (modeling approach). Figure (9) shows a mesh graphical representation of the near-wall treatment methods. The advantages and weaknesses of these methods are summarized in Table (2).

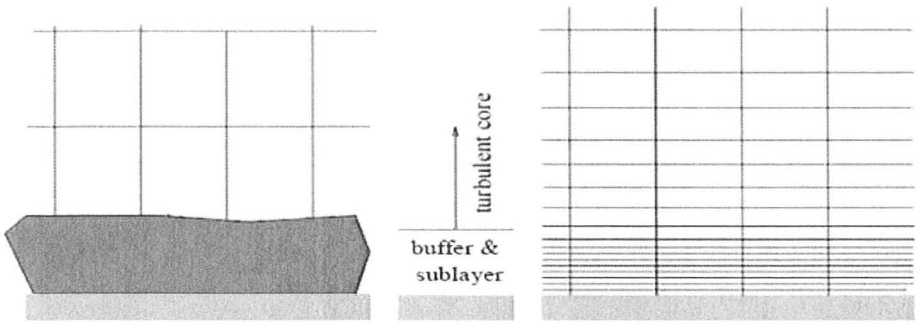

Wall function approach Modeling approach

Figure (9): Mesh graphical representation of the near-wall treatment methods [28].

Table (2): Near wall treatment methods in FLUENT [28].

Method	Advantage	Weakness
Standard	Robust and economical.	Poor for highly 3-dimentional effects
Non-Equilibrium	Accounts for moderate pressure gradients, allows non-equilibrium separation and reattachment.	Poor for low Re flows, highly 3-dimentional effects and severe pressure gradients.
Enhanced	Good for complex flows, does not use empirical function.	The mesh near wall must be fine enough to have a Y^+ value between 1 and 5*.

* Y^+ is discussed in Section 5.1.3.2 of Chapter 5: Results and Discussion.

The turbulence model and the wall treatment method were varied when solving the problems to find the optimum combination of turbulence model and wall treatment method.

3.2 Codes Description

3.2.1 GAMBIT

GAMBIT is a software package designed to build and mesh geometries for CFD. GAMBIT receives user input by means of its graphical user interface (GUI) which provides geometrical objects with different shapes that can be combined to form any desired geometry. Also, it serves the CFD analysis by providing different types of meshes on the base geometry [29].

3.2.2 FLUENT

FLUENT is a CFD three-dimensional, multi-phase computer code for modeling fluid flow and heat transfer in complex geometries, written in the C programming language. Once a mesh has been exported into FLUENT, the remaining operations include: defining fluid material/s and properties from a built-in database (user defined material and properties is also allowed), setting initial, operating and boundary conditions, and selection of mathematical model. Upon solving the model, number of iterations, tolerance value, relaxation factors … etc. can be controlled. Finally, results can be displayed in various formats.

The code shows 2D and 3D flows in either steady state or transient applications. Flows can be solved using Inviscid, laminar, or turbulence models. Newtonian or non-Newtonian flow solutions are also provided [28].

3.3 Method of Solution

The Semi-Implicit Method for Pressure Linked Equations (SIMPLE) [30] in FLUENT was adopted to solve the model equations. In this method, initial profiles of pressure and velocity along the header are assumed. The equations are solved in three steps: the momentum equation is linearized, discretized and solved to give the velocity profile for the guessed pressure. The resulting velocity is not correct unless it satisfies the continuity equation. In the second step, the conservation of mass equation is linearized, discretized and used to correct both pressure and velocity profiles. In the third step the discretized turbulence equation(s) is (are) solved. In each step, a Tri-Diagonal Matrix Algorithm (TDMA) is used to solve the descritized equation and convergence is ensured before going to the next step loop. Second-order discretization scheme was selected.

The boundary and operating conditions are listed for each validation case in Chapter Five: Results and Discussion.

Chapter 4

Experimental Setup and Methodology

Three validations have been performed, one against experimental data obtained from literature, and two against data obtained from experiments done in this study. The following sections describe the experimental setups and the methodology followed in each experiment.

4.1 First Validation: Header with Upward Flow Outlets

In this validation, FLUENT predictions of flow distribution and pressure gradients along a horizontal header with vertical outlets were compared to data obtained by Horiki [11] for single phase flow (water). The effects of flow modeling, grid density, convergence criteria, flow inlet velocity and header size on the solution were investigated.

4.1.1 Experimental Apparatus and Data

The experimental setup (used in Horiki experiment) consists of a horizontal rectangular header with four upward vertical cylindrical branch outlets. The dimensions of the header are 10 mm × 40 mm ×1000 mm and the distance between the entrance of the header and the first branch is 600 mm which is enough to ensure fully developed flow. The branches are connected to the header at intervals of 130 mm. The branches are

1000 mm long and 10 mm in diameter. A schematic of the header is shown in Figure (10). The header and the branch pipes were made of transparent acrylic resin to observe the flow pattern.

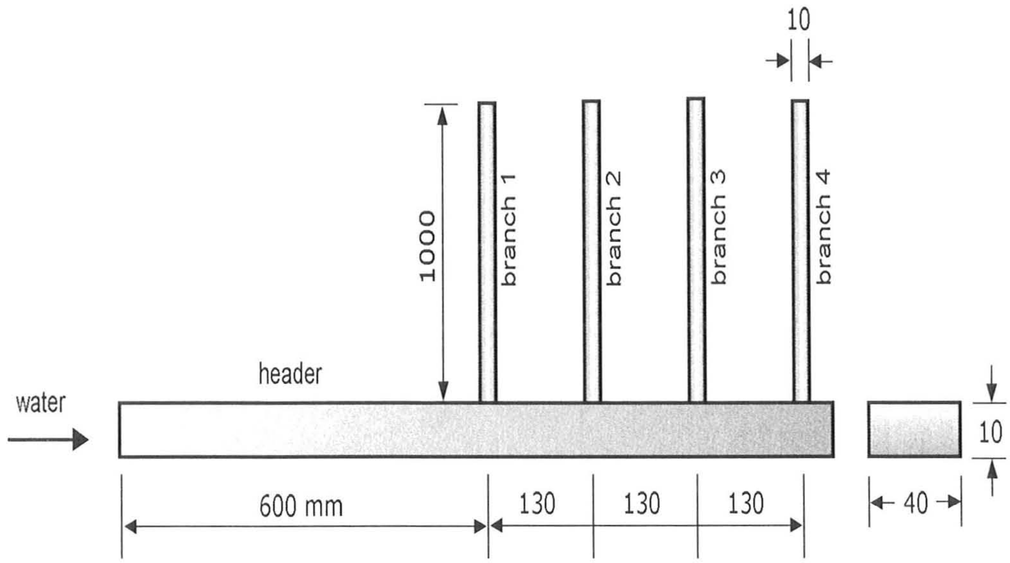

Figure (10): Schematic of the experimental header of first validation (all dimensions are in mm).

A constant static head tank was used to supply the feed water. The water outlet flow rates were found by measuring the time needed to accumulate a known amount of water. The inlet flow Reynolds number was varied from 817.3 up to 4629.5 and isothermal flow was assumed. The collected data consists of flow rate in each branch pipe for each inlet flow rate. Using the flow data, Horiki [11] used a 1-dimentional model to calculate the pressure gradients along the header. In this study, the CFD predictions were compared against the calculated pressure. Furthermore, 2 μm aluminum particles were injected with the inlet flow in order to visualize the flow pattern and vortex formation. CFD predictions were also compared to these observations.

In their study, other header sizes were also used, one header with inlet cross section of 40 mm× 40 mm and two headers with 2000 mm and 10,000 mm branch lengths; respectively. FLUENT was also validated against data obtained for these headers to investigate the effect of header size on the validation. The experimental data is shown in Appendix A.

4.2 Circular Header with Horizontal and Vertical Outlets

In this validation, flow distribution data along a horizontal cylindrical header with vertical and horizontal outlets was collected under varying levels of inlet flow imbalance for single phase flow of water. Validation was performed for vertical and horizontal inlet flows. The effects of flow modeling, grid density, convergence criteria, inlet flow level of imbalance, and header geometry on the solution were investigated.

4. 2. 1 Experimental Apparatus and Data

The experiments were carried out using 1.0 m long, 3.67 cm ID horizontal cylindrical Lucite header with two symmetrically distributed vertical inlets or two horizontal inlets at the two header far edges. Either the vertical or horizontal inlets are selected for a given test. The flow is distributed to five horizontal and five vertical outlets along the header with 0.92 cm ID. A schematic of the header is shown in Figure (11). A unique feature of this experiment is that it allows flow imbalances to be controlled and also allows for flow injection from either the top of the header or from the ends. This allows the experiment to mimic the design of different CANDU headers (Darlington and Bruce reactor headers).

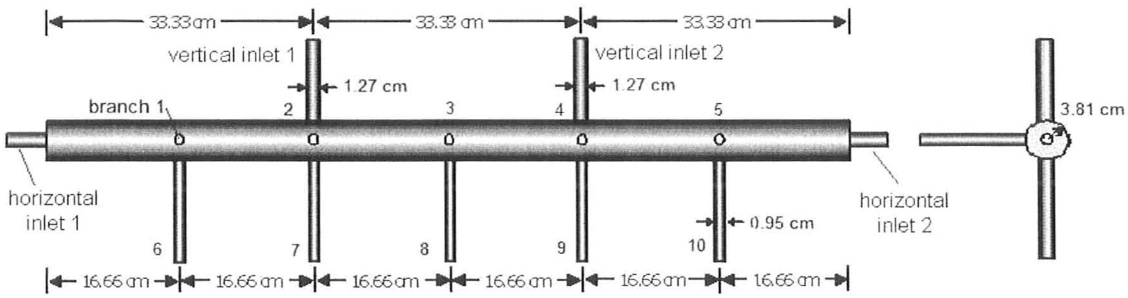

Figure (11): Schematic of the experimental header of second and third validations (length measurement accuracy ± 0.01 cm).

The length of each inlet pipe is 209 cm (from the source to the header) and is adequate to establish fully developed flow. The inlet flow is measured with two Vortex shedding flowmeters (FV100 type) with a built-in display with accuracy of ±0.037 kg/s. The outlet flow is measured with Vortex shedding flowmeters (FLR1012 type) with accuracy of ±0.0025 kg/s, through a Data Acquisition System DAS (Keithley 3700 Series). The operational fluid was water flowing at a temperature between 8-12 ^{o}C. The flow rate in each inlet was varied between 0 and 0.307 kg/s. Water flows out to drain at atmospheric pressure. The collected data consists of a set of flow rates in each branch pipe for each inlet flow configuration. An image of the physical setup is shown in Figure (12).

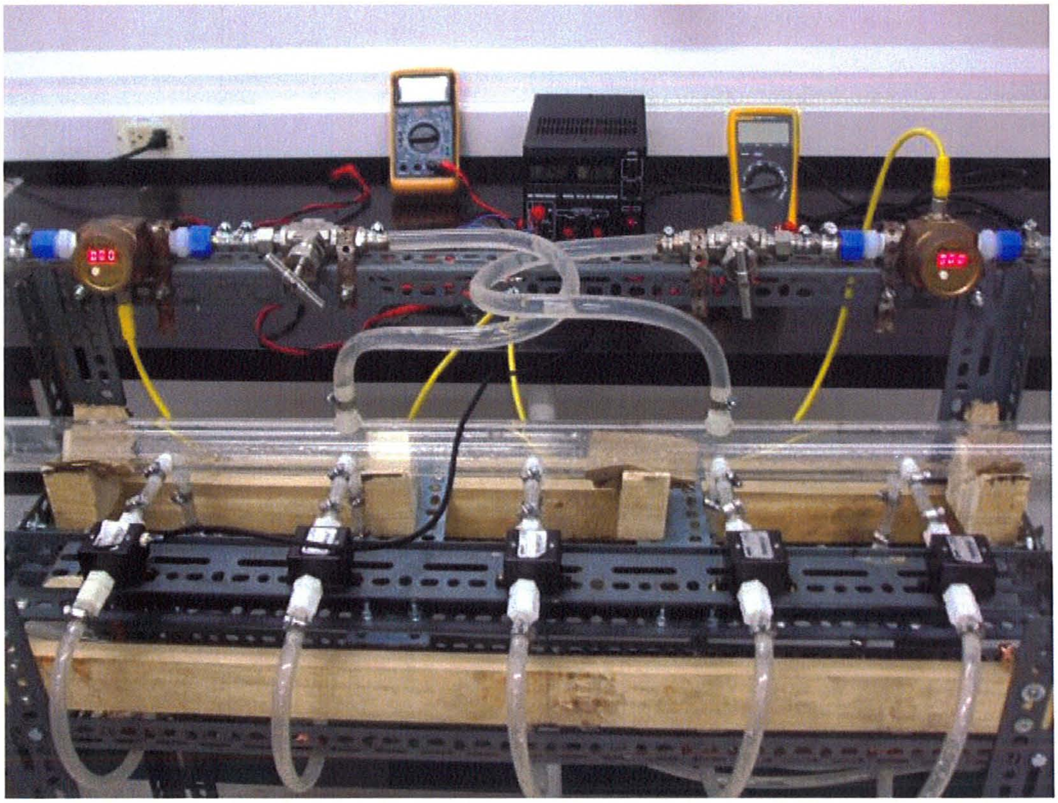

Figure (12): Image of the experimental setup.

4. 2. 2 Measurement Uncertainty

4. 2. 2. 1 Inlet Flow Meters

The operating range of the Vortex shedding flow meters (FV100 type) is 4.5-45.5 L/min with accuracy better than 5% of full scale flow (which equals ±0.037 kg/s). They work best with non-viscous, clean water-like liquids. The inlet flowmeters were calibrated and the calibration curves are shown in the Appendix B.

4. 2. 2. 2 Outlet Flow Meters

The operating range of the Vortex shedding flow meters (FLR1012 type) is 0.2-5 L/min with accuracy better than 3% of full scale flow (±0.0025 kg/s). They work best with non-viscous, clean water-like liquids.

4. 2. 3 Methodology

4. 2. 3. 1 Experimental Procedure

The following procedure was followed to collect the data:

1. The power supply of the DAS was turned on, set to 24 V.
2. The water supply was initiated and the header became full of continuously running water.

3. All air bubbles were removed from the system and the header was adjusted to be horizontal.
4. The valves at the inlet lines were used to control the inlet flow rates appearing on the inlet flow meters displays.
5. The header was run for 5 minutes to assure steady state conditions and to assure stable readings at the flowmeters displays.
6. For the horizontal-inlet header configuration, the data acquisition system was used to record the outlet flow rates for 1 minute. The inlet flow rates were also recorded.
7. The inlet flow rates were then set to zero by closing the water taps for 30 minutes prior to conducting the next test.
8. For each inlet flow rate configuration, the procedure was repeated 10 times and the average of all tests was determined. For the vertical-inlet header configuration, 3 repeat trials were done.
9. When finished, all water was drained from the header.

The tests were done for the inlet flow sets shown in Table (3) for the vertical-inlet header and in Table (4) for the horizontal-inlet header.

Table (3): Summery of experimental runs and inlet flow rate sets (vertical-inlet header configuration).

Inlet 1 / Inlet 2 ((kg/s)/(kg/s)) (±0.0025 kg/s)					
Run	**1**	**2**	**3**	**4**	**5**
1	0.307/0.307	0.307/0.232	0.307/0.158	0.307/0.083	0.307/0.0
2	0.232/0.307	0.232/0.232	0.232/0.158	0.232/0.083	0.232/0.0
3	0.158/0.307	0.158/0.232	0.158/0.158	0.158/0.083	0.158/0.0
4	0.083/0.307	0.083/0.232	0.083/0.158	0.083/0.083	0.083/0.0
5	0.0/0.3077	0.0/0.232	0.0/0.158	0.0/0.083	---

In the following chapters the Runs will be named according to column and line numbers of this Table, e.g. Run 2/3 represents the shaded cell.

Table (4): Summery of experimental runs and inlet flow rate sets (horizontal-inlet header configuration).

Inlet 1 / Inlet 2 ((kg/s)/(kg/s)) (±0.0025 kg/s)					
Run	**1**	**2**	**3**	**4**	**5**
1 H	0.232/0.307	0.232/0.266	0.232/0.232	0.232/0.199	0.232/0.166
2 H	0.307/0.307	0.307/0.232	0.307/0.158	0.307/0.083	0.307/0.0

Chapter 5

Results and Discussion

5.1 First Validation: Header with Upward Flow Outlets

5.1.1 Geometry and Mesh Generation

A sample of mesh created by GAMBIT is shown in Figure (13). Boundary layers were created near the walls. The boundary layer tool in GAMBIT allows controlling how the mesh is refined near walls and boundaries. Using a boundary layer, the mesh grows out from the wall into the domain. It is used to locally refine the mesh in the direction normal to a wall or a boundary [29]. The shown mesh consists of 5.88560×10^5 cells; 1.798708×10^6 faces; and 6.24361×10^5 nodes. Three grid densities (1.51230×10^5, 6.24361×10^5 and 2.570242×10^6 nodes) were investigated to study the effect of grid density on the solution (Section 5.1.3). Maximum value of cell skewness coefficient is 0.8 which is the limit recommended by FLUENT.

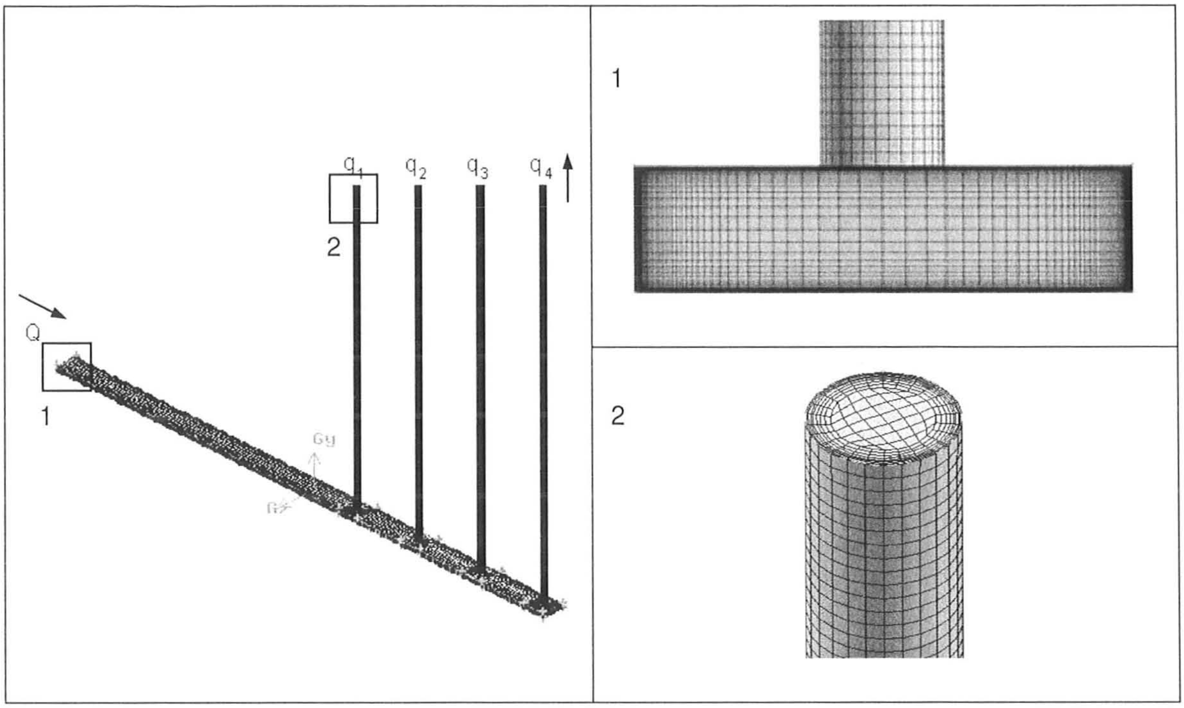

Figure (13): Sample of mesh created by GAMBIT consisting of 6.24361×10^5 nodes.

5.1.2 Boundary and Operating Conditions

Table (5) shows the boundary and operating conditions assigned in FLUENT.

Table (5): Boundary and Operating Conditions assigned in FLUENT (for first validation).

Condition	Value	Unit
Operating fluid	water	---
Inlet Re (range)	817.3 – 4,629.5	---
Gravity	9.81	m/s^2
Outlet pressure	101325	Pa

Incompressible, isothermal flow was assumed and pressure-based solver with implicit formulation was selected. Second-order discretization scheme was selected.

5.1.3 Sensitivity Analysis

5.1.3.1 Selection of Grid Density

Several grid densities were used to study the effect of grid density on the solution. A coarse mesh of 1.51230×10^5 was initially used. The mesh was then further refined until no change in the solution was noticed using two successive grid densities. The grid density beyond which no change noticed in the solution was adopted and used in the rest of this work.

The adopted mesh consists of 6.24361×10^5 nodes. Figure (14) shows the flow in branch 2 and branch 3 branch obtained using three grid densities (1.51230×10^5, 6.24361×10^5 and 2.570242×10^6 nodes). Very small difference (less than 5%) in solution is noticed when using the adopted and the finest meshes. The average run time using the finest mesh (with k-ε turbulence model) was around 12 hours. With the adopted mesh it was around 90 minutes using 1.86 GHz processor.

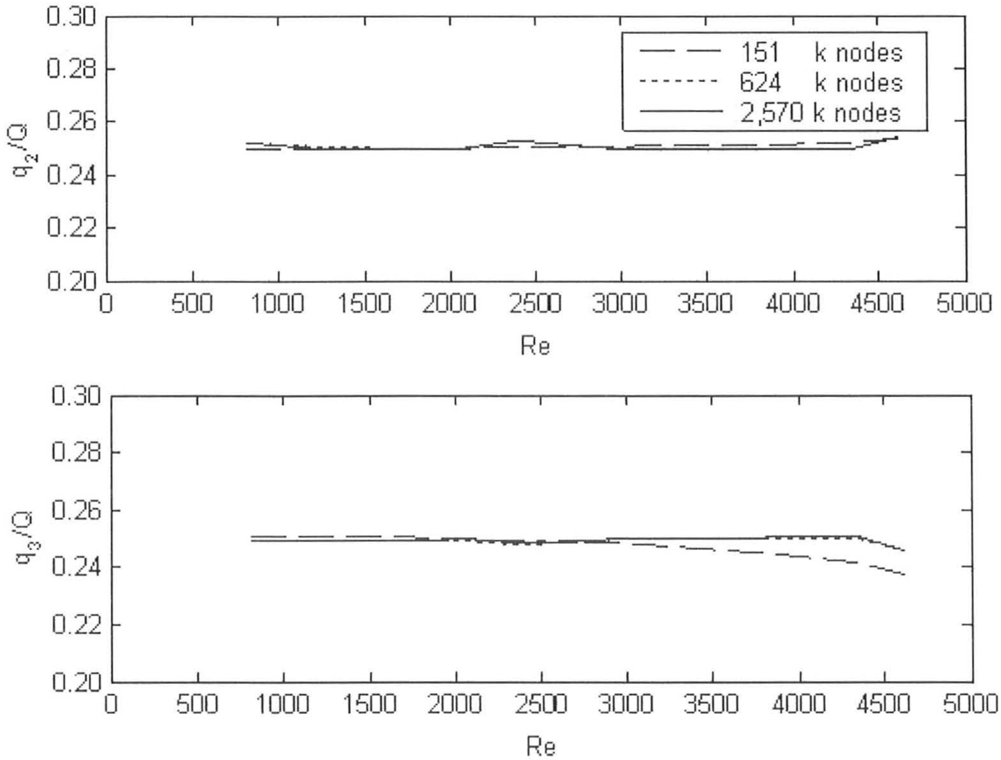

Figure (14): Effect of grid density on the flow in branch 2 and branch 3 (outlet flow rates are represented as ratios of the total inlet flow rate).

5.1.3.2 Selection of Turbulence Model

Laminar, k- ε models (standard, realizable and RNG), k-ω models (standard and SST) were investigated. With the k-ε models, standard, non-equilibrium and enhanced wall treatments were investigated. Other models were tested but provided bad predictions, thus they are excluded. Initially, standard k-ε model with standard wall treatment was used. The wall treatment methods were tested with each turbulence model to find the optimum combination of turbulence model and wall treatment.

The results are shown in Table (6) where the prediction error is calculated for each combination of turbulence model/wall treatment. The error is calculated as the sum of the absolute errors of the four branches for each run as follows:

$$\text{Error} = \sum_{i=1}^{4} \left| \left(\frac{q_i}{Q}\right)_{\text{Exp}} - \left(\frac{q_i}{Q}\right)_{\text{FLUENT}} \right| \quad (12)$$

Table (6): Prediction error (difference) for each combination of turbulence model/wall treatment.

Inlet Re / Model*	817.3	1217.4	1659.8	2069.0	2389.1	2943.5	3457.8	3915.1	4343.7	4629.5
Laminar	0.1300	0.1055	0.0621	0.0394	0.0374	0.0436	0.0354	0.0438	0.0406	0.0410
k-ε STD/STD	0.1372	0.0936	0.0588	0.0325	0.0261	0.0336	0.0255	0.0325	0.0230	0.0310
k-ε STD/NEQ	0.1245	0.0901	0.0528	0.0279	0.0158	0.0223	0.0217	0.0211	0.0230	0.0270
k-ε STD/ENH	0.0786	0.0588	0.0329	0.0181	0.0118	0.0194	0.0138	0.0172	0.0217	0.0221
k-ε RNG/STD	0.1187	0.0968	0.0579	0.0326	0.0262	0.0324	0.0260	0.0331	0.0242	0.0350
k-ε RNG/NEQ	0.1209	--	0.0546	--	0.0167	--	0.0217	--	0.0228	0.0238
k-ε RNG/ENH	0.1261	0.0978	0.0581	0.0325	0.0256	0.0322	0.0256	0.0324	0.0248	0.0370
k-ε REAL/STD	0.1223	--	0.0565	--	0.0232	--	0.0241	--	0.0252	0.0291
k-ε REAL/NEQ	0.1201	--	0.0541	--	0.0173	--	0.0219	--	0.0227	0.0264
k-ε REAL/ENH	0.124	--	0.0563	--	0.0207	--	0.0226	--	0.0243	0.0303
k-ω/STD	0.1273	--	0.0568	--	0.0185	--	0.0277	--	0.0310	0.0346
k-ω/SST	0.1282	--	0.0597	--	0.0230	---	0.0281	--	0.0287	0.0356

* (STD: Standard, NEQ: Non-Equilibrium, ENH: Enhanced, REAL: Realizable, SST: Shear Stress Transport).

From Table (6) it is concluded that the k-ε standard model with the enhanced wall treatment provides the best data fit among all other models. This combination is used in the rest of the first validation work.

The used mesh can be evaluated by looking at the Y^+ value; the mesh-dependent dimensionless distance that quantifies to what degree the wall boundary layer is resolved.

Y^+ is defined as:

$$Y^+ = \frac{\sqrt{\rho \tau_w}\, Y}{\mu} \tag{13}$$

Where: Y^+: the non-dimensional wall distance.

Y: the physical wall distance (m).

τ_w: shear stress at the wall (N/m^2).

In using the enhanced wall treatment with the k-ε model, the recommended Y^+ value is ≈ 1 and can go up to 5. In Figure (15) the Y^+ is plotted versus the position at the wall for Re=4,343.7. The shown value is around 1.8 < 5 (ignoring the anomalies at the inlet) which means the near-wall resolution is in the most accurate region to which the boundary layer can be resolved [28].

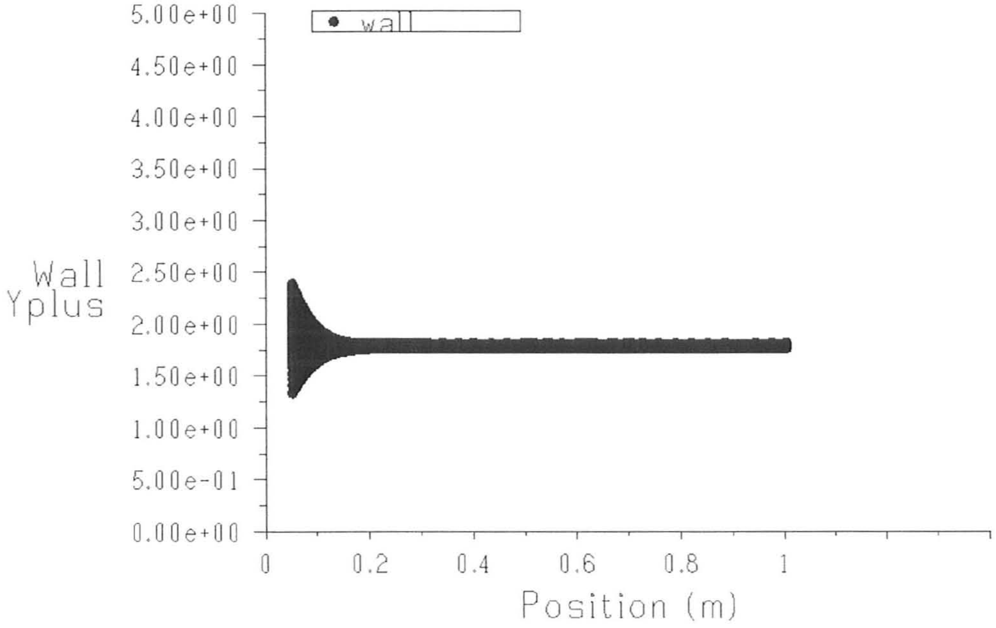

Figure (15): Y^+ value near the wall (Re=4,343.7).

5.1.3.3 Convergence Criteria

Sensitivity analysis of flow distribution and pressure gradients to convergence criteria has been conducted. The tolerance was initially set to FLUENT default's value (10^{-3}) and then decreased. No significant change in solution (less than 1%) was noticed when it was decreased from 10^{-5} to 10^{-6} and thus the tolerance was set to 10^{-5} in the rest of this work as it is precise enough for the present study and no significant change in solution occurs by further tightening.

5.1.4 Flow Distribution Results

In Figure (16), the experimental and predicted outlet flow rate in each branch is plotted (as ratio to the total outlet) versus the inlet flow Re number. Good agreement between FLUENT and the experiment is noticed.

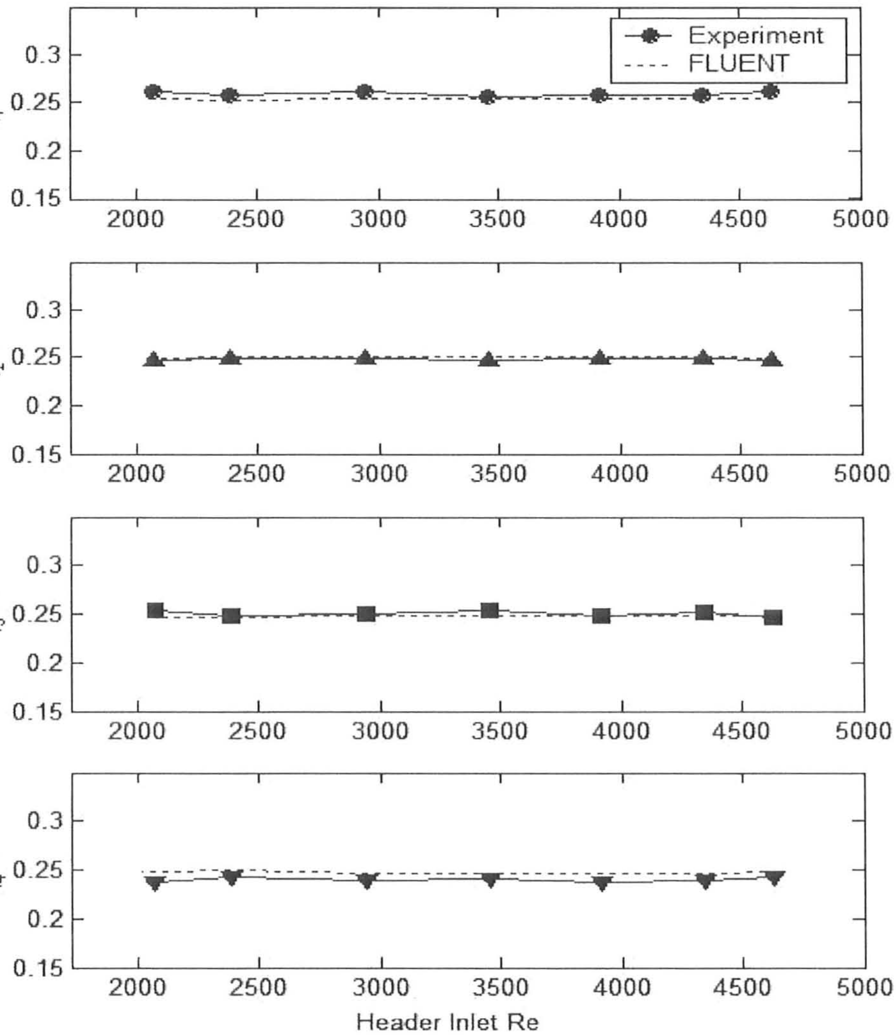

Figure (16): Experimental data and FLUENT predictions of flow distribution in the branches as a function of inlet Re number (measurement uncertainty was not reported in Horiki's paper).

The flow distribution in the branches for three selected Re numbers (Re=2943, 3457 and 4343) are plotted versus the branch number in Figure (17). As Re number increases, the flow in the first two branches decreases and increases in the last two branches. This behavior is due to the higher pressure pushing the fluid towards the end of the header as Re increases. Similar behavior was also noticed for other Re numbers.

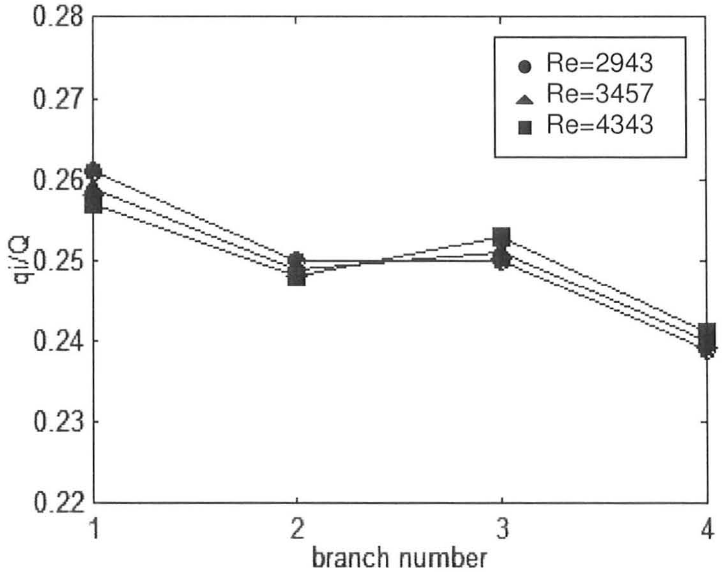

Figure (17): Flow distribution in the branches for several Re numbers.

In Figure (18) velocity contours are plotted at five different planes taken around the first branch for Re=1,217. The flow is uniform at planes A and B. At plane C, just after the branch, the flow is disturbed as a result of flow separation to the branch. The flow returns uniform downwards the branch as shown in plane D. At plane E, just after the branch inlet, the velocity is high as a result of the decrease in flow area.

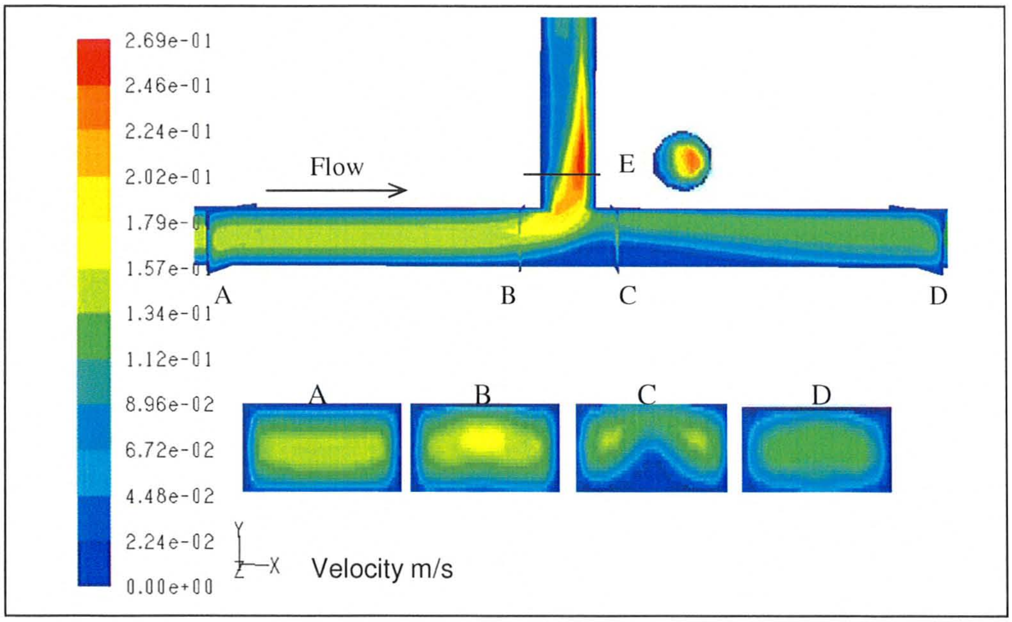

Figure (18): Velocity contours at planes A, B, C, D and E around the first branch (Re=1,217).

Figures (19) to Figure (22) show the velocity vectors around the four branches (in order) for Re=4,629.5.

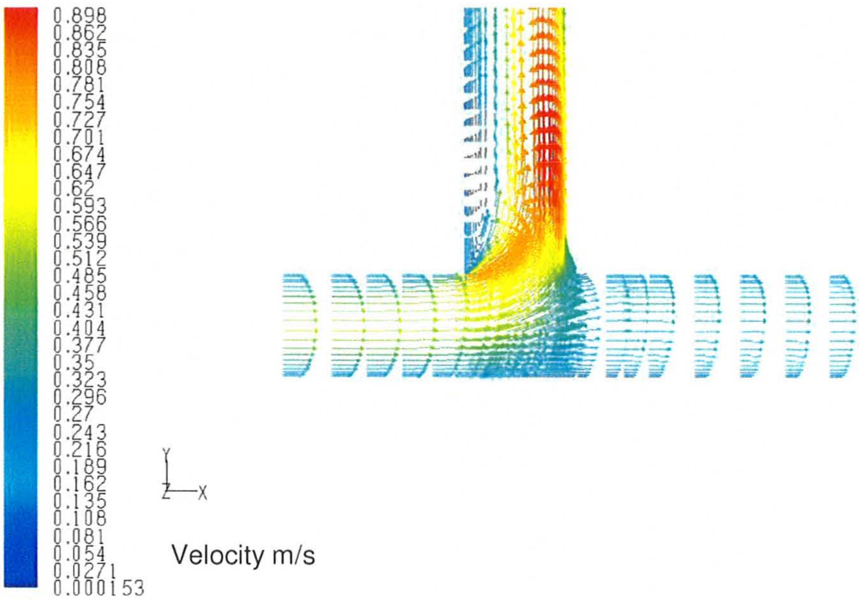

Figure (19): Velocity vectors around branch 1 (Re=4,629.5).

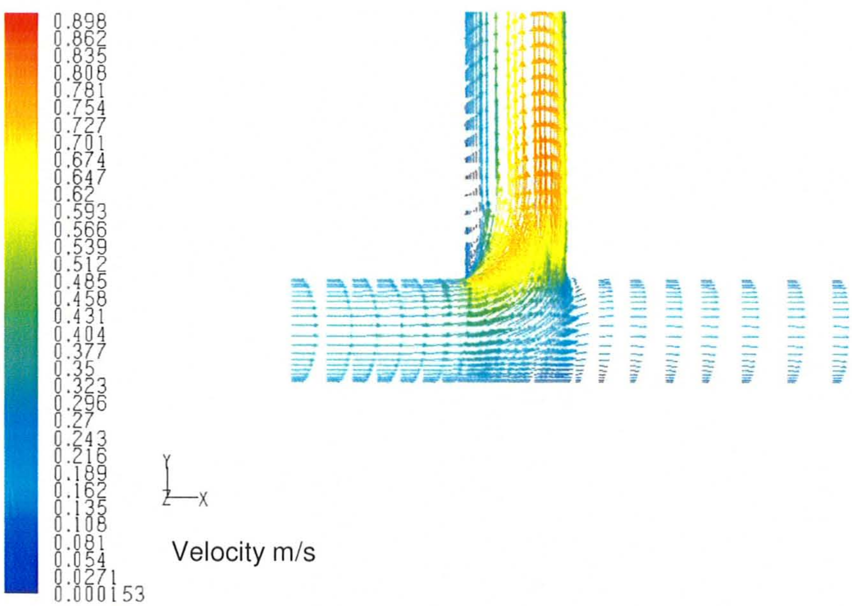

Figure (20): Velocity vectors around branch 2 (Re=4,629.5).

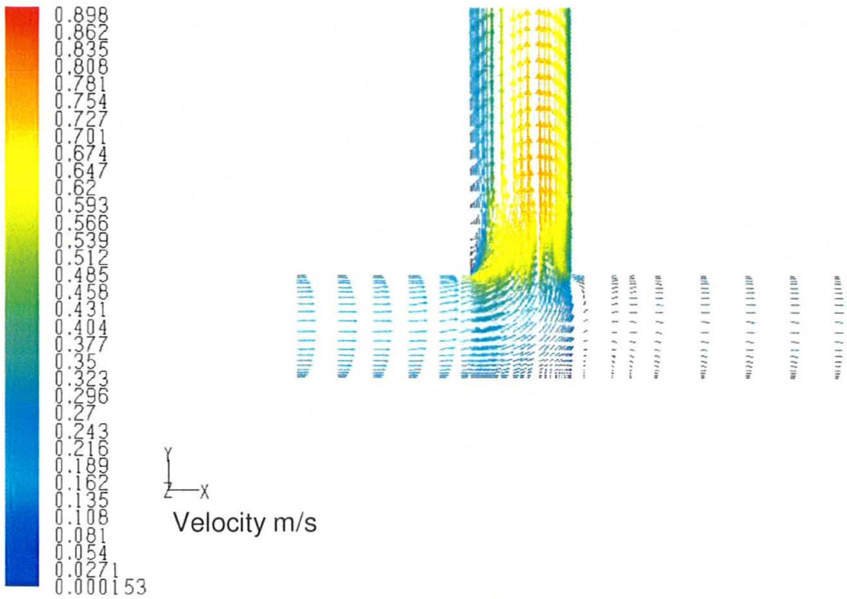

Figure (21): Velocity vectors around branch 3 (Re=4,629.5).

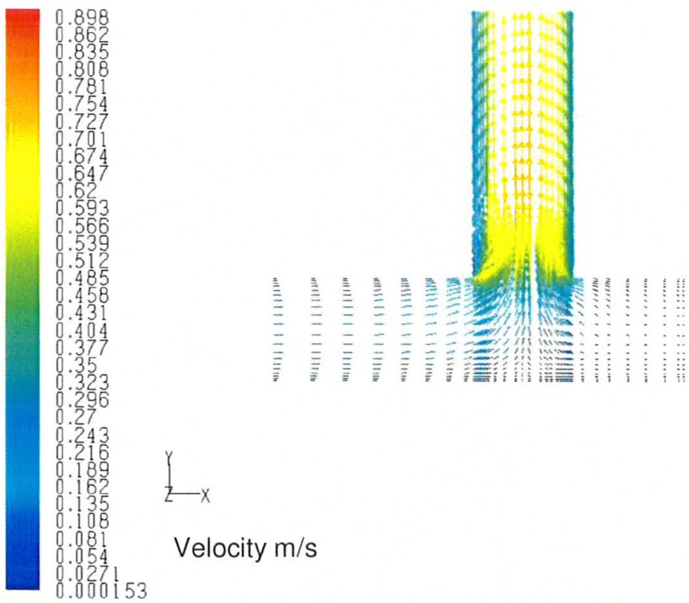

Figure (22): Velocity vectors around branch 4 (Re=4,629.5).

5.1.5 Pressure Gradients

Horiki *et. al.* [11] used the experimentally obtained data of flow distribution in the branches to calculate the pressure gradient in the header. Using the measured flow rates, flow velocities v_m and v_{m+1} at points m and $m+1$ before and after branch m as shown in Figure [23] were calculated. The pressure gradient was then calculated by accounting for pressure loss due to friction and pressure loss due to flow branching.

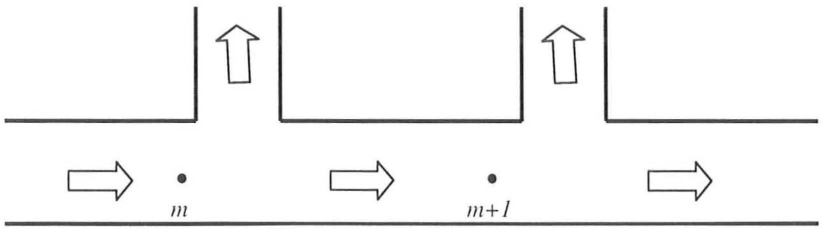

Figure (23): Notation for calculation procedure in Horiki [11].

The obtained results were compared to FLUENT predictions as shown in Figure (24) where good agreement is noticed with a small over-prediction of $P_{3\text{-}4}$. Horiki model provided pressure gradients comparable to those found by FLUENT. This might be due to the fact that these gradients were calculated (in their model) from the experimentally measured flow distribution in the branches. The pressure differences are low for low Re numbers and high for higher Re numbers. This may be due to the increased amount of flow separation and vortex formation near the entrances of the branches as Re number increases.

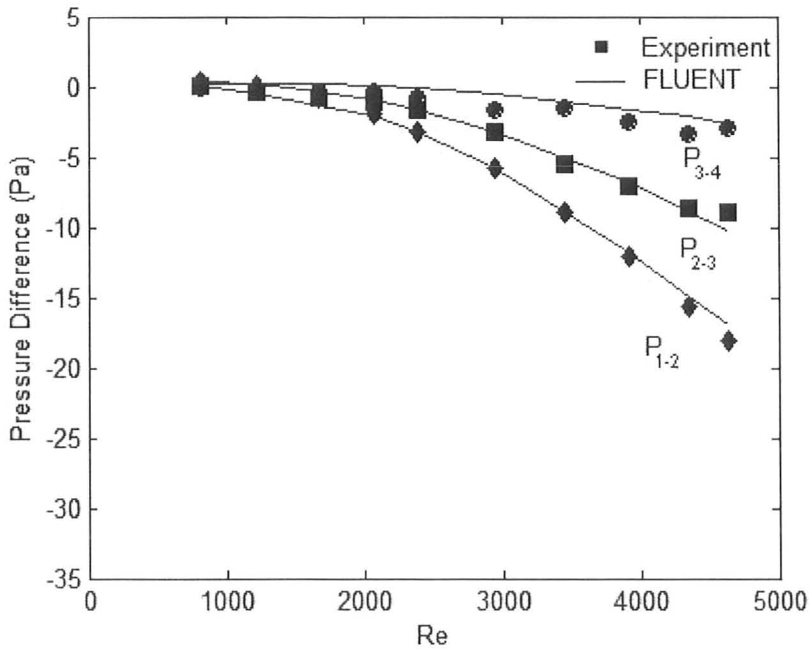

Figure (24): Effect of inlet flow rate on the pressure gradients along the header.

Contours of the dynamic pressure (Pa) at five different planes around each branch for Re=1,217 are shown in Figure (25). Plane A shows a developed pressure where the maximum pressure is at the center point of the duct. This behaviour continues till the pressure starts to increase near the upper wall just before the branch as shown at plane B. At plane C, just after the branch, the pressure is disturbed as a result of flow separation to the branch. As a result of flow separation, the pressure increases through the branch and is maximum at the right wall where the flow "hits" the branch as it separates. (plane E ; just after the branch inlet). The pressure returns developed downwards the header as shown at plane D.

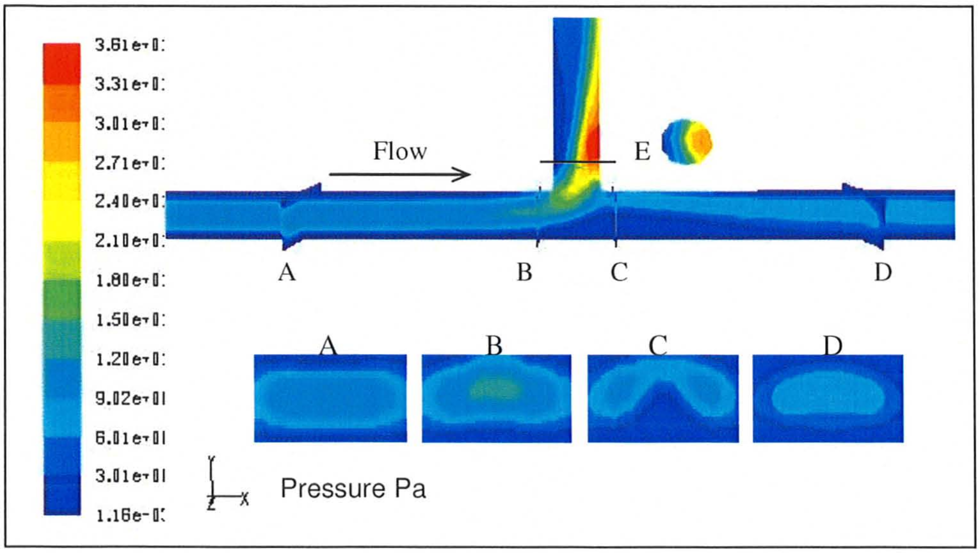

Figure (25): Contours of dynamic pressure at planes A, B, C, D and E around the first branch (Re=1,217).

Figures (26) to Figure (29) show the contours of dynamic pressure around the four branches (in order) for Re=4,629.5.

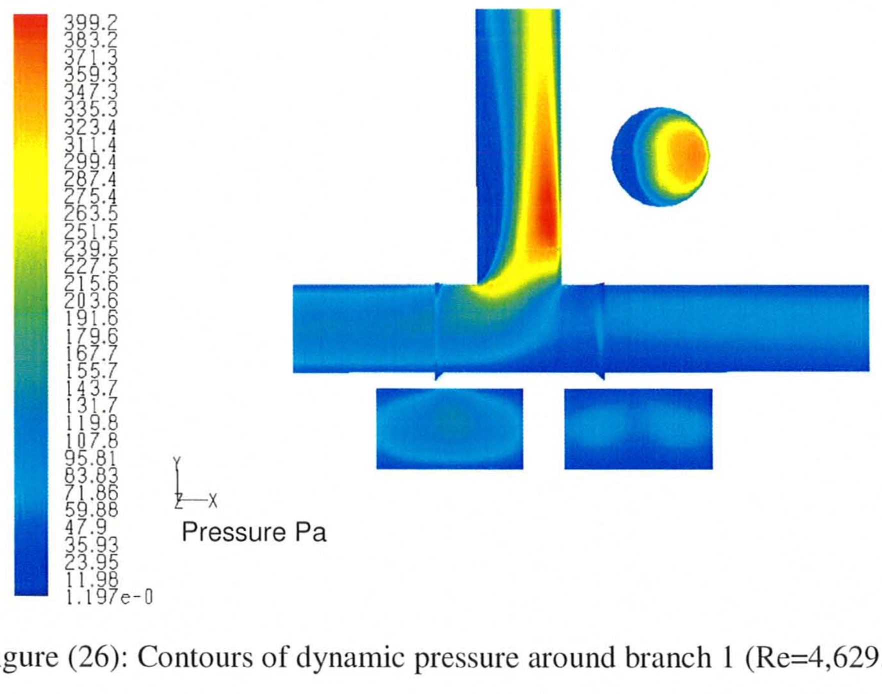

Figure (26): Contours of dynamic pressure around branch 1 (Re=4,629.5).

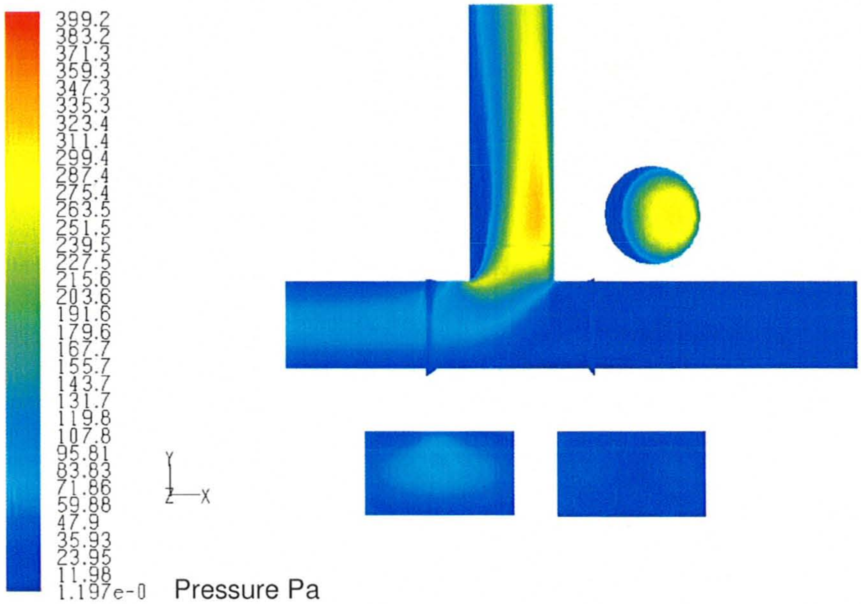

Figure (27): Contours of dynamic pressure around branch 2 (Re=4,629.5).

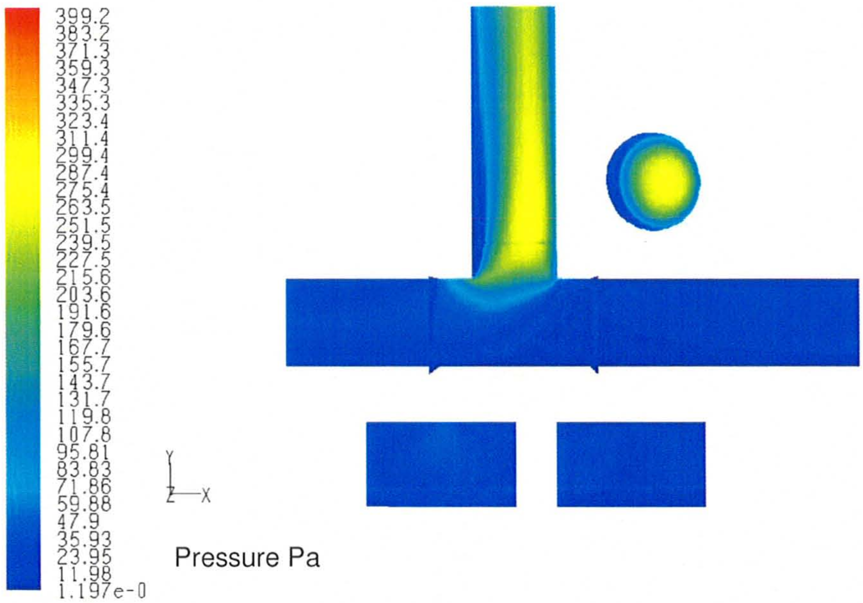

Figure (28): Contours of dynamic pressure around branch 3 (Re=4,629.5).

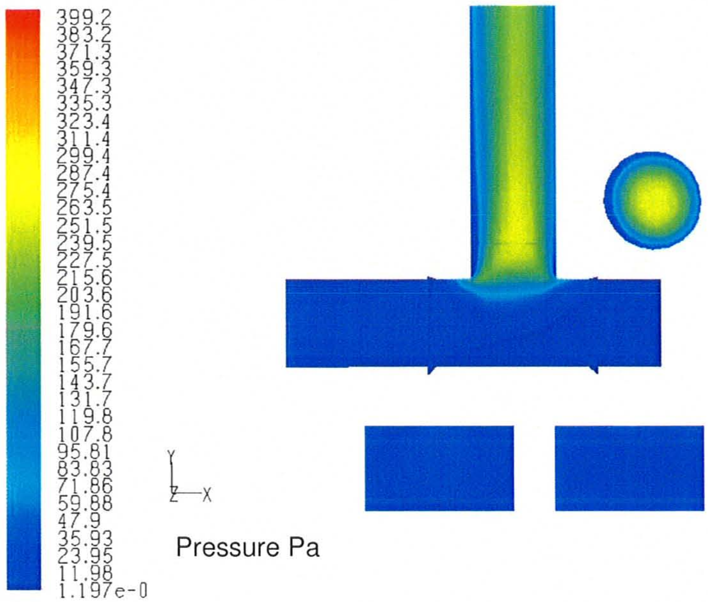

Figure (29): Contours of dynamic pressure around branch 4 (Re=4,629.5).

5.1.6 Flow Separation and Vortex Formation

At Re=5,000, vortex formation inside the header were experimentally observed. The largest vortex was found to occur at the inlet side branch pipe. The observed vortex shape at the inlet of branch 1 is shown in Figure (30) as well as that predicted one by FLUENT (Re number = 5,000). As to the experiment, the vortex predicted by FLUENT has a very similar shape.

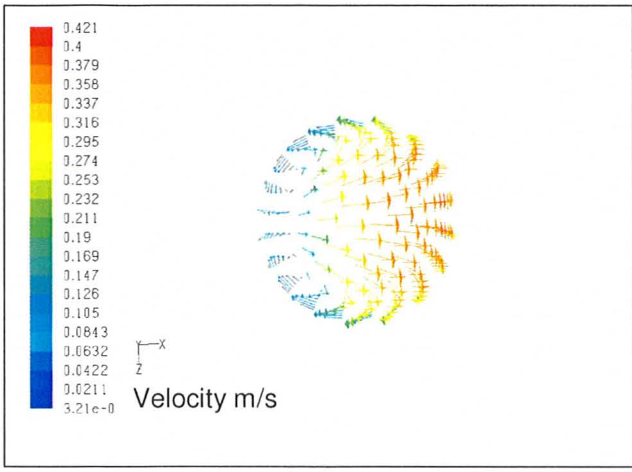

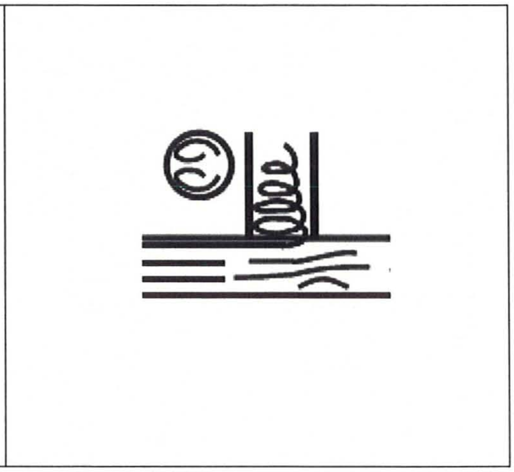

FLUENT prediction Horiki observation [11]

Figure (30): Velocity vectors showing the vorticity at a cross section of the inlet of branch 1 (Re=5,000).

5.1.7 Header Size

Figure (31) shows the effect of the header size on the flow distribution. The flow distribution in the 10 mm × 40 mm header was experimentally measured but the distribution in the 40 mmx 40 mm header was theoretically calculated by a 1-dimentional model. FLUENT provided good prediction of the experimental data of the 10 mmx 40 mm header. For the 40 mmx 40 mm header, FLUENT over-predicted Horiki calculations in the first branch and under-predicted it in the last two branches. This may be due to the three dimensional effects of the flow.

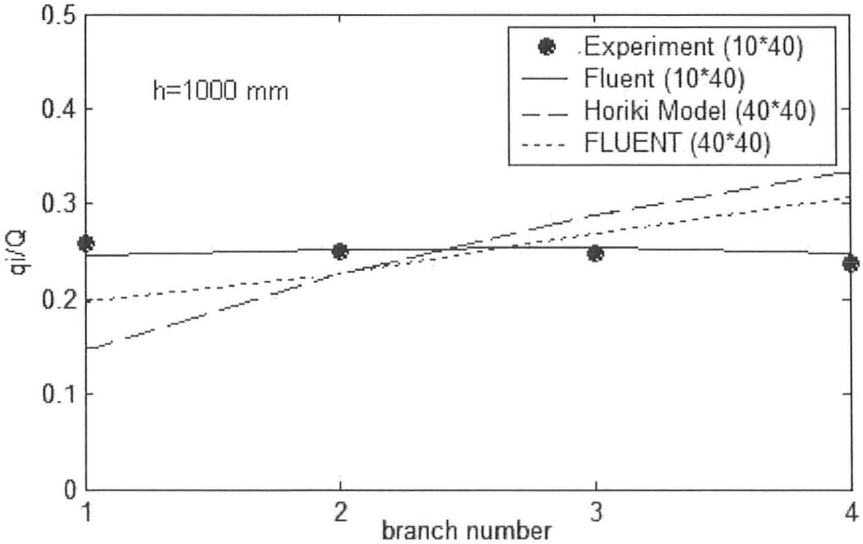

Figure (31): Effect of header size on flow distribution (Re=4,000) where h is the outlet branch length.

5.1.8 Conclusions of First Validation

CFD prediction of flow and pressure distributions in the multi-branch rectangular flow header using FLUENT (6.24361×10^5 nodes) provided good agreement with experimental data under a range of inlet Re number (817.3 – 4,629.5). Standard k-ε turbulence model with enhanced wall treatment was found to provide best fit of the data.

5.2 Vertical-Inlet Header Configuration

5.2.1 Geometry and Mesh Generation

As the mesh quality is very important for the CFD analysis, this section describes in details how the mesh was generated especially in the region where one inlet and two outlet branches connected to the header. The steps followed are summarized in Figure (32). A sample of the entire geometry meshed is shown in Figure (33).

Several grid densities (6.08941×10^5, 2.531985×10^6 and 3.949979×10^6 nodes) were investigated to study the effect of grid density on the solution (Section 5.2.2). Maximum value of cell skewness coefficient is 0.8 which is the limit recommended by FLUENT.

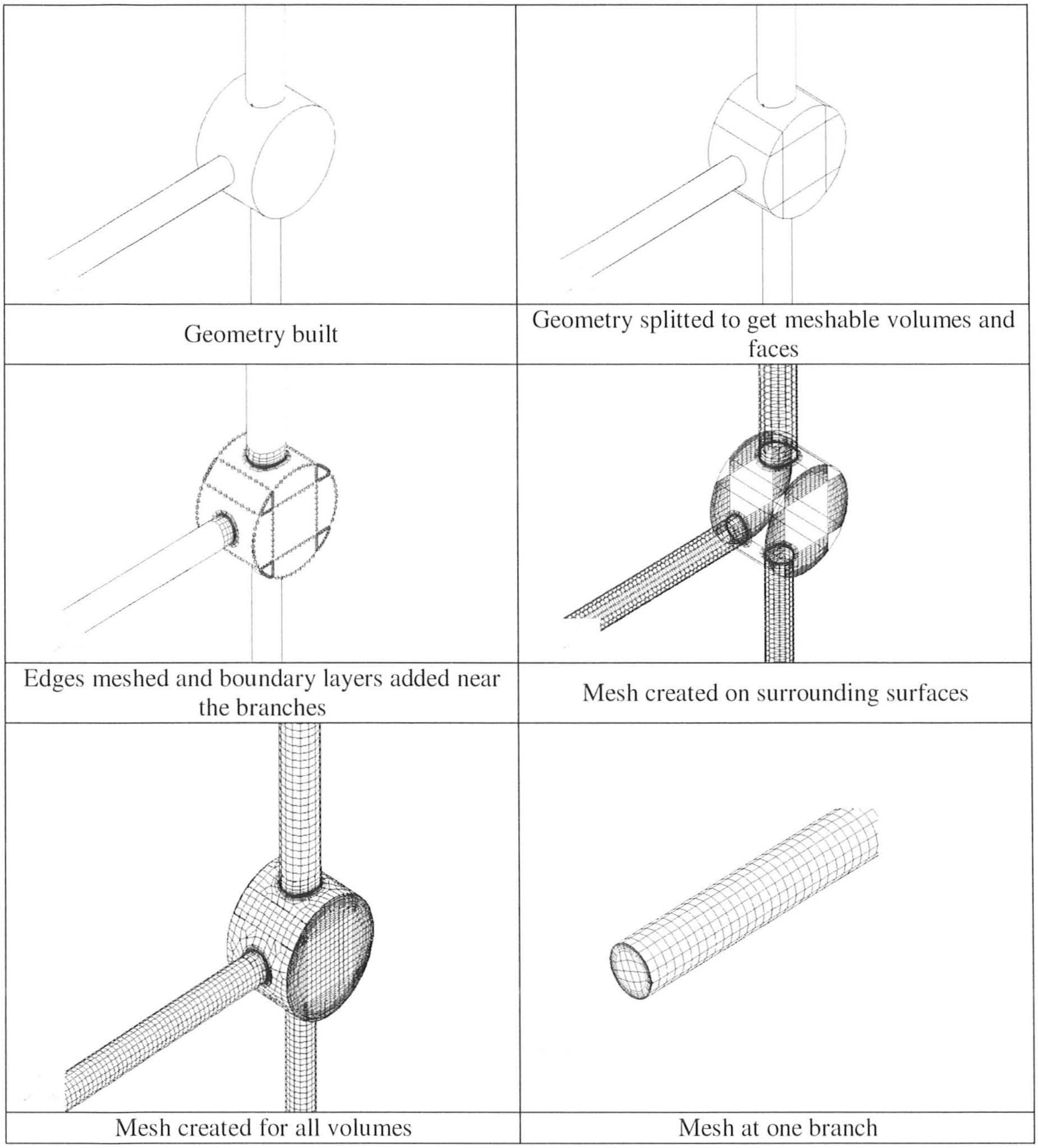

Figure (32): Steps followed to create the mesh at the junction region between the header and three branches (one inlet and two outlets).

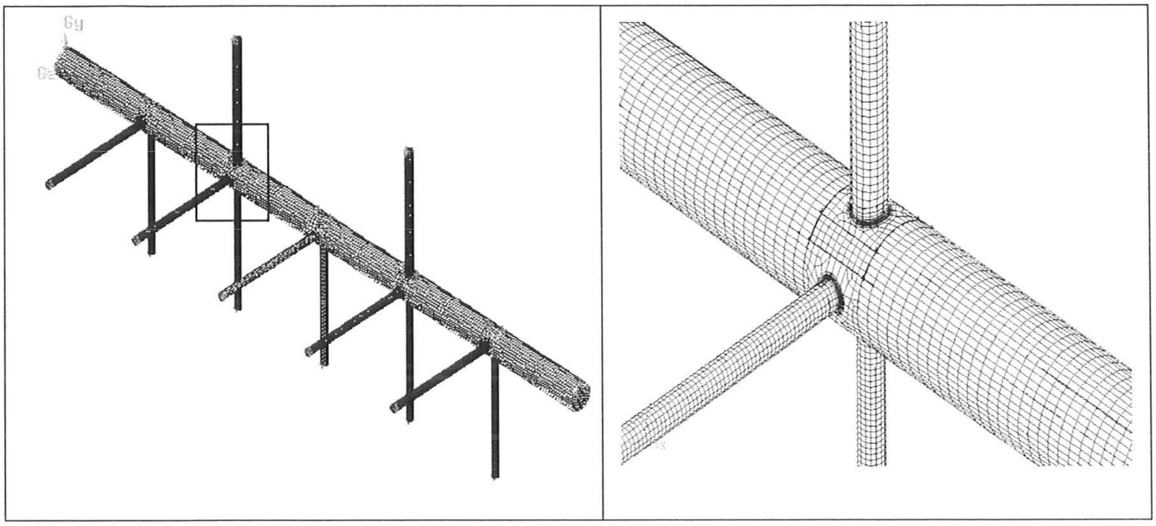

Figure (33): Sample of mesh consisting of 1.013489×10^{6} nodes.

The Y^{+} plot of the mesh is shown in Figure (34) for Inlet1=0.310 kg/s and Inlet2=0.307 kg/s. The value is almost < 5 (except at the inlets) which means the near-wall resolution is in the most accurate region to which the boundary layer can be resolved [28]. The anomalies noticed in the figure are usual to occur in FLUENT at the inlets [28] and do not necessarily mean that the mesh is not of high quality at the inlets.

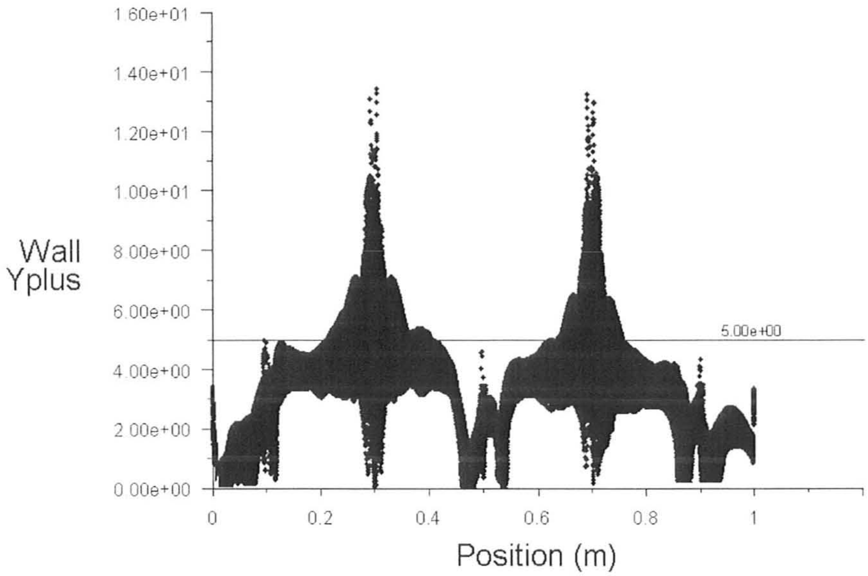

Figure (34): Y^+ value near the wall (Inlet1=0.310 kg/s and Inlet2=0.307 kg/s).

5.2.2 Operating and Boundary Conditions

Table (7) shows the boundary and operating conditions assigned in FLUENT.

Table (7): Boundary and Operating Conditions assigned in FLUENT (vertical- and horizontal-inlet header configurations).

Condition	Value	Unit
Operating fluid	Water	---
Inlet flow rate (range)	0-0.307	kg/s
Level of inlet flow imbalance	$\text{Imbalance} = \dfrac{\text{Inlet 2 flowrate}}{\text{Inlet 1 flowrate}}$	---
Gravity	9.81	m/s^2
Outlet pressure	101325	Pa

5.2.3 Sensitivity Analysis

5.2.3.1 Sensitivity to Grid Density

Similar to the validation discussed in section 5.1.3.1, several grid densities were used to study the effect of grid density on the solution. A mesh of 608 k nodes was initially used. The mesh was then further refined until no significant change in the solution was noticed using two successive grid densities. The grid density beyond which no significant change in the solution noticed was adopted as the reference grid in the rest of this work.

The reference grid consists of 2 M nodes. Figure (35) shows the flow distribution obtained using three grid densities (6.08941×10^5, 2.531985×10^6 and 3.949979×10^6 nodes). Very small difference (less than 1%) in solution is observed when using the reference grid and the finest meshes. The average run time using the finest mesh (with standard k-ε turbulence model) was around 17 hours. With the reference mesh it was around 9 hours using 1.86 GHz processor with convergence criteria of 10^{-5}.

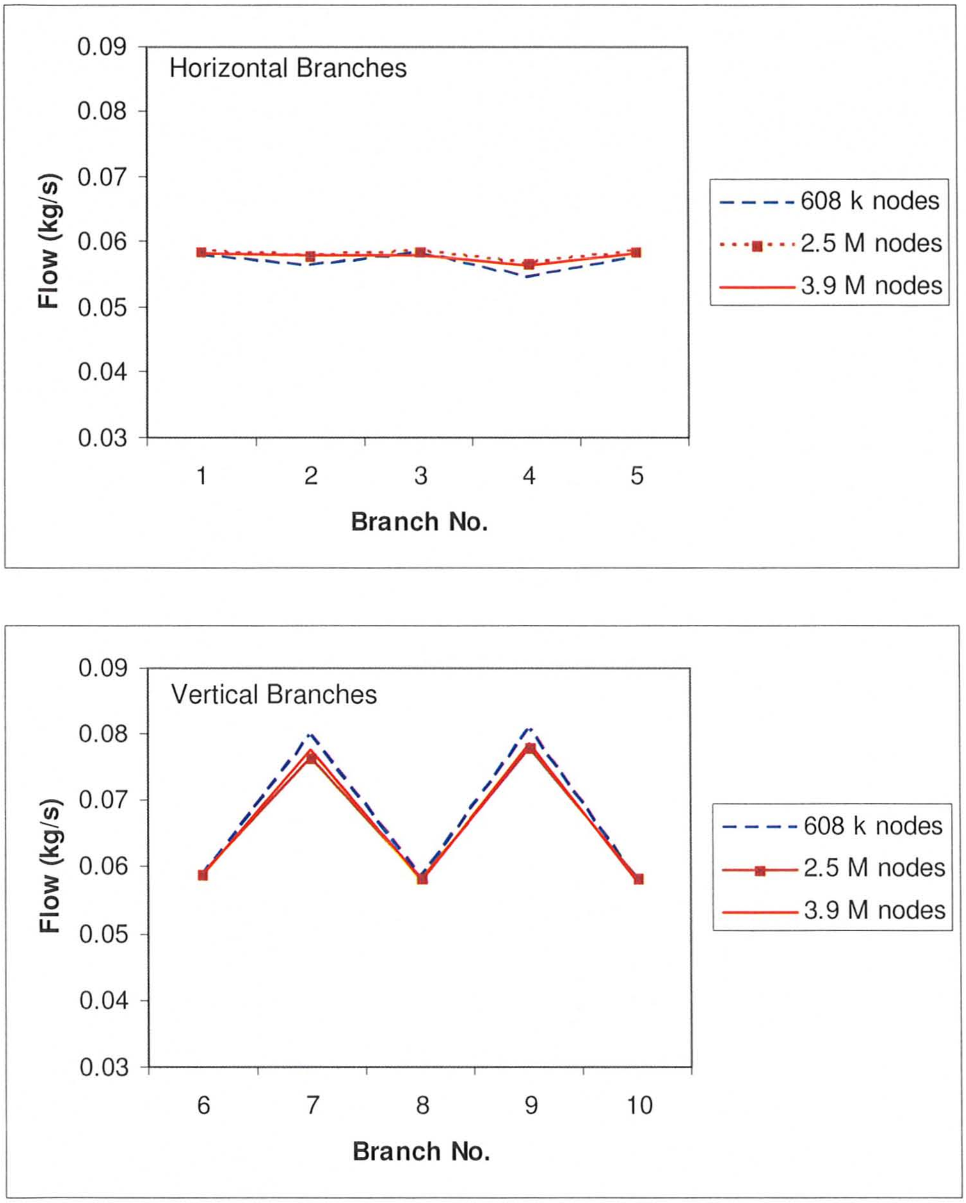

Figure (35): Effect of grid density on flow distribution (Run 1/1).

5.2.3.2 Selection of Turbulence Model

The laminar, Sparlart-Allmaras, k-ε, k-ω, models with standard, non-equilibrium and enhanced wall treatments were investigated and their predictions were compared to experimental data.

Several experimental runs were selected so that they represent various levels of flow imbalance and flow rates for the comparison. These runs are shown in Table (8).

Table (8): Experimental Runs selected to study the sensitivity to turbulence modeling.

Run	**Flow rates (kg/s)/(kg/s)**	**Description**
Run 1/1	0.307/0.307	Imbalance = 1.00, high flow rate/high flow rate.
Run 5/1	0.307/0.000	Imbalance = 0.00, high flow rate/no flow.
Run 2/2	0.232/0.232	Imbalance = 1.00, moderate flow rate/moderate flow rate.
Run 4/2	0.232/0.083	Imbalance = 0.36, moderate flow/very low flow rate.
Run 4/4	0.083/0.083	Imbalance= 1.00, very low flow rate/very low flow rate.

For the selected runs, the RNG k-ε model with enhanced wall treatment and the k-ω models were found to provide the best fit of the data (most predictions are within the measurement error bar). A comparison between three selected models (the standard and RNG k- ε and the standard k-ω models) is shown in Figure (36) and Figure (37) for several runs. Plots of prediction error for several runs are shown in Figures (38) to Figure (40) where the sum of prediction errors for the ten branches are plotted for each combination of turbulence model/wall treatment tested. The RNG model was selected for the rest of this work as it is more commonly used for wide applications in literature.

However, to reduce the simulation time for many reference cases, the solution is initiated from an initial guess generated from the standard k-ε turbulence model with standard wall treatment [10].

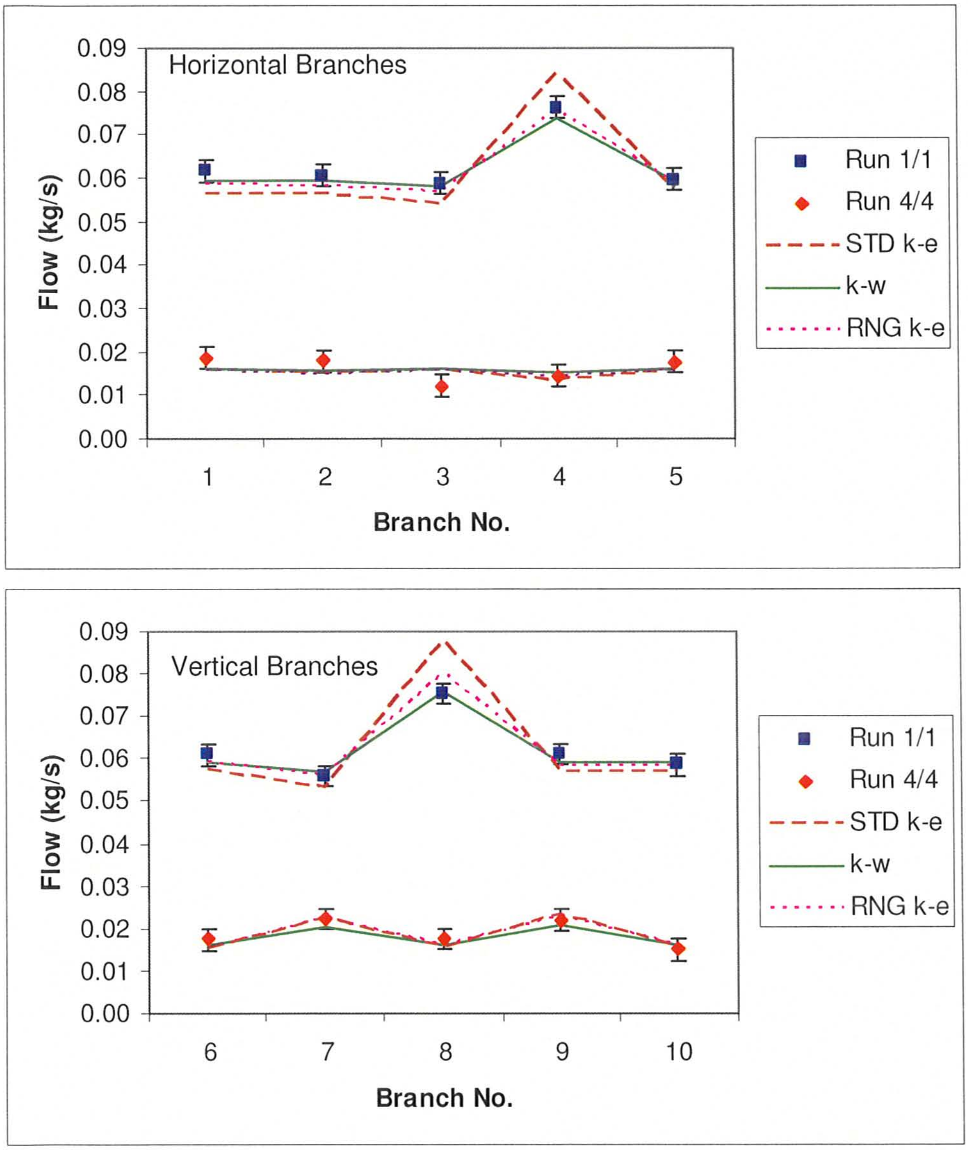

Figure (36): Sensitivity to turbulence modeling (Run 1/1 and Run 4/4).

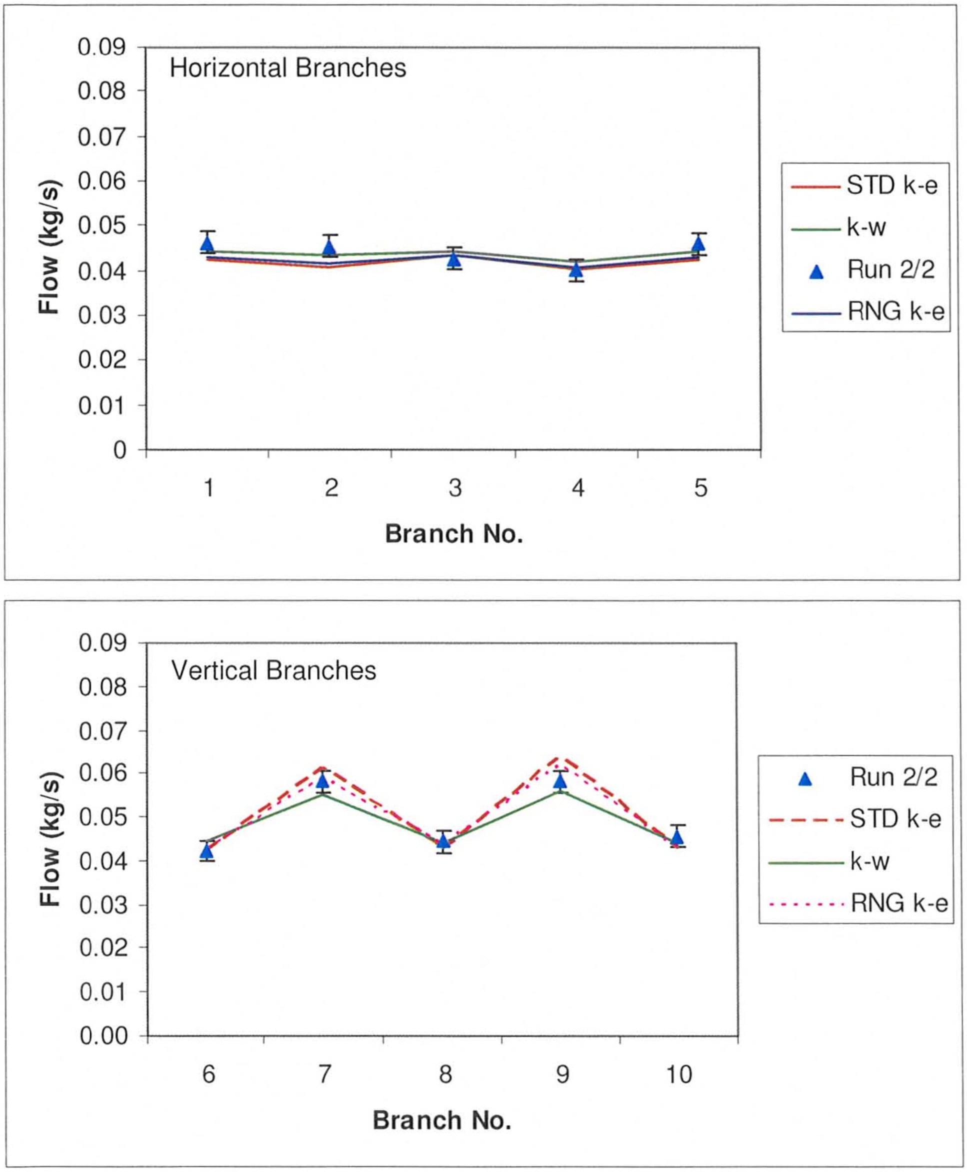

Figure (37): Sensitivity to turbulence modeling (Run 2/2).

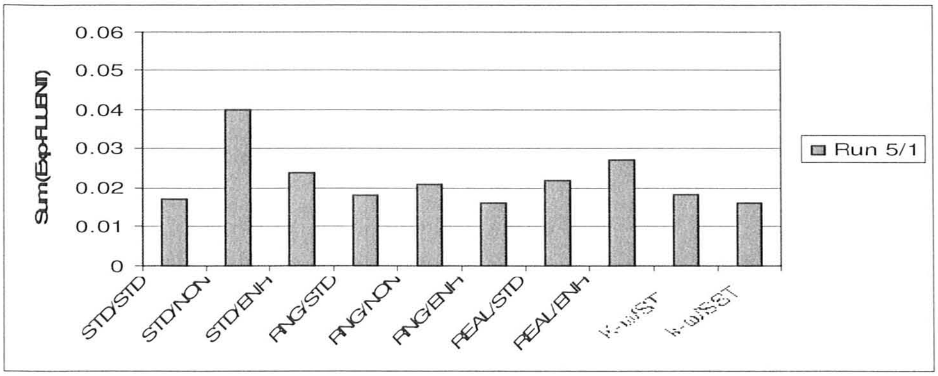

Figure (38): Summation of prediction errors for each combination of turbulence model/wall treatment for Run 5/1 (0.307/0.000 (kg/s)/(kg/s)).

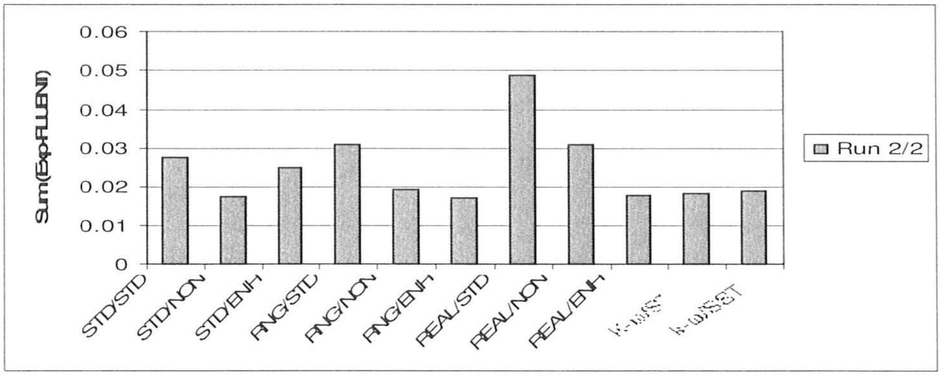

Figure (39): Summation of prediction errors for each combination of turbulence model/wall treatment for Run 2/2 (0.2328/0.232 (kg/s)/(kg/s)).

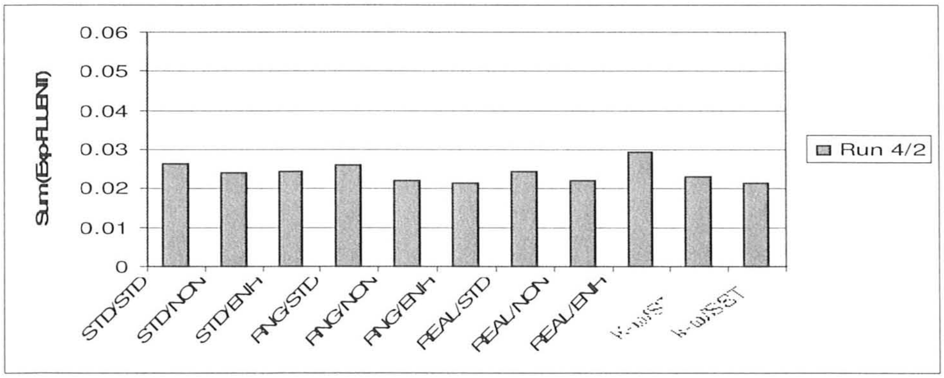

Figure (40): Summation of prediction errors for each combination of turbulence model/wall treatment for Run 4/2 (0.232/0.083 (kg/s)/(kg/s)).

5.2.3.3 Convergence Criteria

Sensitivity analysis of flow distribution to convergence criteria has been conducted. The tolerance was initially set to FLUENT default's value (10^{-3}) and then decreased. No significant change in solution (less than 0.2 %) was noticed when it was decreased from 10^{-5} to 10^{-6} and thus the tolerance was set to 10^{-5} in the rest of this validation work. The results are shown in Figure (41) for Run 1/1.

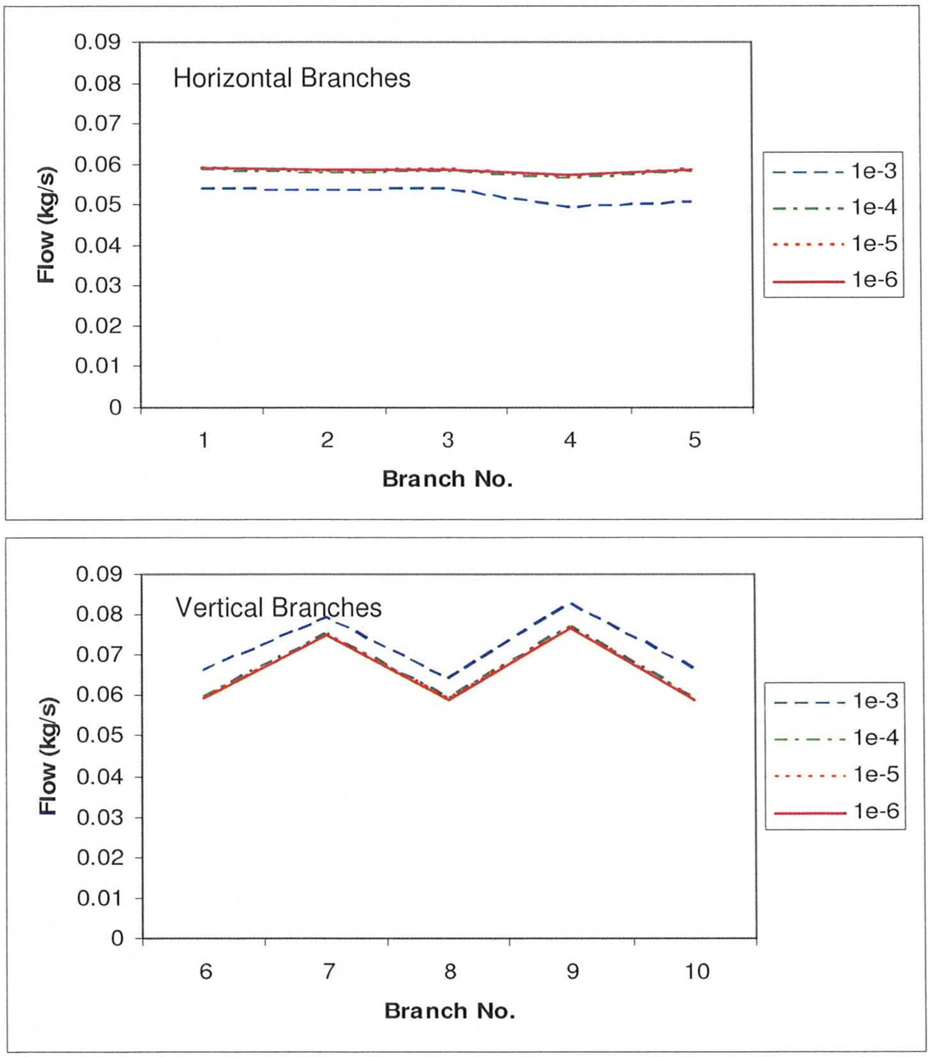

Figure (41): Sensitivity of flow distribution to convergence criteria (Run 1/1).

5.2.4 Flow Prediction Results

The measured outlet flow rates for all runs were compared to FLUENT predictions. Figure (42) shows the comparison for the full balanced flows (Run1/1, Run 2/2, Run3/3 and Run 4/4 described in Table (3)). Good agreement is noticed for all reference cases. From the figure, it is noticed that most predictions are within the accuracy of the outlet flowmeters (±0.0025 kg/s).

By comparing the plot of flow in the horizontal outlets (branch No. 1-5) and the vertical outlets (branch No.6-10), better agreement is noticed for the vertical outlets. Figure (42) also shows that the error between the computations and measurements increases with decreasing flow rate. For very low flow rates the influence of the physical exit conditions for each branch was excessive. Therefore the very low flow rates are not included in the accuracy assessment.

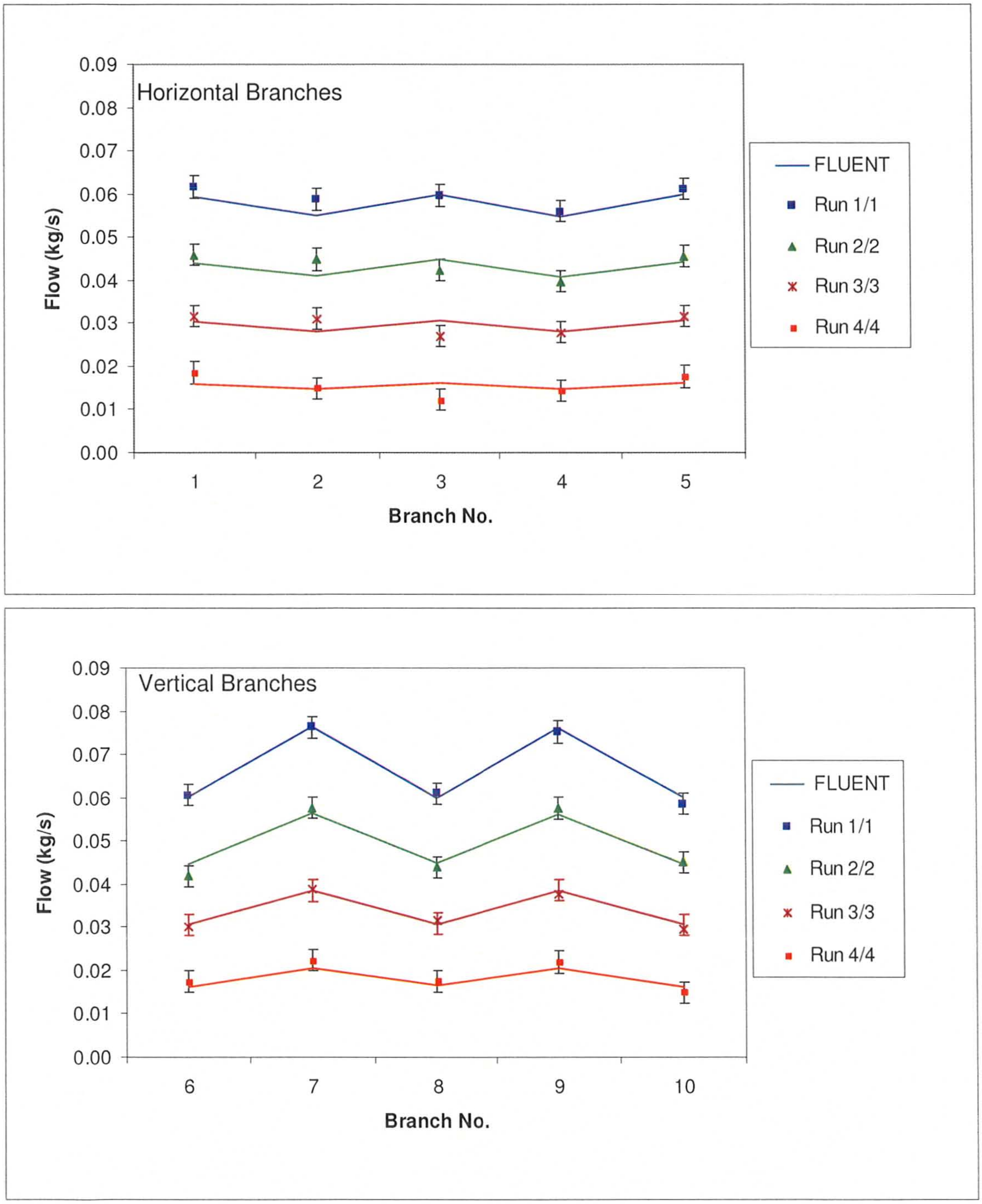

Figure (42): Experimental data and FLUENT predictions for full balanced flows (Run1/1, Run 2/2, Run3/3 and Run 4/4 described in Table (3)).

5.2.5 Effect of Inlet Flow Imbalance

The measured outlet flow rates for all runs with imbalanced flow were compared to FLUENT predictions. Figure (43) to Figure (47) show the comparison where good agreement is noticed.

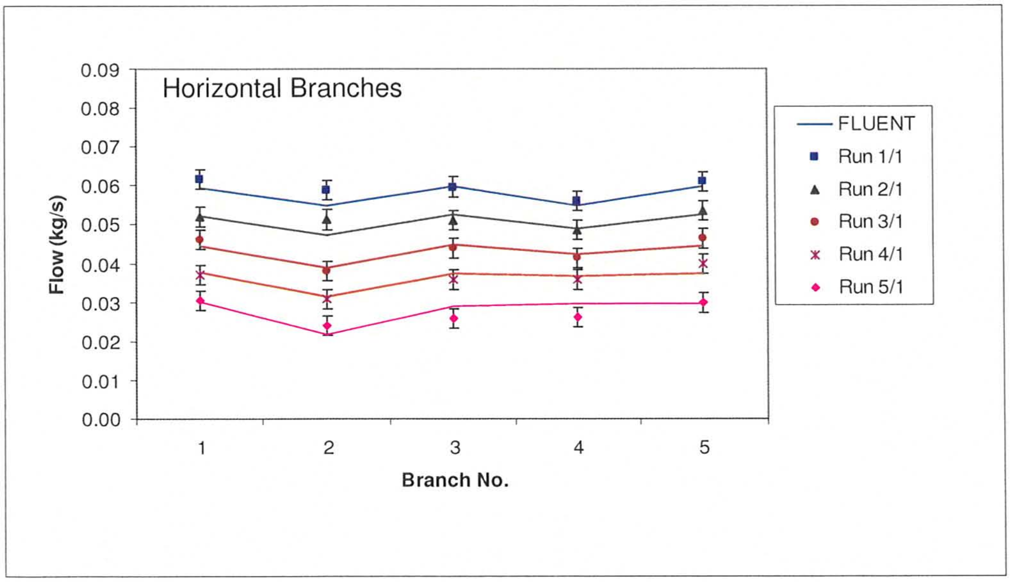

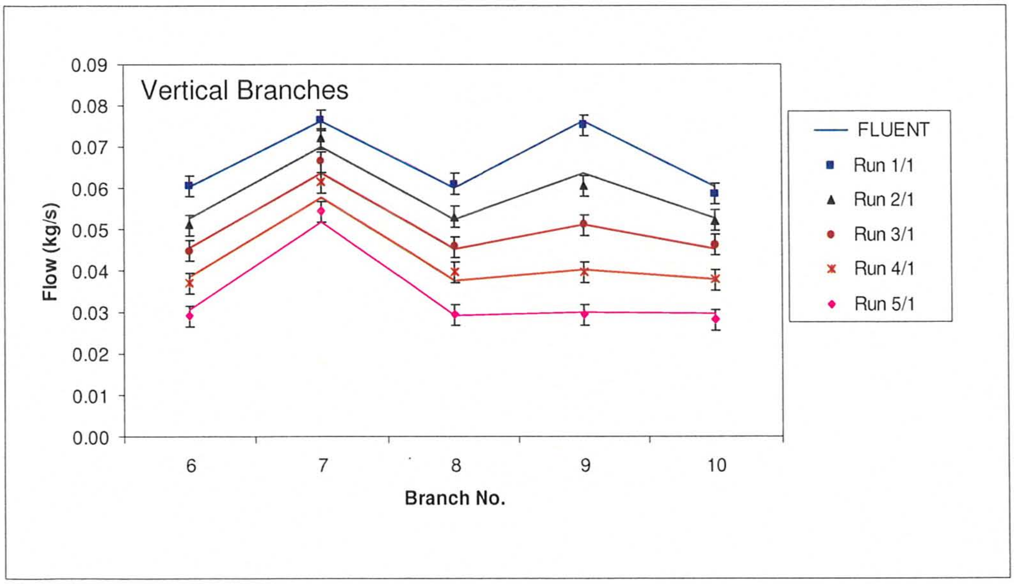

Figure (43): Experimental data and FLUENT predictions of flow distribution in the branches (Run1/1, Run 2/1, Run 3/1, Run 4/1 and Run 5/1 described in Table (3)).

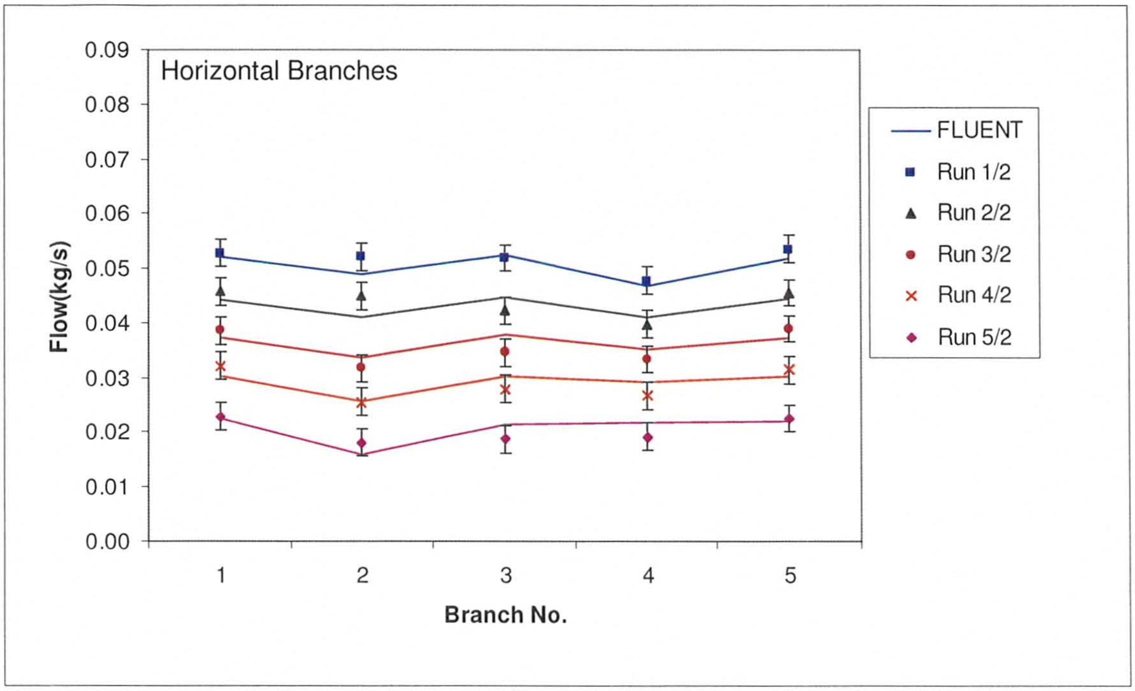

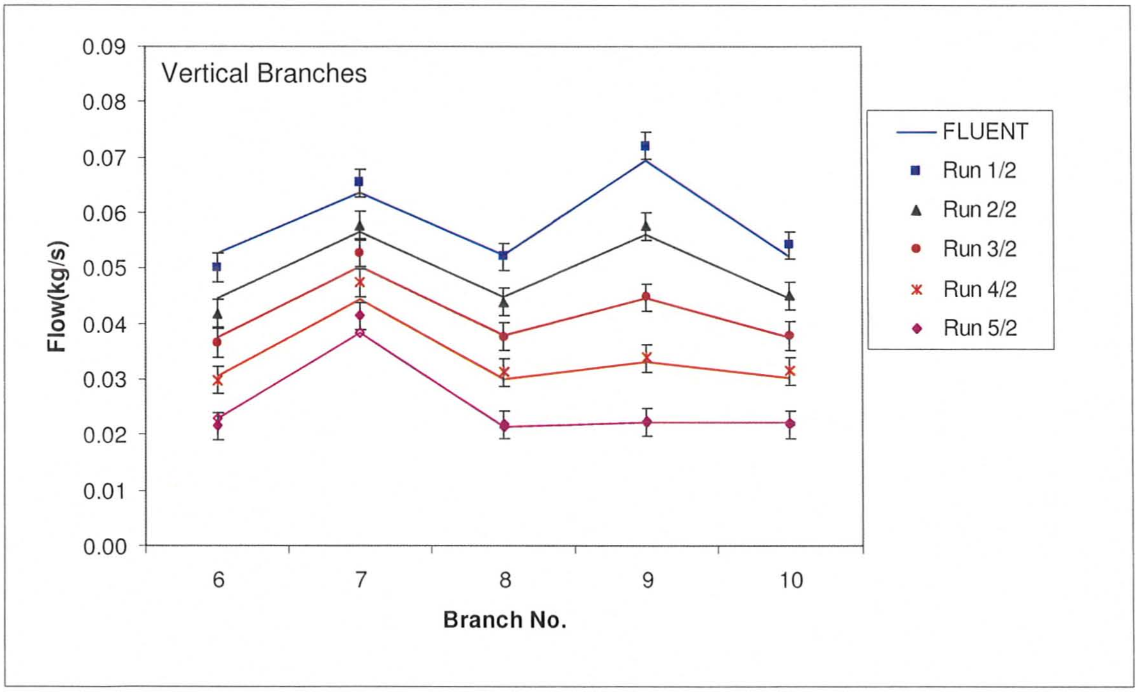

Figure (44): Experimental data and FLUENT predictions of flow distribution in the branches (Run1/2, Run 2/2, Run 3/2, Run 4/2 and Run 5/2 described in Table (3)).

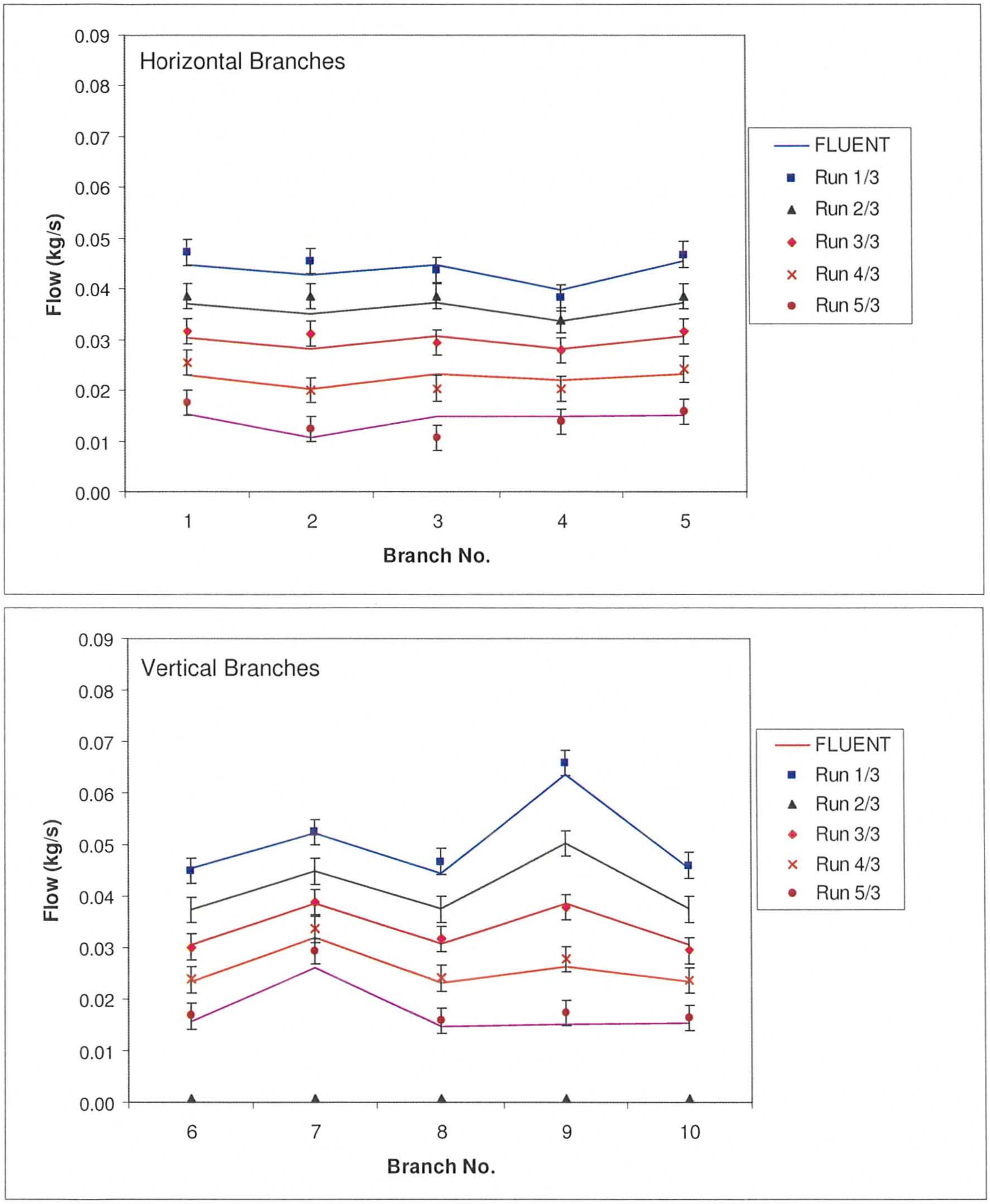

Figure (45): Experimental data and FLUENT predictions of flow distribution in the branches (Run1/3, Run 2/3, Run 3/3, Run 4/3 and Run 5/3 described in Table (3)).

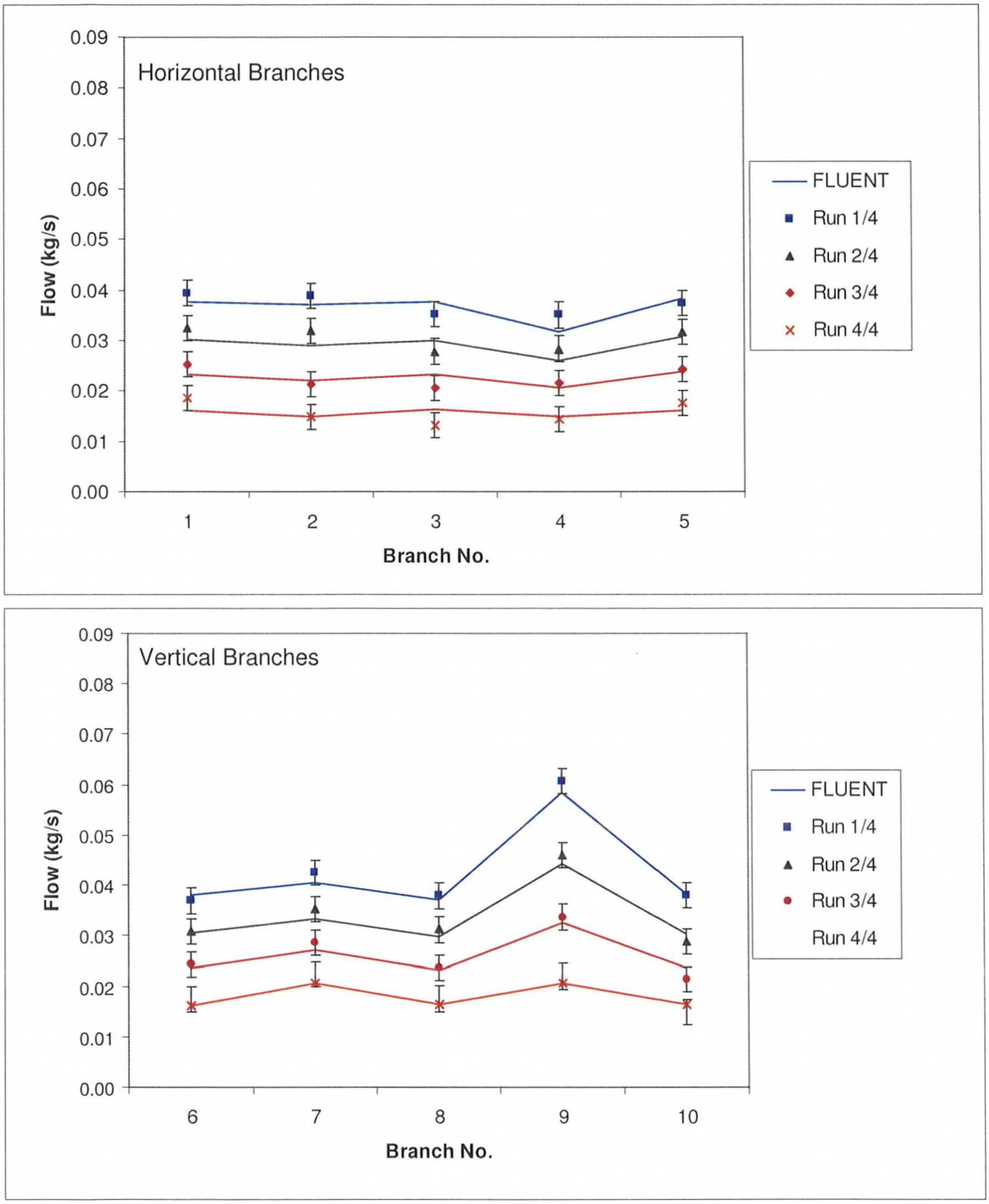

Figure (46): Experimental data and FLUENT predictions of flow distribution in the branches (Run1/4, Run 2/4, Run 3/4 and Run 4/4 described in Table (3)).

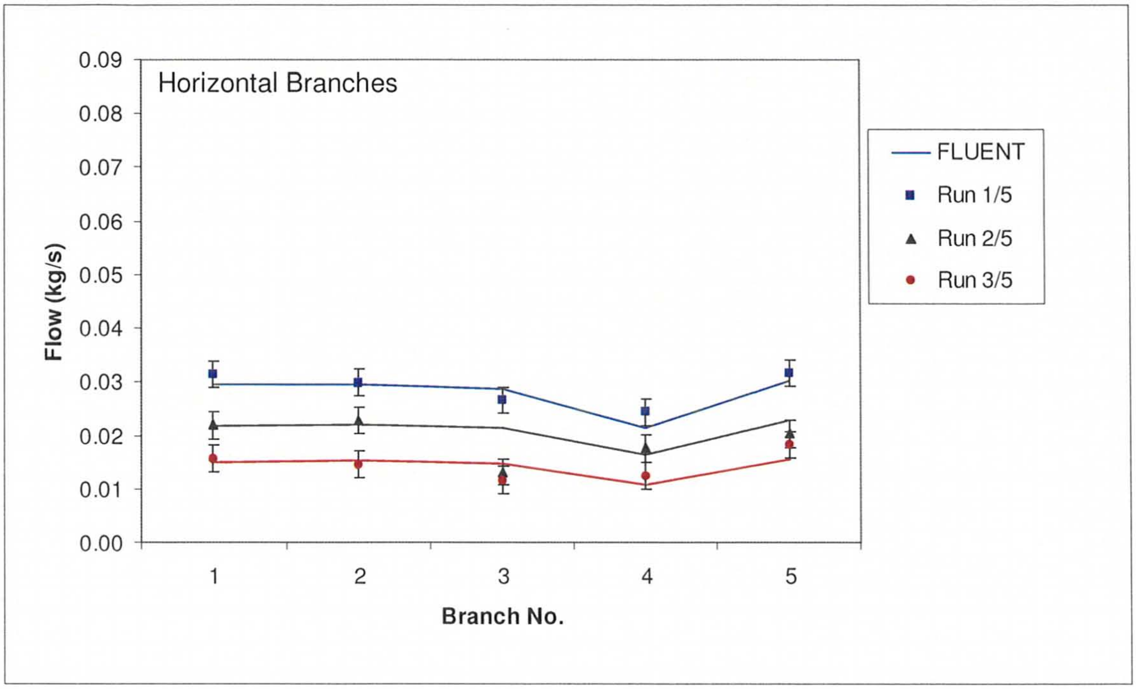

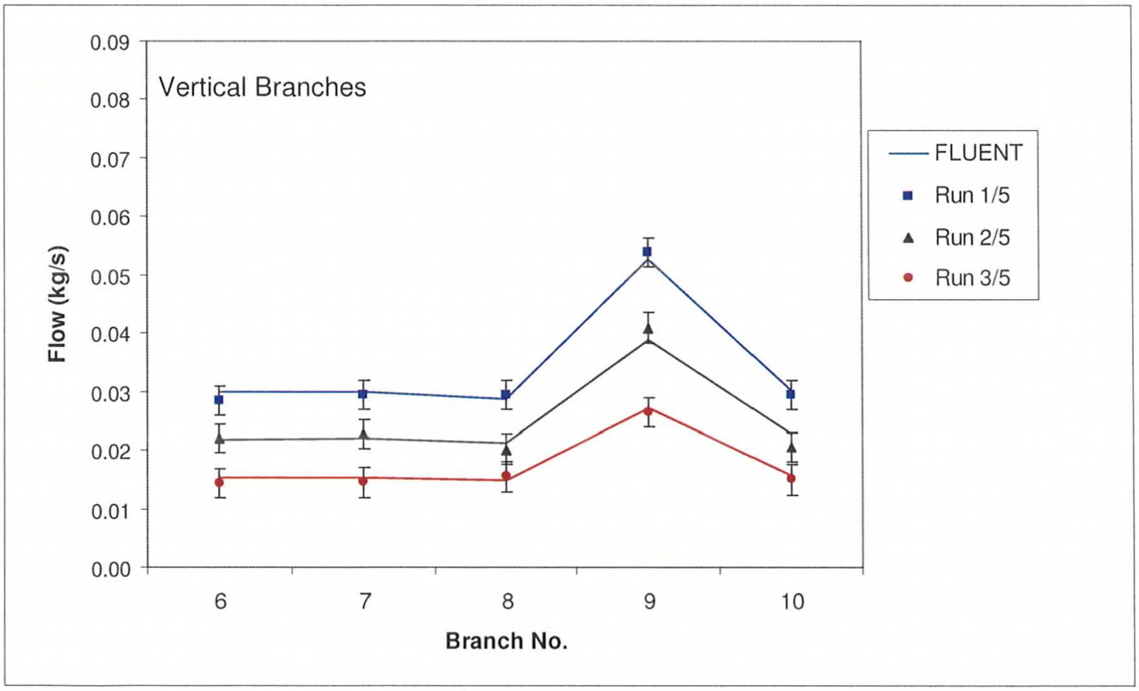

Figure (47): Experimental data and FLUENT predictions of flow distribution in the branches (Run1/5, Run 2/5 and Run 3/5 described in Table (3)).

The relative errors of flow prediction are plotted versus the inlet flow level of imbalance in Figure (48) to Figure (51). The upper dotted line was drawn by connecting the point representing the larger positive error at the lowest imbalance with that at the highest imbalance. The lower dotted line was drawn the same way but for the negative error points. These lines represent the upper and lower error bounds. The figures show that the error is almost independent on the level of imbalance. Also, it is noticed that the relative error increases by decreasing inlet flow rate (by going from Figure (48) to Figure (51)). The relatively higher error at the lower flow rates is due to the difficulty in measuring the low flow rates.

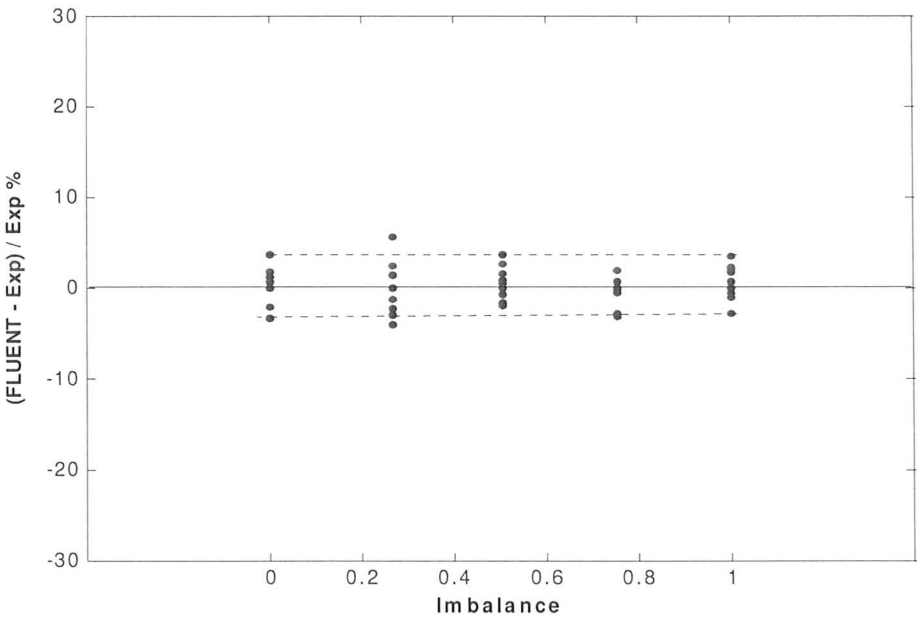

Figure (48): Error in flow prediction versus imbalance level (Inlet 1 kept constant at 0.307 kg/s).

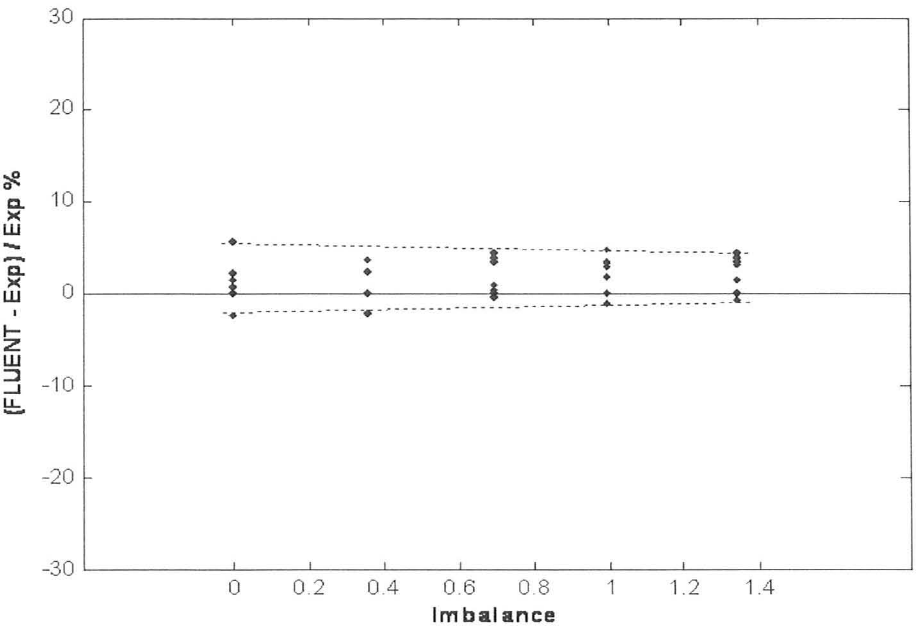

Figure (49): Error in flow prediction versus imbalance level (Inlet 1 kept constant at 0.232 kg/s).

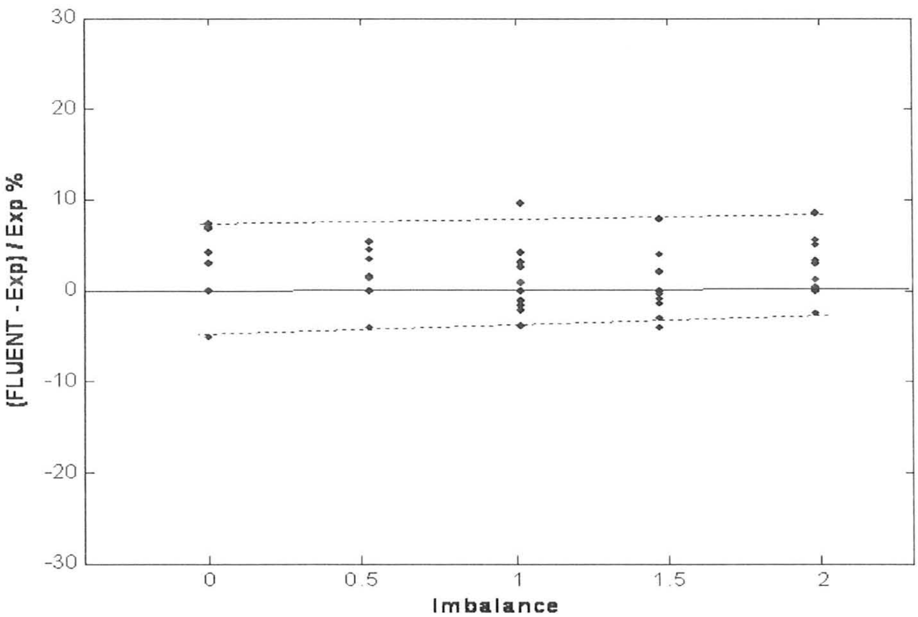

Figure (50): Error in flow prediction versus imbalance level (Inlet 1 kept constant at 0.158 kg/s).

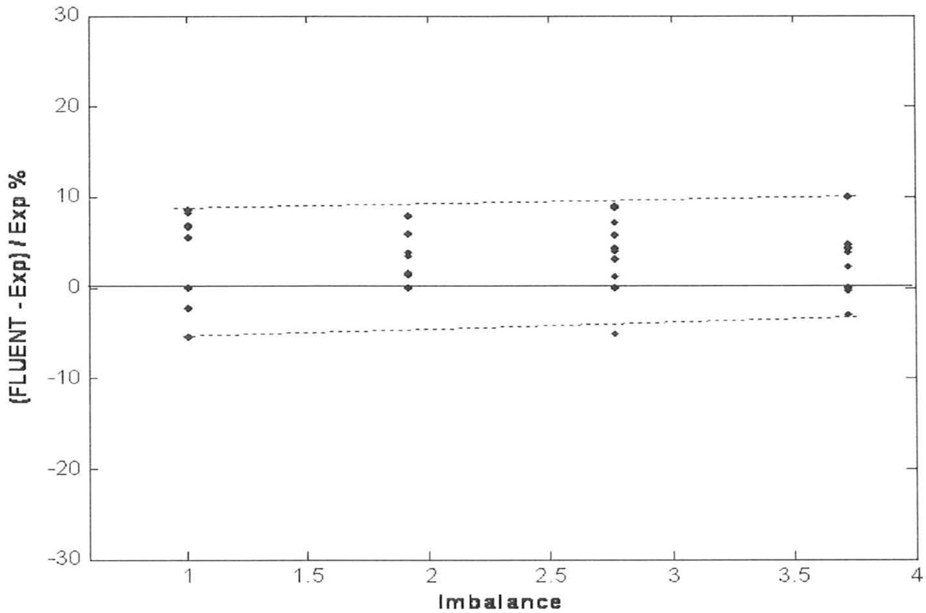

Figure (51): Error in flow prediction versus imbalance level (Inlet 1 kept constant at 0.083 kg/s).

5.2.6 Velocity and Pressure Contours/Vectors

The velocity contours along the header are shown in Figure (52) for a balanced flow case (i.e., Inlet1 = Inlet2 = 0.307 kg/s). More flow goes to the vertical outlet as it is just beneath the headers inlet. Velocity vectors around Inlet1 in cross sectional and axial views are shown in Figure (53) and Figure (54); respectively. The figures clearly show the vortices formed in the azimuthal and axial directions along the header. Pressure contours around Inlet1 in the axial direction are shown in Figure (55).

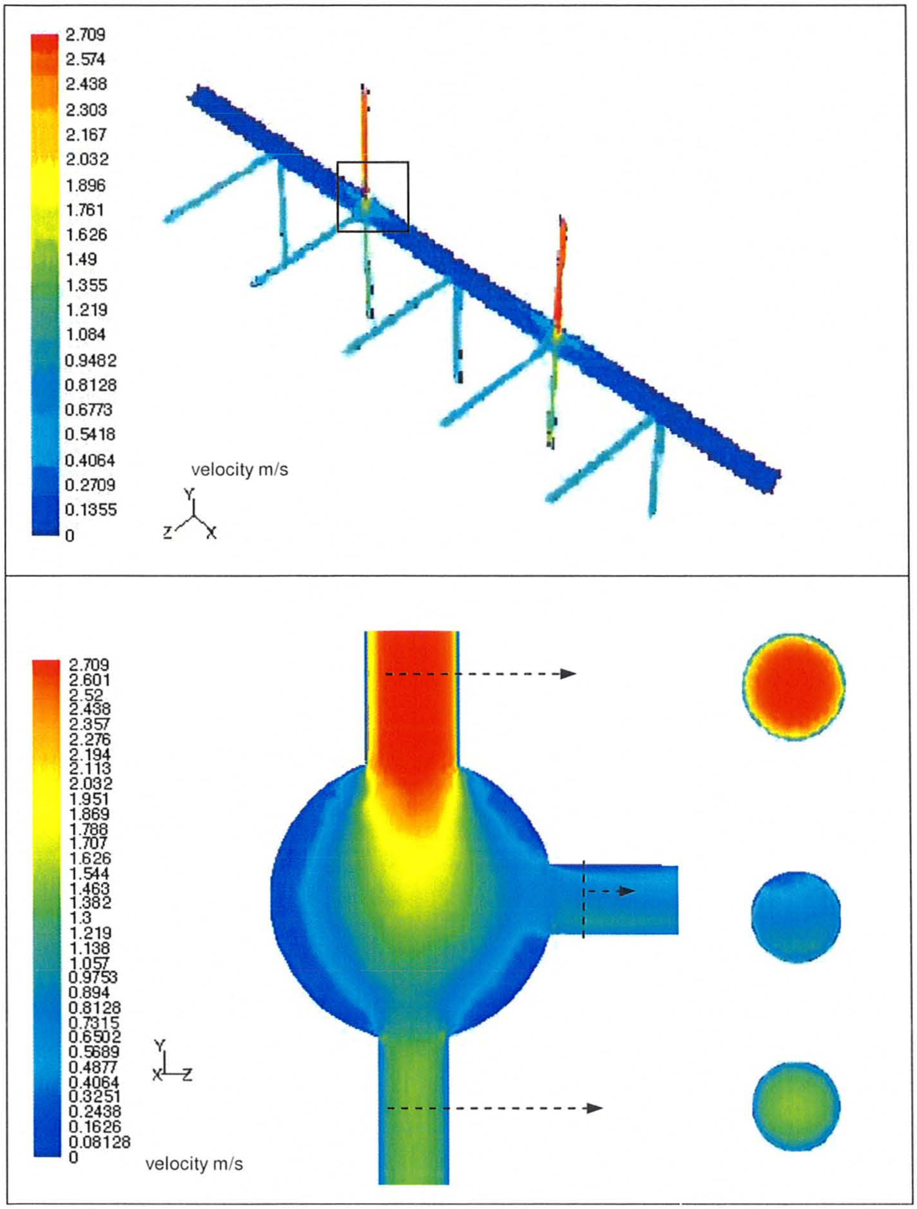

Figure (52): Velocity contours (m/s) along the header (Inlet1 = Inlet2 = 0.307 kg/s).

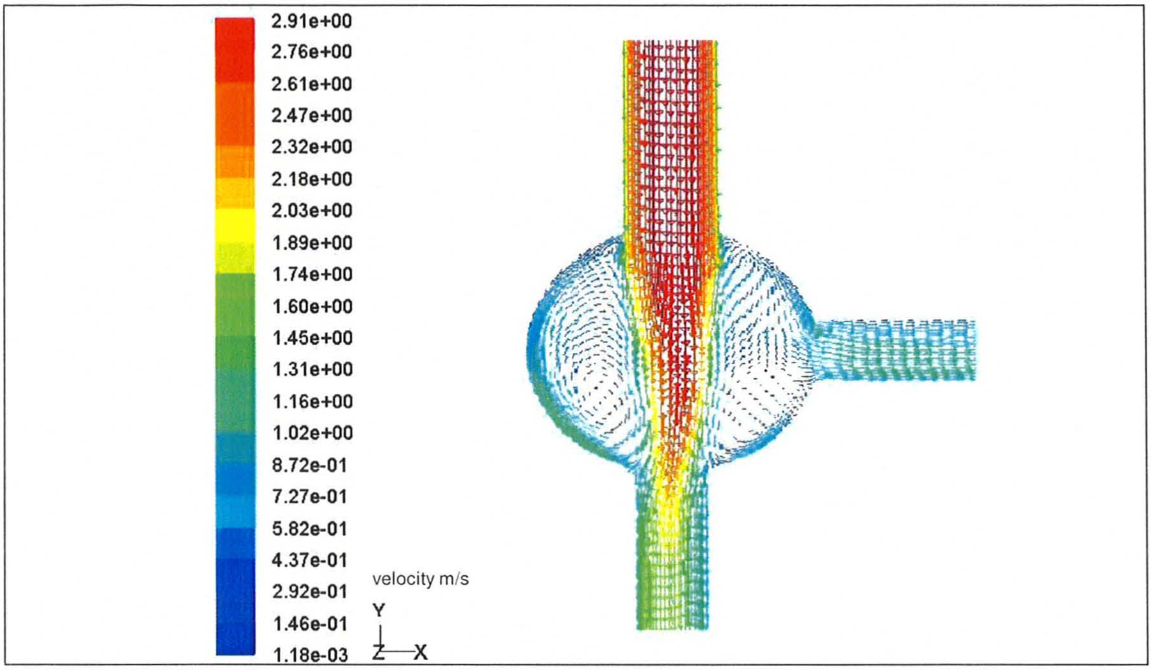

Figure (53): Velocity vectors (m/s) around Inlet1 of the vertical-inlet configuration (Inlet1 = Inlet2 = 0.310 kg/s) (cross-sectional view).

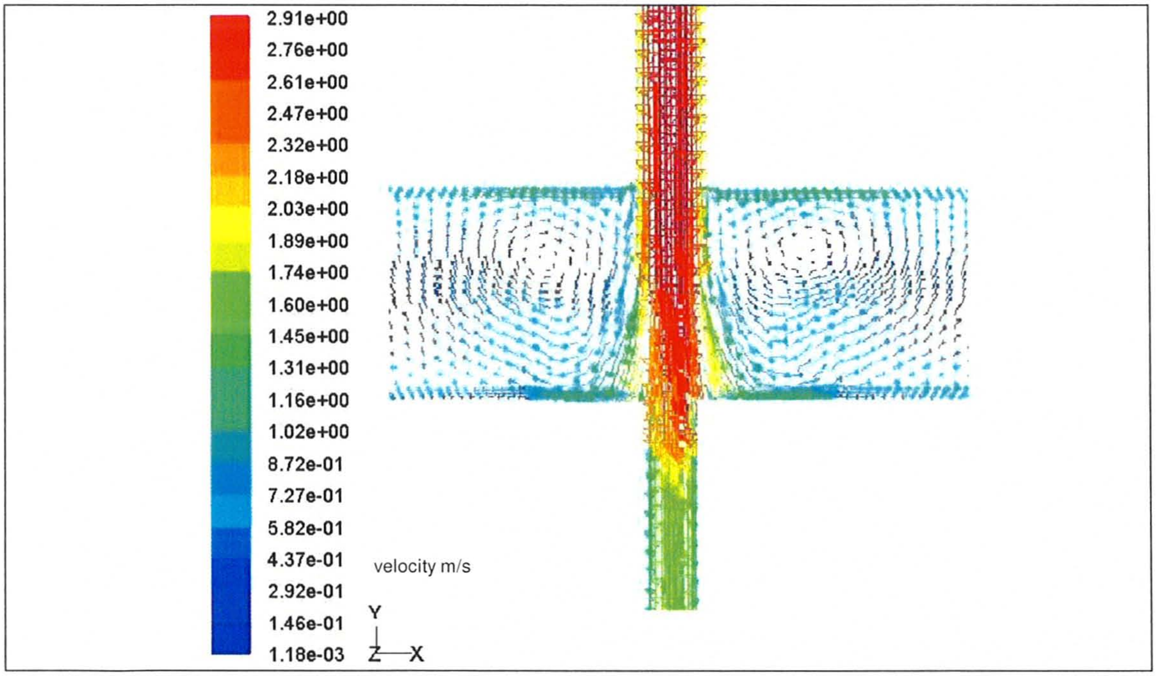

Figure (54): Velocity vectors (m/s) around Inlet1 of the vertical-inlet configuration (Inlet1 = Inlet2 = 0.310 kg/s) (axial view).

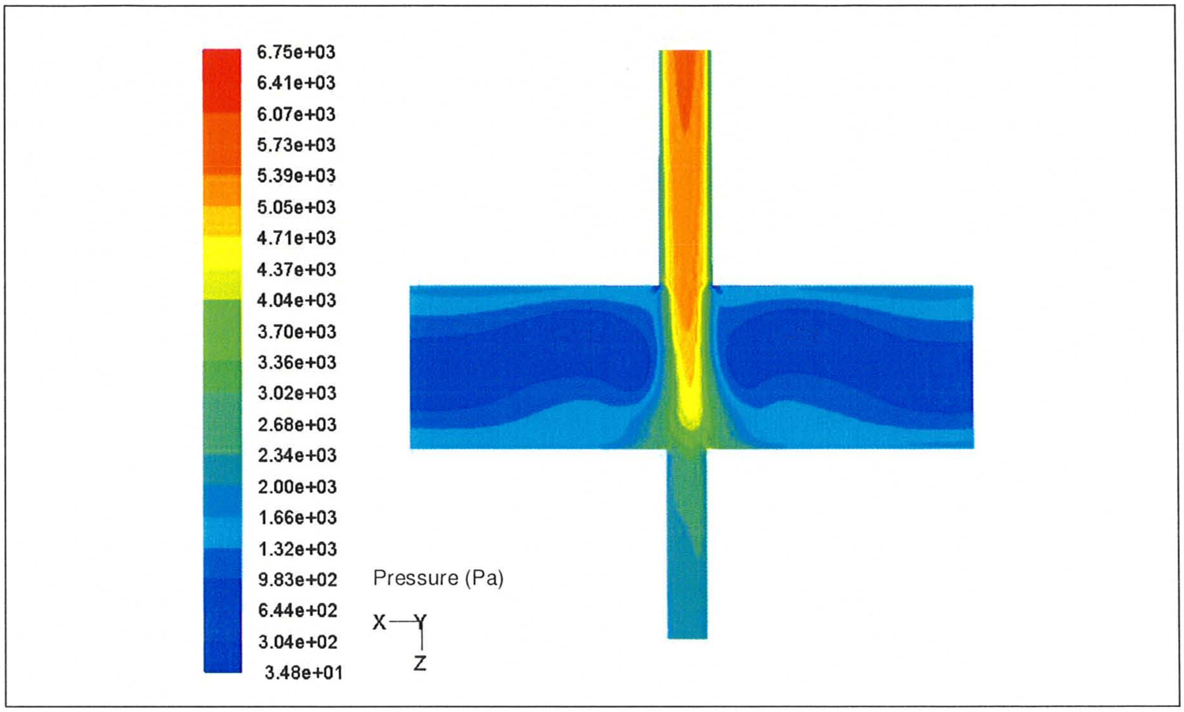

Figure (55): Contours of dynamic pressure (Pa) around Inlet1 of the vertical-inlet configuration (Inlet1 = Inlet2 = 0.310 kg/s) (axial view).

5.2.7 Conclusions

CFD prediction of flow distribution in the multi-branch vertical-inlet header configuration (2.531985×10^6 nodes) provided good agreement with the experimental data under a range of inlet flow levels of imbalance using RNG k-ε turbulence model with enhanced wall treatment.

5.3 Horizontal-Inlet Header Configuration

5.3.1 Geometry and Mesh Generation

A sample of the mesh is shown in Figure (56). Three grid densities (5.29810×10^5, 2.508623×10^6 and 3.949979×10^6 nodes) were investigated to study the effect of grid density on the solution (Section 5.3.3). Maximum value of cell skewness coefficient is 0.8 which is the limit recommended by FLUENT. The Y^+ plot of the mesh is shown in Figure (57) for Inlet1=0.310 kg/s and Inlet2=0.307 kg/s. The value is almost < 5 (except at the inlets) which means the near-wall resolution is in the most accurate region to which the boundary layer can be resolved [28].

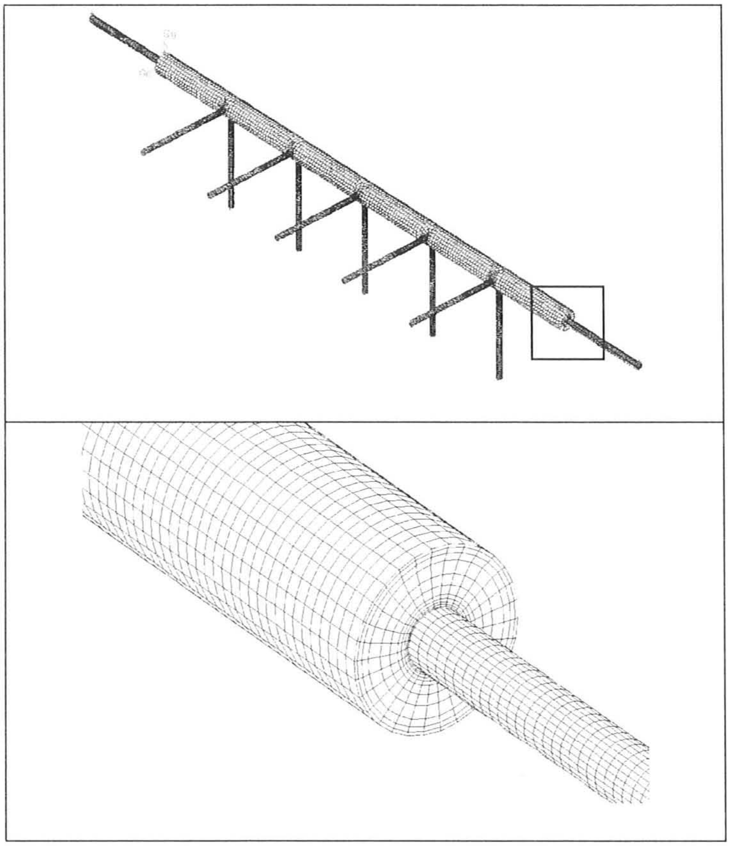

Figure (56): Sample of mesh consisting of 5.29810×10^5 nodes.

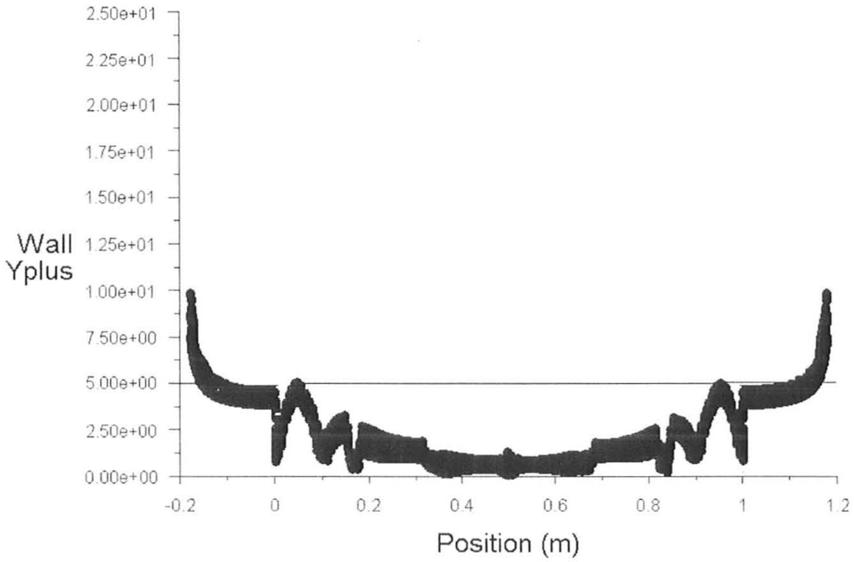

Figure (57): Y^+ value near the wall (Inlet1=0.310 kg/s and Inlet2=0.307 kg/s).

5.3.2 Operating and Boundary Conditions

The boundary and operating conditions assigned in FLUENT are previously shown in Table (7).

5.3.3 Sensitivity Analysis

5.3.3.1 Sensitivity to Grid Density

A mesh of 5.29810×10^5 nodes was initially used. The mesh was then further refined until no significant change in the solution was noticed using two successive grid densities.

The reference grid consists of 2.508623×10^6 nodes. Figure (58) shows the flow distribution obtained using three grid densities (5.29810×10^5, 2.508623×10^6 and

3.949979×10^6 nodes). Very small difference (less than 0.1%) in solution is noticed when using the reference grid and the finest meshes.

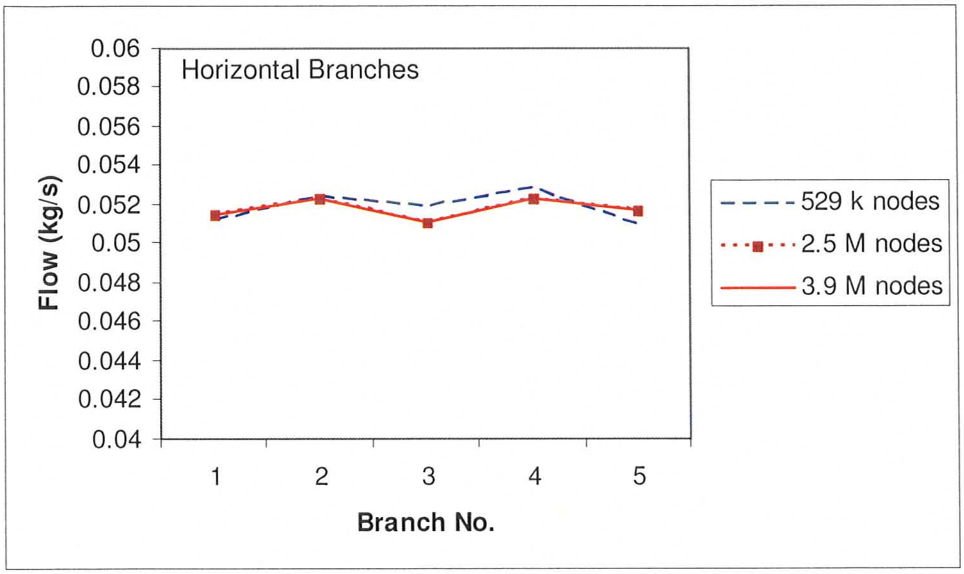

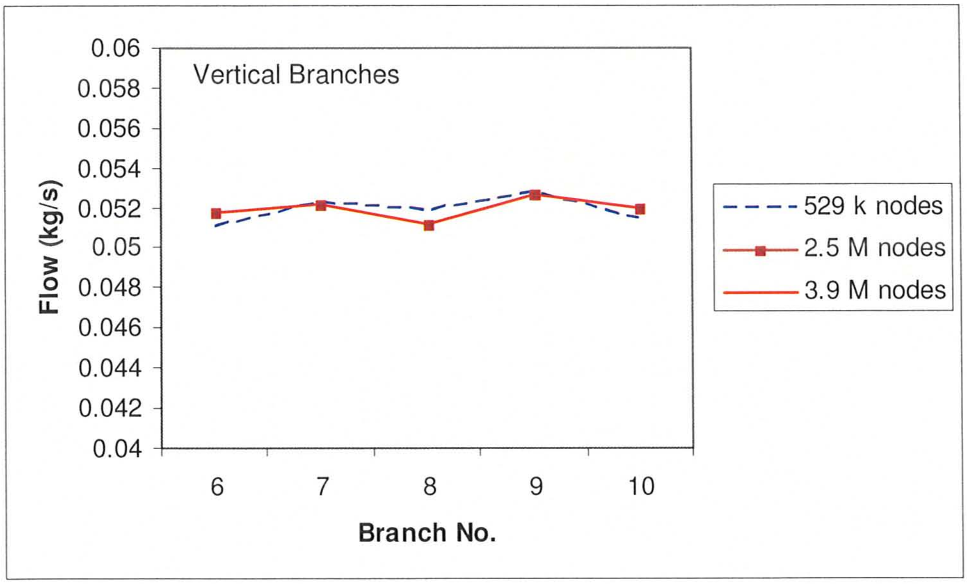

Figure (58): Effect of grid density on flow distribution (Run 1/1H).

5.3.3.2 Selection of Turbulence Model

Similar to the previous validation (Section 5.2.3.2), several combinations of turbulence models with wall treatment methods were investigated and the results were compared to the experimental data. The runs were selected to represent varying levels of imbalance and flow rates. The selected runs are shown in Table (9).

Table (9): Experimental Runs selected to study the sensitivity to turbulence modeling.

Run	**Flow rates (kg/s)/(kg/s)**	**Description**
Run 1/2H	0.301/0.301	Imbalance = 1.00, high flow rate/high flow rate.
Run 3/1H	0.232/0.232	Imbalance = 1.00, moderate flow rate/moderate flow rate.
Run 5/1H	0.232/0.166	Imbalance = 0.71, moderate flow rate/low flow rate.
Run 3/2H	0.307/0.158	Imbalance = 0.51, high flow rate/low flow rate.
Run 5/2H	0.307/0.000	Imbalance = 0.00, high flow rate/no flow.

Several comparisons are shown in Figures (59) to Figures (62) where the sum of error predictions for all branches is plotted versus each model/wall treatment combination. The error is defined as:

$$\text{Error} = \sum_{i=1}^{10} \left| (q_i)_{\text{Exp}} - (q_i)_{\text{FLUENT}} \right| \tag{14}$$

Where q_i is: flow rate in branch i (kg/s).

As the figures show, the RNG k-ε model with enhanced wall treatment provides the best data fit with minimum deviation from the experimental data (most predictions are within the measurement error bar). The standard k-ω model also provides good predictions. The RNG k-ε model was selected for the rest of this work.

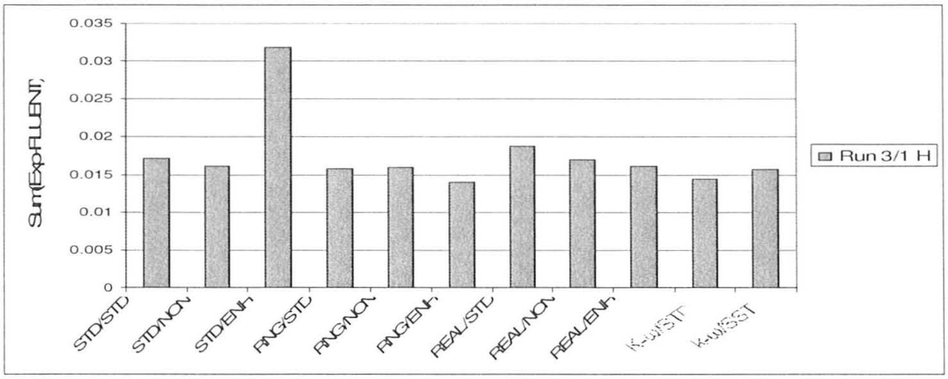

Figure (59): Summation of prediction errors for each combination of turbulence model/wall treatment for Run 3/1H (0.232/0.232 (kg/s)/(kg/s)).

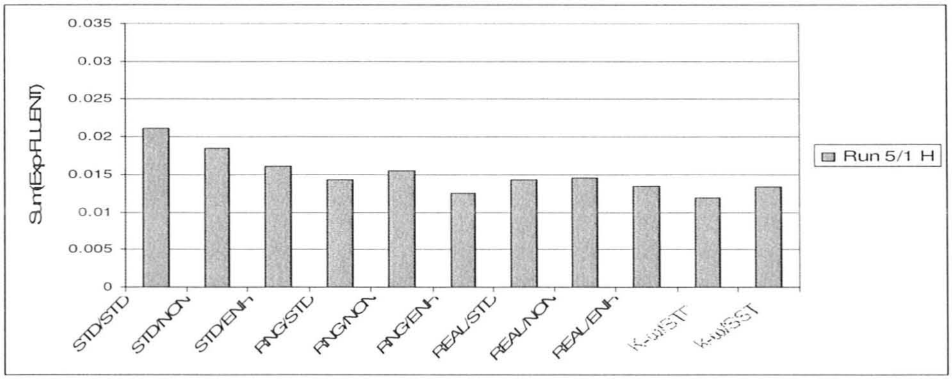

Figure (60): Summation of prediction errors for each combination of turbulence model/wall treatment for Run 5/1H (0.232/0.166 (kg/s)/(kg/s)).

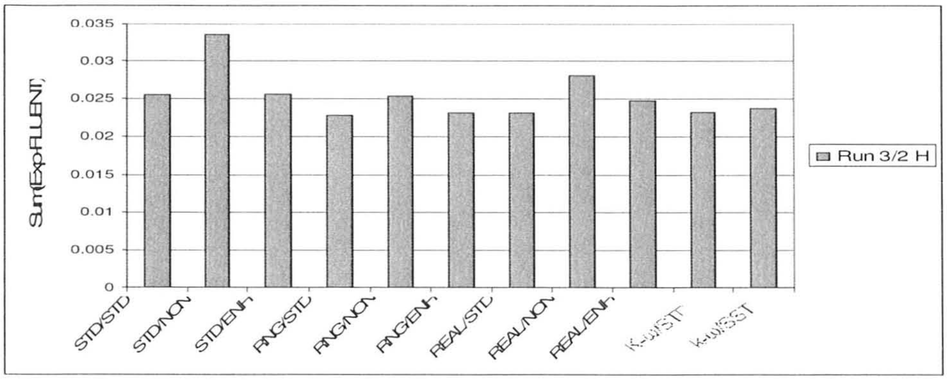

Figure (61): Summation of prediction errors for each combination of turbulence model/wall treatment for Run 3/2H (0.307/0.158 (kg/s)/(kg/s)).

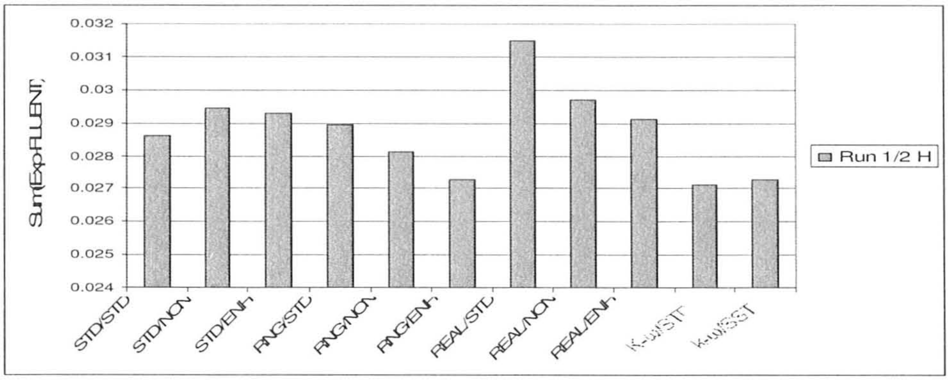

Figure (62): Summation of prediction errors for each combination of turbulence model/wall treatment for Run 1/2H (0.307/0.307 (kg/s)/(kg/s)).

5.3.3.3 Convergence Criteria

Sensitivity analysis of flow distribution to convergence criteria has been conducted similar to that in Section 5.2.2.3. No significant change in solution (less than 0.1 %) was noticed when it was decreased from 10^{-5} to 10^{-6} and thus the tolerance was set to 10^{-5} in the rest of this work. The results are shown in Figure (63) for Run 1/1H.

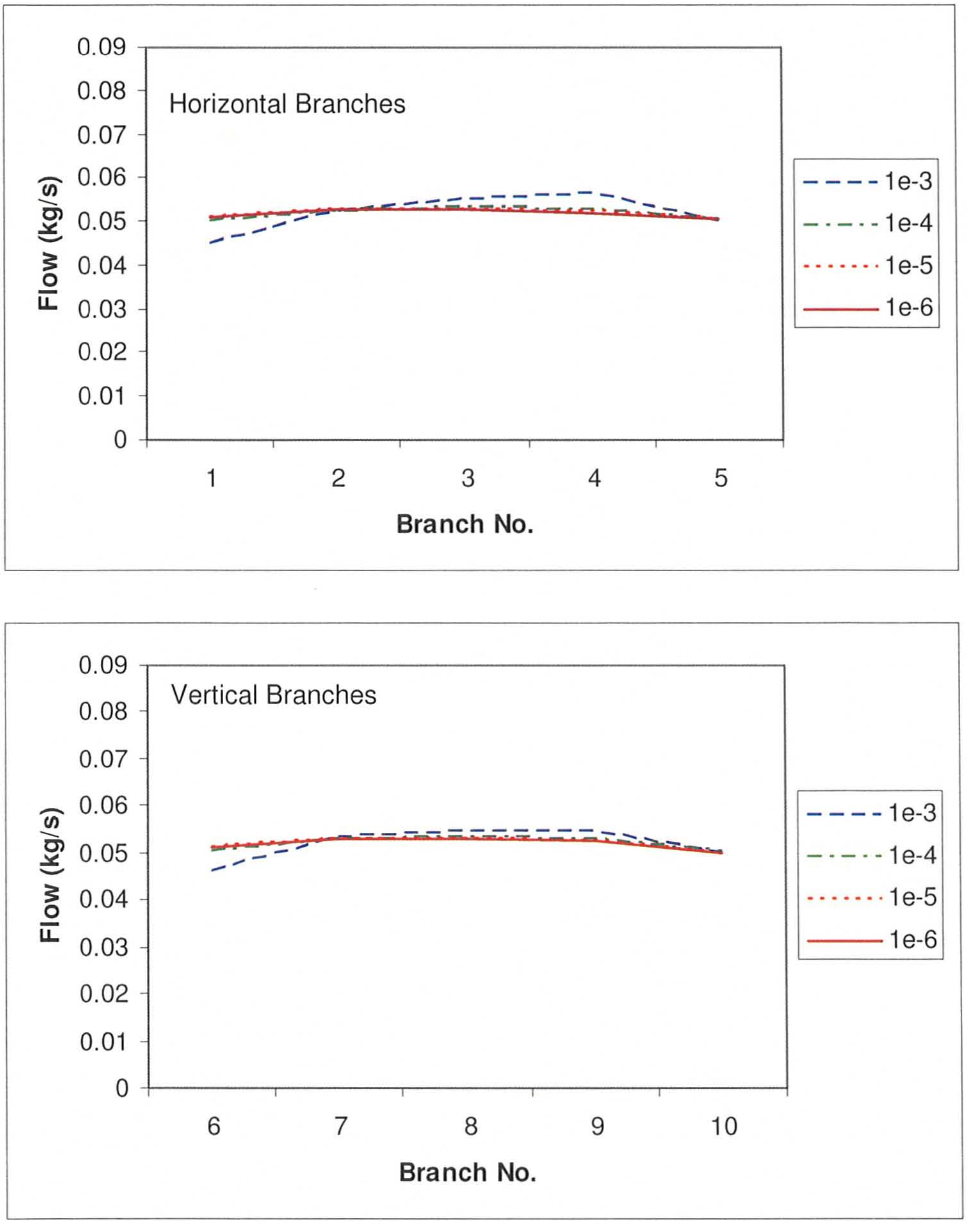

Figure (63): Sensitivity of flow distribution to convergence criteria (Run 1/1H).

5.3.4 Flow Prediction Results

The measured outlet flow rates for all runs were compared to FLUENT predictions as shown in Figure (64) to Figure (67). Good agreement with the experiment is noticed. Also, most predictions are within the accuracy of the outlet flow meters (±0.0025 kg/s).

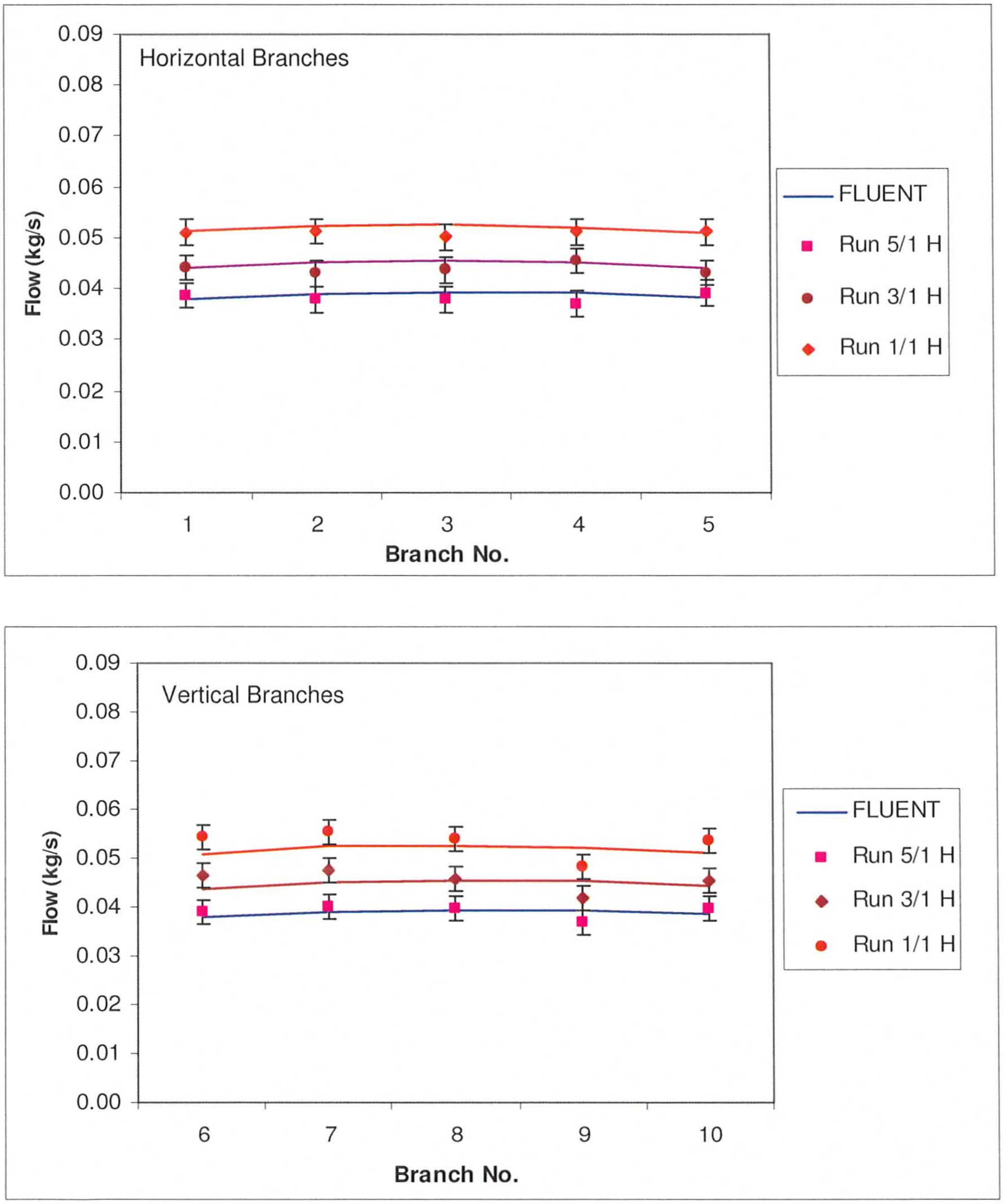

Figure (64): Experimental data and FLUENT predictions of flow distribution (Run 5/1 H, Run 3/1 H and Run 1/1 H).

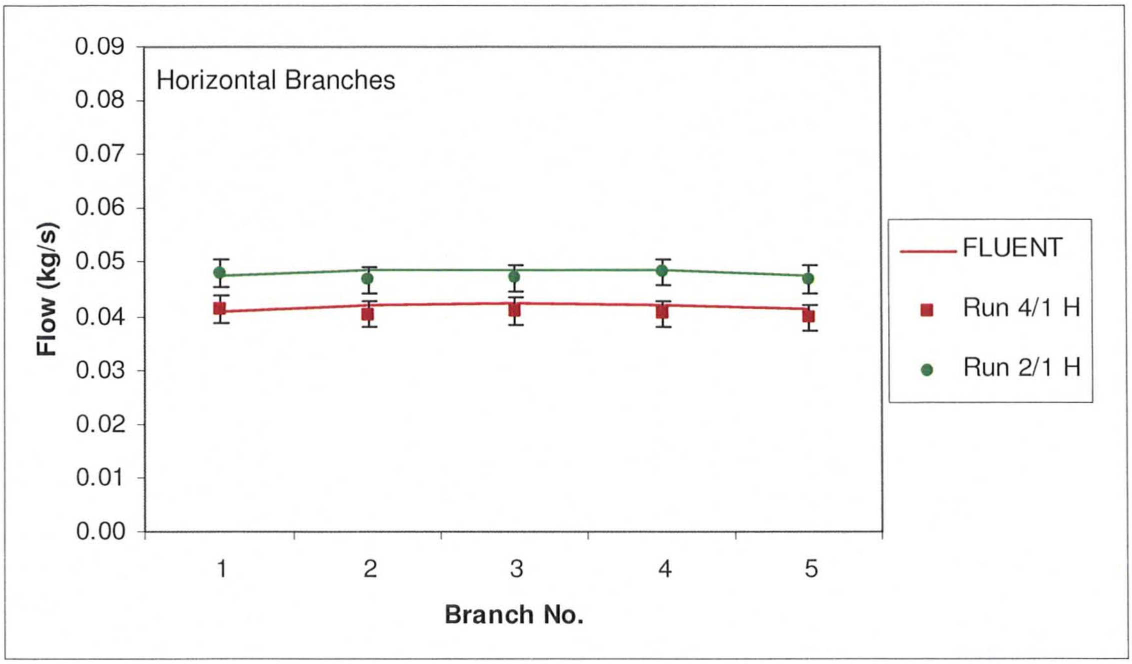

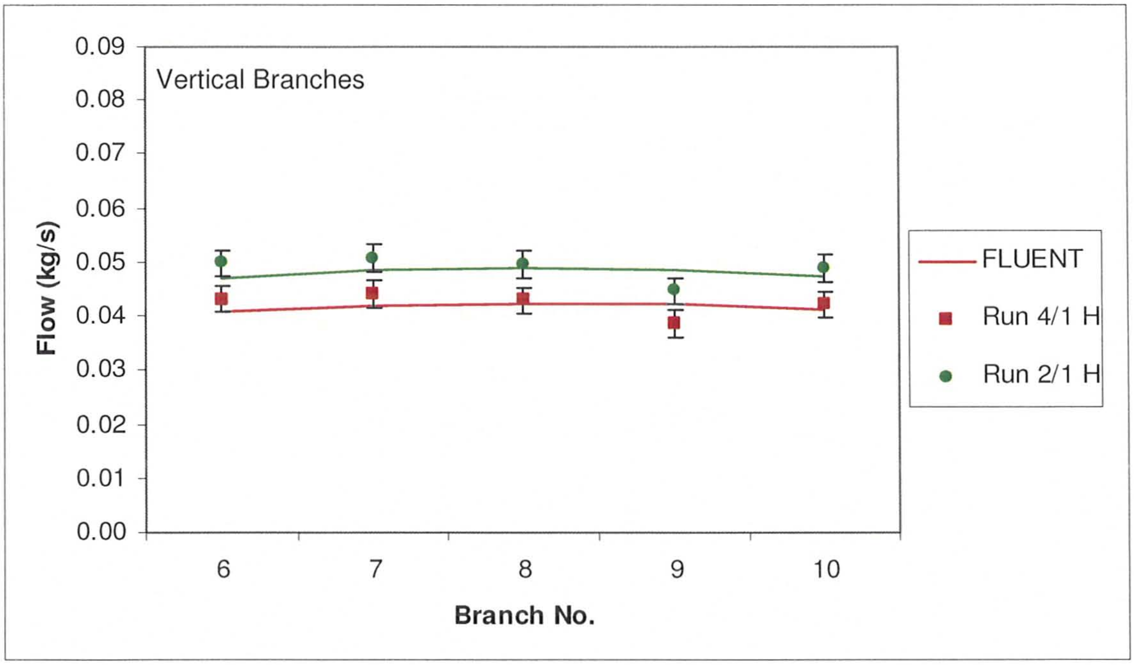

Figure (65): Experimental data and FLUENT predictions of flow distribution (Run 4/1 H, and Run 2/1 H).

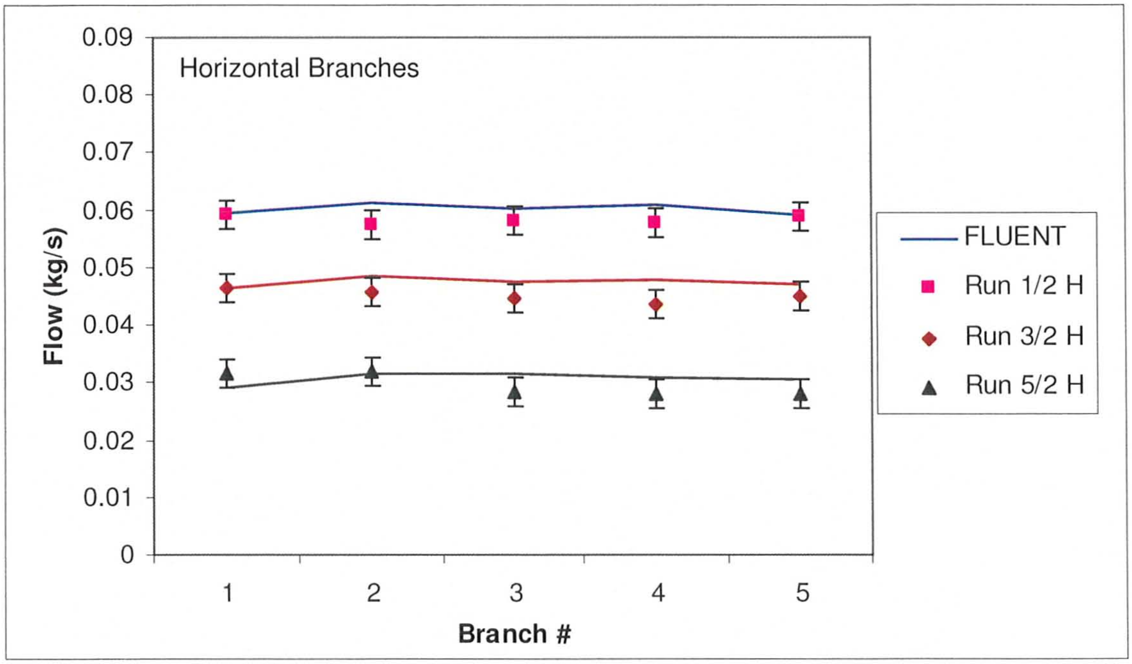

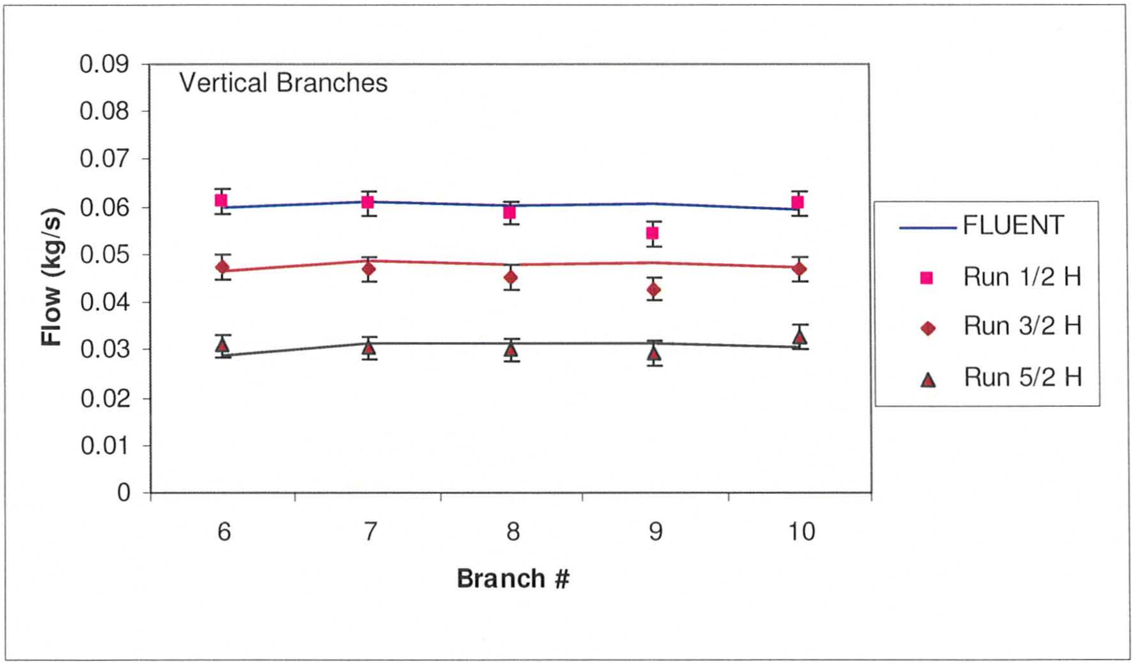

Figure (66): Experimental data and FLUENT predictions of flow distribution (Run 1/2 H, Run 3/2 H and Run 5/2 H).

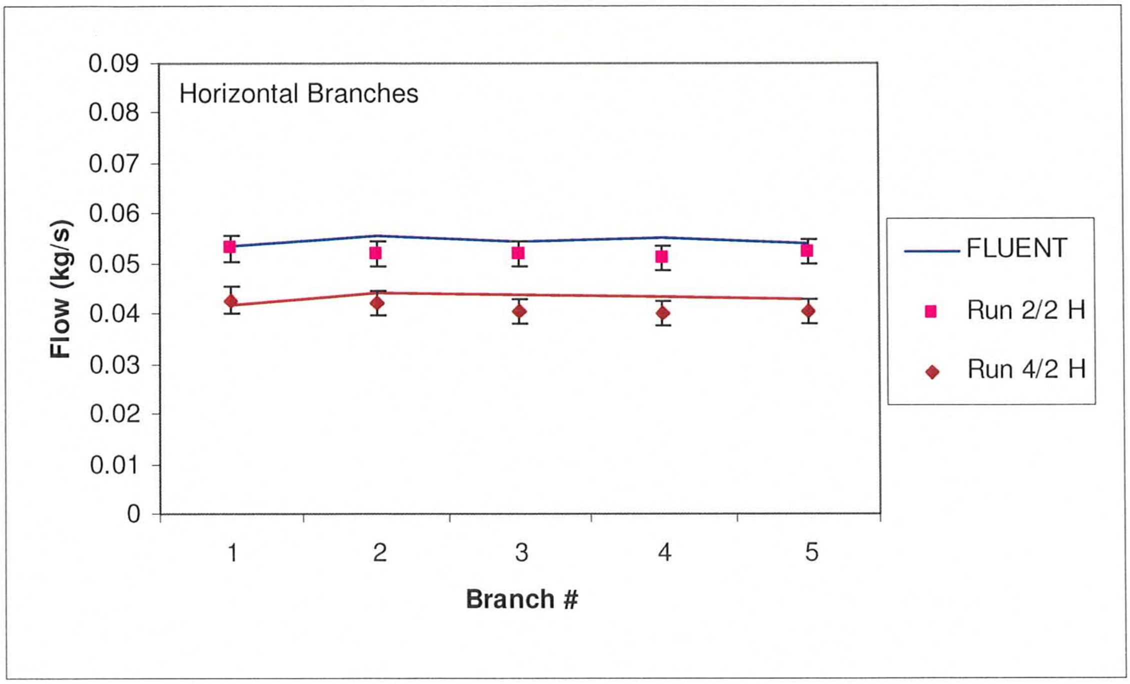

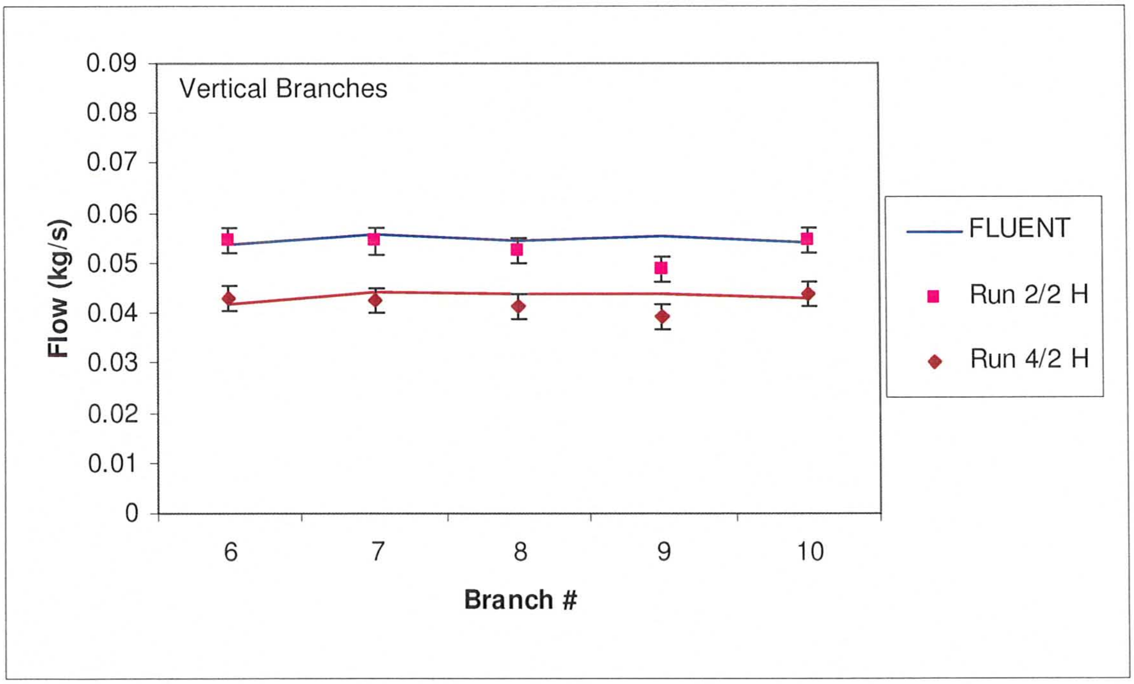

Figure (67): Experimental data and FLUENT predictions of flow distribution (Run 2/2 H and Run 4/2 H).

5.3.5 Effect of Inlet Flow Imbalance Level

The relative errors of flow rate predictions for Run 1/1H to Run 5/1H in Table (3) are plotted versus the inlet flow levels of imbalance as shown in Figure (68). The figure shows that the error is almost the same for all levels of imbalance. This is due to the relatively high flow rates in this run (minimum inlet flow rate was 0.166 kg/s) and due to the accuracy in the measurements as ten trials were done and a DAS was used. Similarly, prediction error versus the imbalance level is plotted for Run 1/2 H to Run 5/2 H as shown in Figure (69). The same trend is notices.

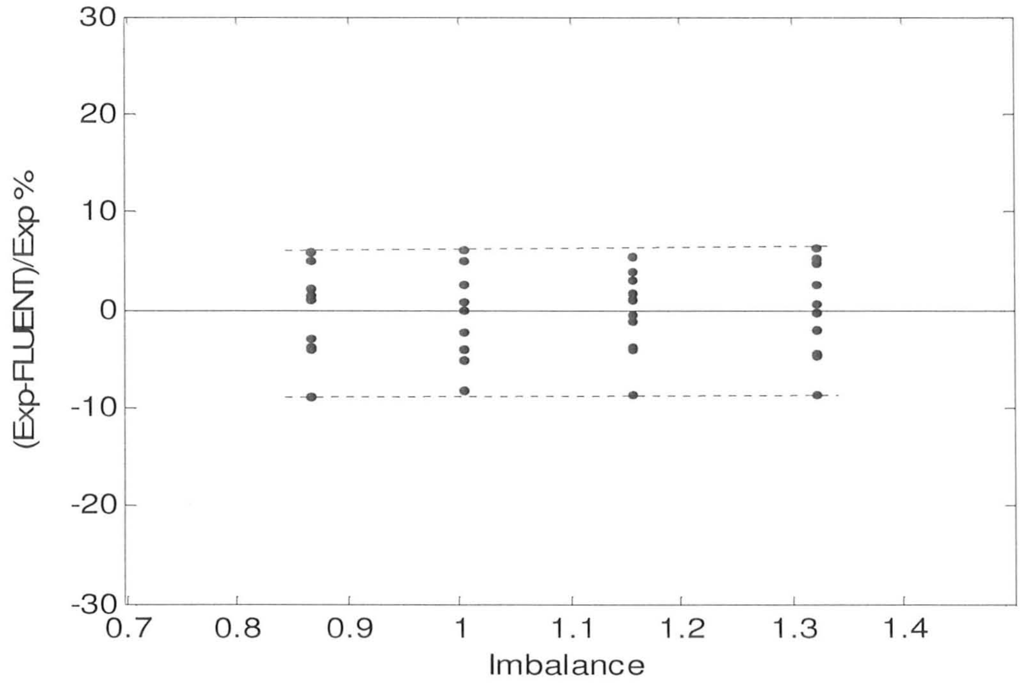

Figure (68): Flow error versus imbalance (Inlet 1 kept constant 0.232 kg/s).

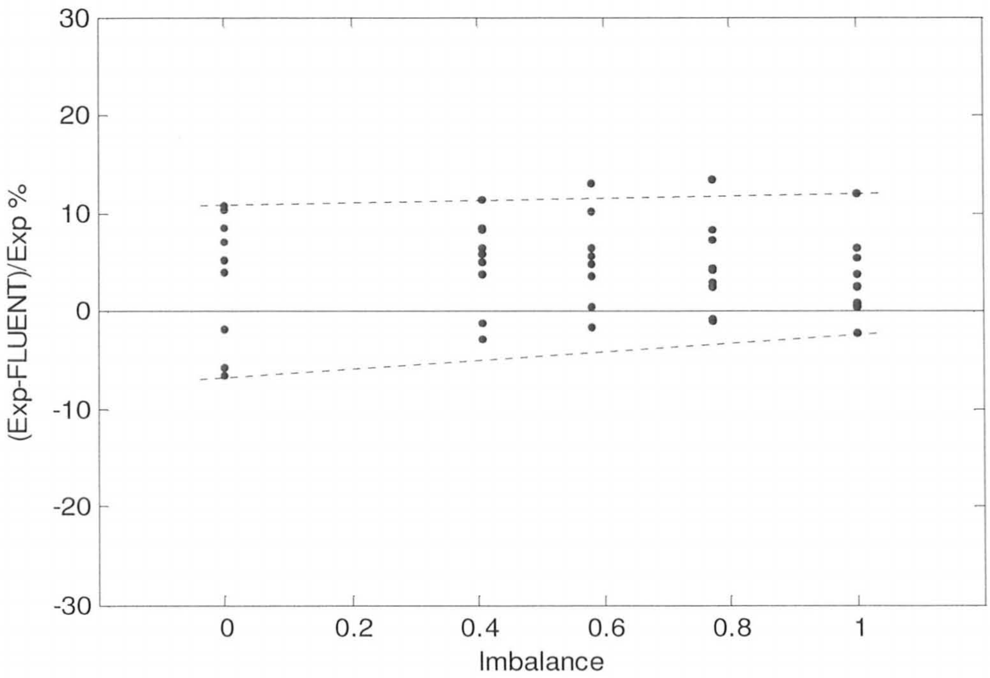

Figure (69): Flow error versus imbalance (Inlet 1 kept constant at 0.307 kg/s).

5.3.6 Pressure Gradients

Pressure contours along the header axis for both configurations are shown in Figure (70). The figure shows that the vertical-inlet configuration encounters higher pressure gradient along the header from the inlets to the far edges of the header (the red and blue regions; respectively). The highest pressure in the vertical-inlet configuration is noticed to be just beneath the two inlets and this explains why the outlet flow rates in branches 7 and 9 are always higher than those in the other branches for most of the entire flow cases. The low pressure regions (blue regions) are not noticed in the horizontal-inlet configuration but more uniform pressure gradients exists. This explains why more flow uniformity is noticed for this configuration.

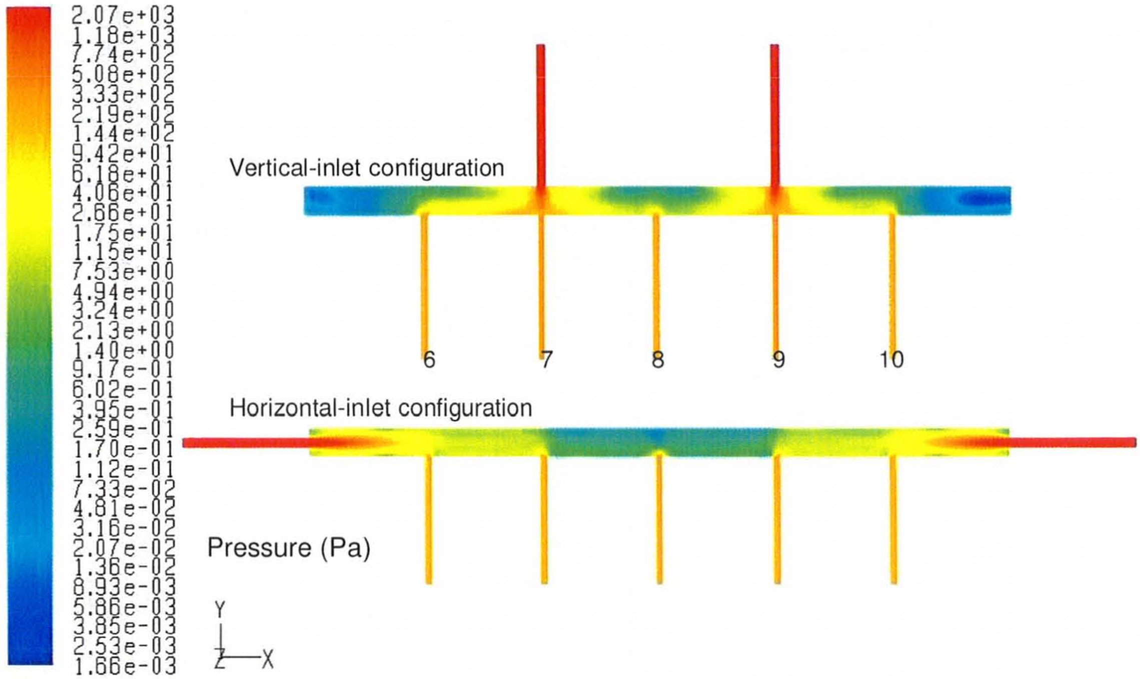

Figure (70): Contours of dynamic pressure along the header axis for both header configurations (Inlet1=Inlet2= 0.232 kg/s).

5.3.7 Conclusions

CFD prediction of flow distribution in the multi-branch horizontal-inlet header configuration (2.508623×10^6 nodes) provided good agreement with experimental data under a range of inlet levels of imbalance using the RNG k-ε turbulence model with enhanced wall treatment which found to provide best fit of the data.

Chapter 6

Conclusions

1. The analysis of flow distribution and pressure gradients in the CANDU header is of great importance for the reactor safety. The one dimensional system codes have been successful for the NSA because they use a large database of empirical correlations. However, these correlations were formulated mainly from one dimensional separate-effect experiments and, also, are restricted to their operating conditions. The flow in many reactor components (like the headers) is three dimensional in nature, and for NSA the three dimensional effects should be accounted for. Therefore, there has been a move towards the CFD tools in NSA and reactor design. CFD tools have shown promising results for several reactor large and complex components.

2. CFD tools have not been widely used in NSA due to the complexity in analyzing transient, two-phase flows usually occur under accident scenarios in addition to the issue of the code validation. However, the computational capabilities are being improved.

3. This study validated FLUENT, a CFD code, for the flow distribution in headers with two different geometries representing various CANDU header designs. Validation using cylindrical header with vertical/horizontal inlet configurations showed good

agreement with the experimental data. The results showed that FLUENT well predicted the flow distribution under varying levels of imbalance. However, the deviation between the experiment and the predictions was found to increase as the level of imbalance decreases. This is due to the difficulty in measuring the very low flow rates and might not be due to the level of imbalance itself.

4. It was found that FLUENT predicted 95.14% of all flow measurements with less than 9% relative error for vertical-inlet header configuration and predicted 94.0% of all flow measurements with less than 5% relative error for horizontal-inlet header configuration. The difference is accuracy is believed to result from the quality of the experimental data, since 10 repeated measurements were performed for the latter, and only limited repeats performed for the former. Also, the uniformity in flow distribution in the horizontal inlet configuration header makes it easier to be predicted by FLUENT.

5. Those flow measurement predictions with more than 7% relative error are mainly due to experimental errors. It is believed that the main experimental error is the difficulty in controlling the inlet flowrate and hold it at constant value. Thus, CFD has been found to be an efficient tool for analyzing the single-phase flow in headers under the studied operating conditions.

6. Based on the results of this study, the recommended turbulence model to use for header geometries under steady state conditions is the RNG k-ε model. This model is also widely applicable and is commonly used in the literature. The finding of this study is in agreement with another published work [10] where the RNG model with enhanced wall treatment provided best data fit of flow in coupled manifolds (two main horizontal tubes connected with three risers) for a range of Re number. The RNG model is widely applicable for complex flow behaviors, separating and recirculating flows, curved geometries, and applicable over large range of Re. k-ω also performed satisfactorily but RNG was favoured since it is more commonly applied across a wide range of geometries.

7. Based on the results of this study and on notes from the literature, the CFD tools are capable to predict the full size CANDU header gradients taking the following points into consideration:

(a) In the full size header, some problems might be faced in properly building and meshing the complex geometry to get a high quality grid (some details of the geometry might be needed to be simplified). Also, large number of nodes is required to get the mesh independency.

(b) In modeling the flow under steady state conditions, the RNG with enhanced wall treatment is the more attractive model to use and to start with. However, validation is still recommended on the large scale as the geometry there is much more complex and the operating conditions are different than those in the small scale validation. In this study, k-ω models also showed closed results to those of the RNG model but, from the literature, the k-ω models show a severe free-stream dependency and thus are not recommended as its results are strongly dependent on the user input [17].

(c) In applying the CFD tools for the full scale header the boundary and initial conditions of the simulation need to be determined. The recommended way to do that is to provide the boundary conditions from a one dimensional system code and to feed the system code with averaged boundary conditions from the CFD code in what is called "code coupling". However, the coupling itself can be a source of errors in addition to the errors in the system code.

(d) The transient nature of most scenarios in NSA makes the application of CFD tools more difficult than for steady state scenarios. Solving the RANS equations for transient conditions might be an additional source of errors. This is due to the fact that RANS equations were derived by integrating over a time T large in comparison with the turbulent time scale. Such averaging is well defined only when T goes to infinity [32]. Thus, transient computations using RANS equations may lead to errors in the results if the simulated process is fast and requires short time steps. An alternative to RANS are Unsteady RANS (URANS), Large Eddy Simulation LES and Detached Eddy Simulation (DES) which are well suited to and recommended for transient computations.

8. Depending on the four points mentioned above, it is expected that the error in simulating the full scale header to be larger than the error found in this study. However, the CFD tools have shown promising results when used to simulate the branching flow in lower plenums and in the PWR downcomers and are highly recommended for the gradients in the CANDU headers.

9. The accuracy of a transient CFD calculation depends on the discretization scheme (first or second order), grid size, grid quality and time step. If the time step is very small, it is expected that the accuracy to be close to that of a steady state calculation. However, for a complex geometry like the CANDU header, it will be computationally very expensive to use a fine grid with a very small time step. The time step itself is also dependent on the grid density. If N^3 is the total number of nodes in a volume, then the time step is roughly proportional to $1/N$ and the run time is roughly proportional to N^5 [17].

Chapter 7

Recommendations

It is recommended to consider the following points in CFD analysis of the reactor components:

1. Validation of CFD tools for NSA should start using simple representing geometries [17] (like the header of this study) with limited number of important variables where all code input data, initial and boundary conditions can be accurately measured. Also repeated experimental runs are preferred in order to detect systematic errors.

2. A balance must be struck between computational accuracy and computational cost. Local grid refinement of the geometry is recommended. Also, very small time steps in specific periods in the entire time domain (like the initial interval of a LOCA transient) are recommended.

As an extension of this work it is recommended to study the following:

1. CFD analysis of full scale CANDU headers. The analysis would be much more complicated due to the geometry complications. However, it would be interesting to

investigate the applicability of the CFD techniques for the real header geometry and under the real operating conditions.

2. CFD analysis of transient single phase flow in the header. The same setup of this study could be used.

3. CFD analysis of steady state and transient two phase flow in the header. The same setup of this study could be used.

4. CFD analysis of CANDU headers coupled with 1-dimentional analysis of the other reactor components and comparison with 1-dimentional analysis for all components (including the headers); i.e. system code-CFD coupling.

5. Validation of CFD tools against measurements of velocity and turbulence distributions along the header using Laser Doppler Anemometry (LDA).

Bibliography

1. J. Luxat, "Safety Analysis Technology: Evolution, Revolution and the Drive to Re-Establish Margins", 21st Annual Conference of the Canadian Nuclear Society, Toronto, Canada, 2000.

2. R. Rock and M. Lightstone, "A Numerical Investigation of Turbulent Diffusion Mixing of Coolant in Rod Bundle Subchannels", CFD98, Quebec, June 1998.

3. X. Jijun, V. Krishnan, P. Ingham, B. Hanna and J. Buell, "Thermalhydraulic Design Methods and Computer Codes", *Shanghai Jiaotong University, Atomic Energy of Canada Limited.*

4. E. Holliday, M. Ali and D. Novog, "Modeling of a Pressure Gradient across a CANDU Reactor Inlet Header", *28th Annual CNS Conference*, Saint John, Canada, June 3 - 6, 2007.

5. I. Love, "Reactor Coolant System, Moderator and Major Auxiliary Systems", *ACR Development Project*, Presented to US Nuclear Regulatory Commission Office of Nuclear Reactor Regulation, September 25, 2002.

6. R. Moffett, M. Soulard, G. Hotte, R. Gibb and A. Banas, "Pressure Distribution Inside a CANDU-6 Reactor Inlet Header", *4th Annual Conference of the CFD Society of Canada*, Ottawa, Ontario, Canada, June 2-6, 1996.

7. A. Kwan, "Modeling of Header for The CANDU Primary Heat Transfer System", McMaster University, 1997.

8. Canadian Nuclear FAQ website, www.nuclearfaq.ca., 2009.

9. R. Bajura and E. Jones, "Flow Distribution Manifolds", *Journal of Fluids Engineering*, Tram. ASME. 1976. Vol. 98.

10. J. Galliera, Isothermal Flow Distribution in Coupled Manifolds: Comparison of Results from CFD and an Integral Model", Villanova University, Villanova, PA, 1998.

11. S. Horiki, T. Nakamura and M. Osakabe, "Thin Flow Header to Distribute Feed Water for Compact Heat Exchanger", *Experimental Thermal and Fluid Science* 28, pp 201–207, 2004.

12. R. Benay, B. Chanetz and Jean Délery, "Code Verification/Validation with Respect

to Experimental Data Banks", *Aerospace Science and Technology*, Volume 7, Issue 4, Pages 239-262, June 2003.

13. X. Jijun, V. Krishnan, P. Ingham, B. Hanna and J. Buell "Thermalhydraulic Design Methods and Computer Codes", Shanghai Jiaotong University, Atomic Energy of Canada Limited.

14. D. Chandraker, N. Maheshwari, D. Saha and V. Venkat Raj, "Experimental and Analytical Investigations on Core Flow Distribution and Pressure Distribution in the Outlet Header of a PHWR", *Experimental Thermal and Fluid Science* Volume 27, Issue 1, December 2002, Pages 11-24.

15. "Accurate Modeling of Difficult Reactor Geometry Permits CFD Simulation of Nuclear Event", *Journal Articles by FLUENT Software Users*, FLUENT Inc., 2009.

16. T. Kethely, "STAR-CD Dynamics", The Customer Magazine of the CD Adapco Group, Issue 20 Spring 2003.

17. "Assessment of Computational Fluid Dynamics (CFD) for Nuclear Reactor Safety Problems", Nuclear Energy Agency Committee on the Safety of Nuclear Installations Assessment, Unclassified, NEA/CSNI/R (2007) 13, January, 2008.

18. Manwoong Kim, Seon-Oh Yu, Hho-Jung Kim, "Analyses on fluid flow and heat transfer inside Calandria vessel of CANDU-6 using CFD", *Nuclear Engineering and Design* 236 (2006) 1155–1164.

19. M. Kim, S. Yu and H. Kim, "Analyses on fluid flow and heat transfer inside Calandria vessel of CANDU-6 using CFD", *Nuclear Engineering and Design* 236 (2006) 1155–1164.

20. D. Chang and S. Tavoularis, "Numerical simulation of turbulent flow in a 37-rod bundle", *Nuclear Engineering and Design*, Volume 237, Issue 6, March 2007, Pages 575-590.

21. Y. Cho, I. Kim and G. Jeun, "Application of CFD Technique to CANDU Header-to-Feeder Free Surface Flow", *NTHAS5: Fifth Korea-Japan Symposium on Nuclear Thermalhydraulics and Safety*, Jeju, Korea, November 26- 29, 2006.

22. P. Gulshani, "Investigation of Natural Circulation Two-Phase Flow Behavior in Header Manifold using CFD Code", *27th Annual Conference of Canadian Nuclear Society*, Toronto, Ontario, Canada, June 11 - 14, 2006.

23. M. An, M. Thompson and M. Wright, "Numerical Simulation of The RD-14M Test T9308", *21st Annual CNS Conference*, Toronto, June 11 - 14, 2000.

24. Z. Zhang and Y. Li, "CFD Simulation on Inlet Configuration of Plate-Fin Heat Exchangers", *Cryogenics* 43 (2003) 673–678.

25. L. Hua, P. He, E. Bibeau, M. Salcudean and I. Gartshore, "Three Dimensional Flow Distribution in a Headbox Manifold", Department of Mechanical Engineering, The University of British Columbia, Vancouver.

26. A. Chen and E. Sparrow, "Turbulence modeling for flow in a distribution manifold", *International Journal of Heat and Mass Transfer* 52 (2009) 1573–1581.

27. M. Uygun, S. Onbasiglu and S. Avci, "Turbulence Modeling for Computational Fluid Dynamics, Part I: Conceptual Outlook", *Journal of Aeronautics and Space Technologies*, July 2004 Volume 1 Number 4 (19-26).

28. FLUENT 6.3.26 Documentation, www.fluent.com, 2008, "Modeling Turbulent Flows", FLUENT Software Training TRN-99-003, FLUENT Inc., 2009.

29. Gambit Documentation, FLUENT Inc., 2008.

30. S. Patankar, "Numerical Heat Transfer and Fluid Flow", Hemisphere Publishing Corporation, 1997.

31. M. Osakabe, T. Hamada and S. Horiki, "Water Flow Distribution in Horizontal Header Contaminated with Bubbles", *International Journal of Multiphase Flow*, Volume 25, Issue 5, August 1999, Pages 827-840.

Appendix

Appendix A: Experimental Data

A1: Experimental Data of Flow Distribution in the Upward Header

Table (A1): Experimental data for upward header size 10×40×1000 mm [11].

Q (m^3/s)×10^{-3}	V (m/s)	Re	q_1/Q	q_2/Q	q_3/Q	q_4/Q
0.028	0.071	0.8173	0.310	0.246	0.240	0.199
0.042	0.106	1.2174	0.296	0.245	0.245	0.212
0.058	0.145	1.6598	0.273	0.247	0.255	0.226
0.072	0.181	2.0690	0.262	0.248	0.253	0.238
0.083	0.209	2.3891	0.258	0.250	0.249	0.242
0.103	0.257	2.9435	0.261	0.250	0.250	0.239
0.121	0.302	3.4578	0.257	0.248	0.253	0.241
0.137	0.342	3.9151	0.258	0.249	0.248	0.238
0.152	0.380	4.3437	2.259	0.249	0.251	0.240
0.162	0.405	4.6295	0.261	0.248	0.246	0.243

A2: Experimental Data of Flow Distribution in the Cylindrical Header

Vertical-Inlet Header Configuration

(All values are in L/min as experimentally measured with accuracy of ±0.15 L/min)

Table (A2): Experimental data of flow distribution (Inlet 1 kept constant at 18.50 L/min).

18.50/18.50	18.50/14.00	18.50/9.50	18.50/5.00	18.50/0.00
3.71	3.14	2.77	2.24	1.84
3.53	3.08	2.71	2.22	1.72
3.59	3.08	2.64	2.16	1.42
3.37	2.93	2.50	2.15	1.58
3.68	3.22	2.73	2.29	1.80
3.64	3.07	2.75	2.24	1.75
4.59	4.28	3.91	3.67	3.27
3.67	3.18	2.74	2.27	1.76
4.53	3.72	3.02	2.48	1.76

Table (A3): Experimental data of flow distribution (Inlet 1 kept constant at 14.00 L/min).

14.00/18.50	**14.00/14.00**	**14.00/9.50**	**14.00/5.00**	**14.00/0.00**
3.12	3.12	2.24	1.81	1.34
2.93	2.93	2.02	1.54	0.95
3.14	3.14	2.26	1.81	1.29
2.82	2.82	2.12	1.74	1.30
3.12	3.12	2.24	1.82	1.32
3.17	3.17	2.26	1.83	1.37
3.82	3.82	3.02	2.66	2.30
3.15	3.15	2.26	1.80	1.29
4.17	4.17	2.67	1.98	1.33

Table (A4): Experimental data of flow distribution (Inlet 1 kept constant at 9.500 L/min).

9.50/18.5	**9.5&14.00**	**9.5/9.5**	**9.50/5.00**	**9.50/0.00**
2.83	2.32	1.91	1.53	1.05
2.73	2.29	1.87	1.44	0.74
2.63	2.05	1.63	1.15	0.46
2.61	1.97	1.68	1.22	0.83
2.82	2.16	1.90	1.45	0.95
2.70	2.24	1.81	1.43	1.01
3.15	2.65	2.33	2.02	1.76
2.81	2.24	1.91	1.45	0.96
3.96	3.08	2.27	1.67	1.04

Table (A5): Experimental data of flow distribution (Inlet 1 kept constant at 5.00 L/min).

5.00/18.50	**5.00/14.00**	**5.00/9.50**	**5.00/5.00**
2.37	1.95	1.52	1.11
2.34	1.92	1.53	1.07
2.12	1.68	1.24	0.73
2.11	1.71	1.30	0.87
2.25	1.91	1.46	1.06
2.22	1.85	1.47	1.05
2.55	2.12	1.72	1.34
2.28	1.88	1.42	1.05
3.65	2.77	2.03	1.32

Table (A6): Experimental data of flow distribution (Inlet 1 kept constant at 0.00 L/min).

0.00/18.5	**0.00/14.00**	**0.00/9.00**
1.89	1.32	0.94
1.80	1.33	0.88
1.60	1.24	0.66
1.67	1.06	0.62
1.91	1.41	1.02
1.72	1.32	1.02
1.77	1.34	0.98
1.77	1.21	0.83
3.24	2.40	1.59

Horizontal-Inlet Header Configuration

(All values are in L/min as experimentally measured with accuracy of ±0.15 L/min)

Table (A7): Experimental data of flow distribution (Inlet 1 kept constant at 14.00 L/min).

14.00/12.10	**14.00/10.20**	**14.10/14.00**	**14.00/16.20**	**14.00/18.50**
2.486	2.323	2.652	2.886	3.069
2.426	2.275	2.583	2.809	3.081
2.464	2.274	2.624	2.829	3.016
2.431	2.228	2.733	2.898	3.081
2.384	2.350	2.596	2.812	3.077
2.591	2.342	2.796	2.995	3.261
2.654	2.415	2.860	3.041	3.320
2.575	2.391	2.750	2.981	3.238
2.322	2.213	2.510	2.687	2.884
2.532	2.391	2.723	2.940	3.213

Table (A8): Experimental data of flow distribution (Inlet 1 kept constant at 18.00 L/min).

18.10/18.10	**18.50/14.30**	**18.10/10.50**	**18.50/7.50**	**18.50/0.00**
2.323	3.187	2.784	2.568	1.896
2.275	3.118	2.746	2.527	1.924
2.274	3.126	2.688	2.432	1.705
2.228	3.066	2.619	2.406	1.685
2.355	3.144	2.704	2.441	1.690
2.342	3.270	2.842	2.591	1.851
2.415	3.264	2.824	2.565	1.826
2.391	3.141	2.723	2.480	1.801
2.213	2.935	2.571	2.357	1.755
2.391	3.270	2.828	2.622	1.974

Appendix B: Calibration of Flow Meters

The inlet flow meters were calibrated using a graduated cylinder and a stopwatch and calibration lines were generated (measured flow rate versus the flow meter reading). The plots are shown in Figure (B1) and Figure (B2) for inlet 1 and inlet 2 flow meters; respectively.

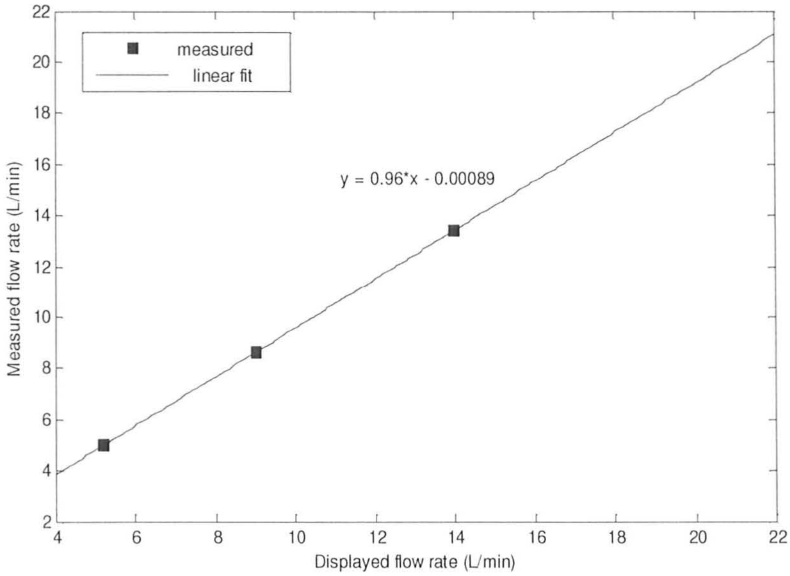

Figure (B1): Inlet 1 calibration line.

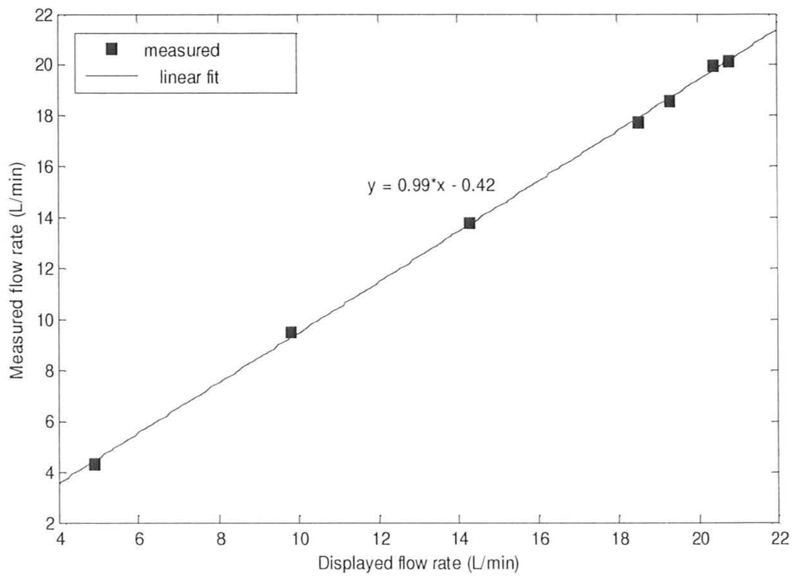

Figure (B2): Inlet 2 calibration line.